UNIVERSITÀ
DEGLI STUDI
DI PADOVA

Sede Amministrativa: Università degli Studi di Padova

Dipartimento di *Ingegneria Industriale*

CORSO DI DOTTORATO DI RICERCA IN: Ingegneria Industriale

CURRICOLO: Thermo-mechanical energy engineering

CICLO XXXI

NEW FRONTIERS AND ENVIRONMENTAL SUSTAINABILITY OF REFRIGERATION SYSTEMS

Tesi redatta con il contributo finanziario dell'Istituto per le tecnologie della costruzione (ITC) del Consiglio Nazionale delle Ricerche (CNR)

Coordinatore: Ch.mo Prof. Luisa Rossetto

Supervisore: Ch.mo Prof. Claudio Zilio

Co-Supervisore: Ing. Silvia Minetto

Dottorando : Ing. Pietro Saglia

ABSTRACT

Clothes drying is a very energy-intensive process and it has a high impact in the domestic electricity consumption. In 2005, the EU-28 total energy consumption of household tumble dryers has been estimated at 21 TWh and an increase up to 30 TWh in 2020 will be expected. Therefore, there is a strong interest to improve the efficiency of these household appliances in order to reduce their energy consumption. In fact, the traditional technology of domestic tumble dryers, based on opened or closed air cycle, uses electrical heaters to warm up the process air before the entrance in the drum. Since many years, vapour compression heat pump system has been identified as a suitable technology for more efficient household tumble dryers. In the case of heat pump tumble dryers, it is of the greatest importance to pursue efficiency improvement, by focusing on the single components or process and in the general unit operation. The research focuses on the process of mass transfer in order to improve the condensation rate, leading to a faster removal of moisture. The fin surface characteristics impact on heat and mass transfer rate, as well as on air pressure losses; in a tumble dryer the selection of the surface which leads to the fastest removal of moisture from the air is crucial. For this purpose, an experimental study was undertaken to evaluate the impact of different coatings on evaporator performance during dehumidification process. Studies in the existing literature that investigate into the impact of fin coatings in dehumidification process are limited. Moreover, data at high air absolute humidity (more than 40 g_v/kg_a) are not available in the open literature. A wind tunnel was then designed and built at the ITC-CNR of Padova for experimental investigations. A characterization of the heat exchanger behaviour in dry conditions was performed. Then, tests in dehumidification conditions were carried out to compare experimental results to a dehumidification model. Good model predictions was found using a log-mean enthalpy method (LMED) for tests with air inlet absolute humidity up to 30 g_v/kg_a; for higher values of this parameter, the relative difference between experimental and model results increased. The model assumption of a unit value of the Lewis Factor was not verified for tests with air inlet absolute humidity higher than 30 g_v/kg_a; a Lewis Factor equal to 0.5 was calculated. An alternative model was then considered, based on a modification of the previous log-mean enthalpy difference method (m-LMED). This model included the Lewis Factor value in the calculation of the overall heat transfer coefficient. For tests with air inlet absolute humidity higher than 30 g_v/kg_a, relative differences below 10% was found between experimental results and m-LMED predictions. The core of the experimental activity investigated into the impact of fin coatings on heat exchanger performance in dehumidification conditions. Experimental test conditions were characterized by values of air inlet absolute humidity higher than 40 g_v/kg_a. Three test sample with different surface characteristics were analyzed: one is the untreated aluminium surface, a second with an hydrophilic

coating and a third with an hydrophobic coating. Comparisons were carried out according to the total heat transfer rate, the drain rate and the retained weight. Dehumidification tests were performed in steady state conditions at different air volumetric flow rates. The hydrophobic sample presented the lowest values of heat transfer rate and drain rate for all the investigated flow rates, but it showed the highest values of retained weight. On the other hand, the hydrophilic and the untreated samples showed similar values of heat transfer rate, drain rate and retained weight, highlighting no relevant difference between their behaviour in dehumidification conditions.

NEW FRONTIERS AND ENVIRONMENTAL SUSTAINABILITY OF REFRIGERATION SYSTEMS

TABLE OF CONTENTS

NOMENCLATURE

A_{box}	psychrometer box cross section area [m^2]
A_e	external heat transfer area [m^2]
AE_c	weighted annual energy consumption [$kWh \cdot year^{-1}$]
A_{fr}	frontal cross section area [m^2]
A_i	internal heat transfer area [m^2]
A_t	tube external heat transfer area [m^2]
A_{tube}	tube cross section area [m^2]
b	coefficient relating the enthalpy of saturated moist air to air temperature [$J \cdot kg^{-1} \cdot K$]
C_{dry}	average condensation efficiency at full load [/]
$C_{dry1\cdot2}$	average condensation efficiency at partial load [/]
COP	Coefficient of Performance [/]
$c_{p,a}$	air specific heat at constant pressure [$J \cdot kg^{-1} \cdot K^{-1}$]
$c_{p,w}$	water specific heat at constant pressure [$J \cdot kg^{-1} \cdot K^{-1}$]
C_t	average condensation efficiency both at full and partial load [/]
D_0	outside tube diameter [m]
EEI	Energy Efficiency Index [/]
F	correction factor [/]
f	fraction of solid surface area wet by the liquid [/]
$f(\theta)$	contact angle function [/]
f_{bp}	bypass factor [/]
G	Gibbs free energy [J]
H	enthalpy [J]
h	specific enthalpy [$J \cdot kg^{-1}$]
$h_{a,amb}$	ambient air specific enthalpy [$J \cdot kg^{-1}$]
$h_{a,in}$	air inlet specific enthalpy [$J \cdot kg^{-1}$]
$h_{a,out}$	air outlet specific enthalpy [$J \cdot kg^{-1}$]
$h_{a,s1}$	saturated air specific enthalpy at coolant inlet temperature [$J \cdot kg^{-1}$]
$h_{a,s2}$	saturated air specific enthalpy at coolant outlet temperature [$J \cdot kg^{-1}$]
h_{dr}	drain specific enthalpy [$J \cdot kg^{-1}$]
h_m	mass transfer coefficient [$kg\ m^{-2}\ s^{-1}$]
J	nucleation rate [$nuclei\ cm^{-3}\ s^{-1}$]

J_0	kinetic constant [nuclei cm^{-3} s^{-1}]
k	Boltzmann constant [J K^{-1}]
k_{cu}	copper thermal conductivity [$W \cdot m^{-1} \cdot K^{-1}$]
L	latent heat of phase changing [J]
l	tube length [m]
Le	Lewis Number [/]
$Le^{2/3}$	Lewis Factor [/]
$\dot{m}_a$	air mass flow rate [$kg \cdot s^{-1}$]
$\dot{m}_{dr}$	condensate water drain rate [$kg \cdot s^{-1}$]
MER	Moisture Extraction Rate [$kg \cdot s^{-1}$]
$\dot{m}_r$	refrigerant mass flow rate [$kg \cdot s^{-1}$]
$\dot{m}_v$	vapor mass flow rate [$kg \cdot s^{-1}$]
m_w	mass of water [kg]
N	number of tube rows [/]
P_{cycle}	power of a dryer cycle [W]
P_{fan}	fan power [W]
p_r	tube pitch between rows [m]
p_t	tube pitch between tubes [m]
Q_a	air heat transfer rate [W]
Q_{diss}	dispersion heat transfer rate [W]
Q_{dr}	drain heat transfer rate [W]
Q_{lat}	latent heat transfer rate [W]
$Q_{m,d}$	mean heat transfer rate in dry conditions [W]
$Q_{m,w}$	mean heat transfer rate in wet conditions [W]
Q_{sens}	sensible heat transfer rate [W]
Q_w	water heat transfer rate [W]
r	radius [m]
r_c	critical radius [m]
r_e	tube external radius [m]
Re_{D0}	Reynolds Number at D_0 [/]
Re_w	water Reynolds Number [/]
r_i	tube internal radius [m]
S	entropy [$J \cdot K^{-1}$]
SAE_c	standard annual energy consumption [$kWh \cdot year^{-1}$]

s_f	fin spacing [m]
SMER	Specific Moisture Extraction Rate [$kg \cdot J^{-1}$]
T	temperature [K]
$t_{a,amb}$	air ambient temperature [°C]
$t_{a,in}$	air inlet temperature [°C]
$t_{a,out}$	air outlet temperature [°C]
T_c	equilibrium transformation temperature [K]
t_{dry}	drying time [min]
$t_{w,in}$	inlet water temperature [°C]
$t_{w,out}$	outlet water temperature [°C]
U_d	overall heat transfer coefficient in dry conditions [$W \cdot m^{-2} \cdot K^{-1}$]
U_w	overall heat transfer coefficient in wet conditions [$W \cdot m^{-2} \cdot K^{-1}$]
$U_{w,m}$	modified overall heat transfer coefficient in wet conditions [$W \cdot m^{-2} \cdot K^{-1}$]
V_m	molar volume [$m^3 \cdot mol^{-1}$]
w_a	air velocity [$m \cdot s^{-1}$]
$w_{a,fr}$	frontal air velocity [$m \cdot s^{-1}$]
$w_{a,in}$	inlet air velocity [$m \cdot s^{-1}$]
x	absolute humidity [$kg_v \cdot kg_a^{-1}$]
$x_{a,in}$	air inlet absolute humidity [$kg_v \cdot kg_a^{-1}$]
Greek symbols	
α_e	external convective heat transfer coefficient [$W \cdot m^{-2} \cdot K^{-1}$]
α_i	internal convective heat transfer coefficient [$W \cdot m^{-2} \cdot K^{-1}$]
β_f	surface roughness ratio [/]
γ	surface tension [$N \cdot m^{-1}$]
γ_{LG}	liquid-gas interface tension [$N \cdot m^{-1}$]
γ_{SG}	solid-gas interface tension [$N \cdot m^{-1}$]
γ_{SL}	solid-liquid interface tension [$N \cdot m^{-1}$]
ΔG^*	Gibbs free energy variation at critical radius [J]
$\Delta G^*_{heterogeneous}$	heterogeneous Gibbs free energy variation at critical radius [J]
$\Delta G_{heterogeneous}$	heterogeneous Gibbs free energy variation [J]
ΔG_r	total free energy variation [J]
$\Delta G_{surface}$	surface Gibbs free energy variation [J]
ΔG_v	Gibbs free energy variation referred to molar volume [J]
ΔG_{volume}	volume Gibbs free energy variation [J]

Δh_{ml}	log-mean enthalpy difference [J·kg^{-1}]
ΔT	temperature difference [K]
Δt_{ml}	log-mean temperature difference [K]
δ	relative discrepancy [/]
θ	contact angle [°]
θ_a	advancing contact angle [°]
θ_c	Cassie contact angle [°]
θ_r	receding contact angle [°]
θ_t	tilt angle [°]
θ_w	Wenzel contact angle [°]
ρ_a	air density [kg·m^{-3}]
Ω^*_e	external heat transfer surface efficiency [/]

1 Introduction

1.1 European background

The EU-28 population overcame the threshold of 500 million in 2008 and reached the 510 million inhabitants in 2016 [1]. Considering the population density, the EU-28 reached the value of 117 inhabitants/km^2 in 2016, being one of the most densely populated zone in the world. From 2000 to 2016, the EU-28 gross domestic product (GDP) had increased, contributing to a 21.7% share of the world's GDP. In the same period, the EU-28 import and export of goods had doubled their values, making the EU-28 a net exporter. This wealth is partially reflected in the final energy consumption during 2000-2016, shown in Fig. 1.1.

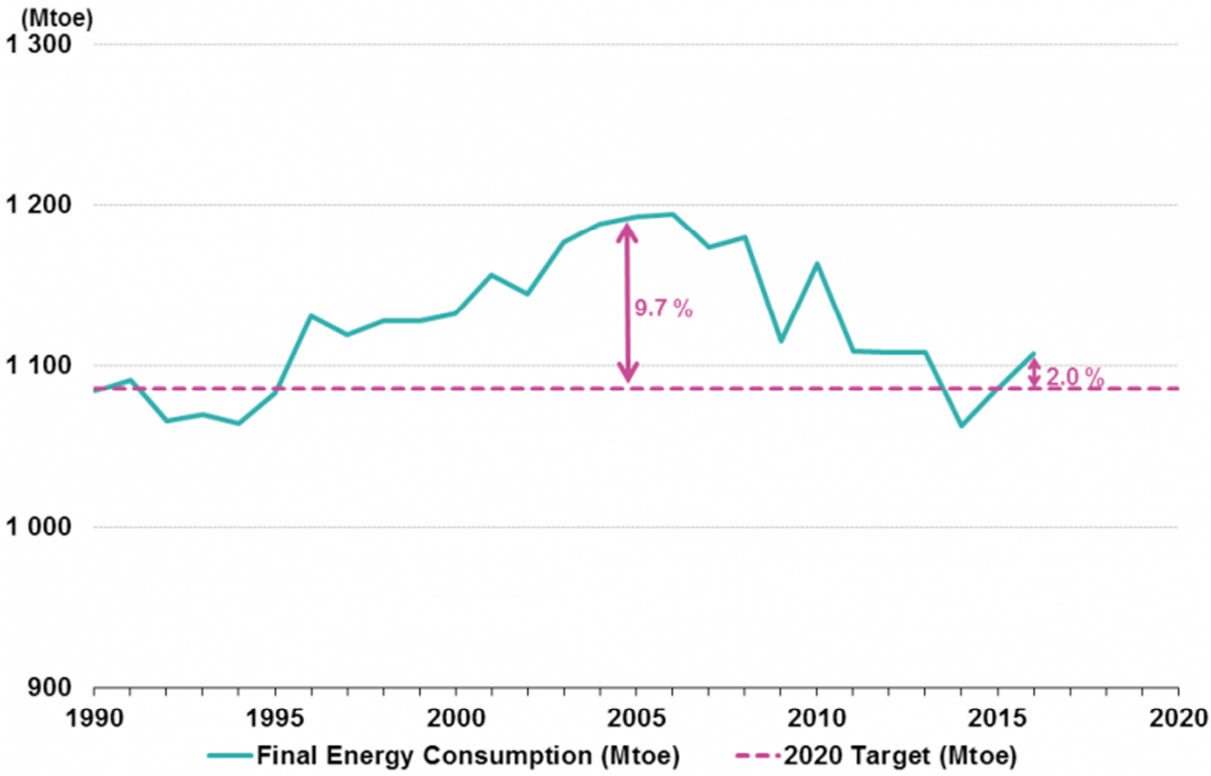

Fig. 1.1 EU-28 final energy consumption [1]

As can be seen from Fig. 1.1, this parameter is substantially increased until 2008, when the financial crisis occurred. The following descending trend from 2010 to 2014 is mainly characterized by the introduction of the "Europe2020" strategy, explained in the Directive 2012/27/EU [2]. This policy aims to reach a 20% reduction of the EU-28 primary energy consumption at 2020 from the projected value evaluated in 2007. A target of 1078 Mtoe has been fixed for the final energy consumption at 2020 and the last available value (2016) is very close to this target. The European Commission has also introduced a framework for 2030 that establishes new targets for climate and

energy parameters [3]. For the greenhouse gas emissions, a 40% reduction of the 1990 levels should be achieved. Following, the share of renewable energies on the overall 2030 energy consumption has been fixed at least 27%. At last, an improvement of the energy savings by 2030 has been endorsed at least 27%. Among the final energy consumption, it is interesting to observe the EU-28 final electricity consumption distribution from 1990 to 2015 between main sectors, shown in Fig. 1.2.

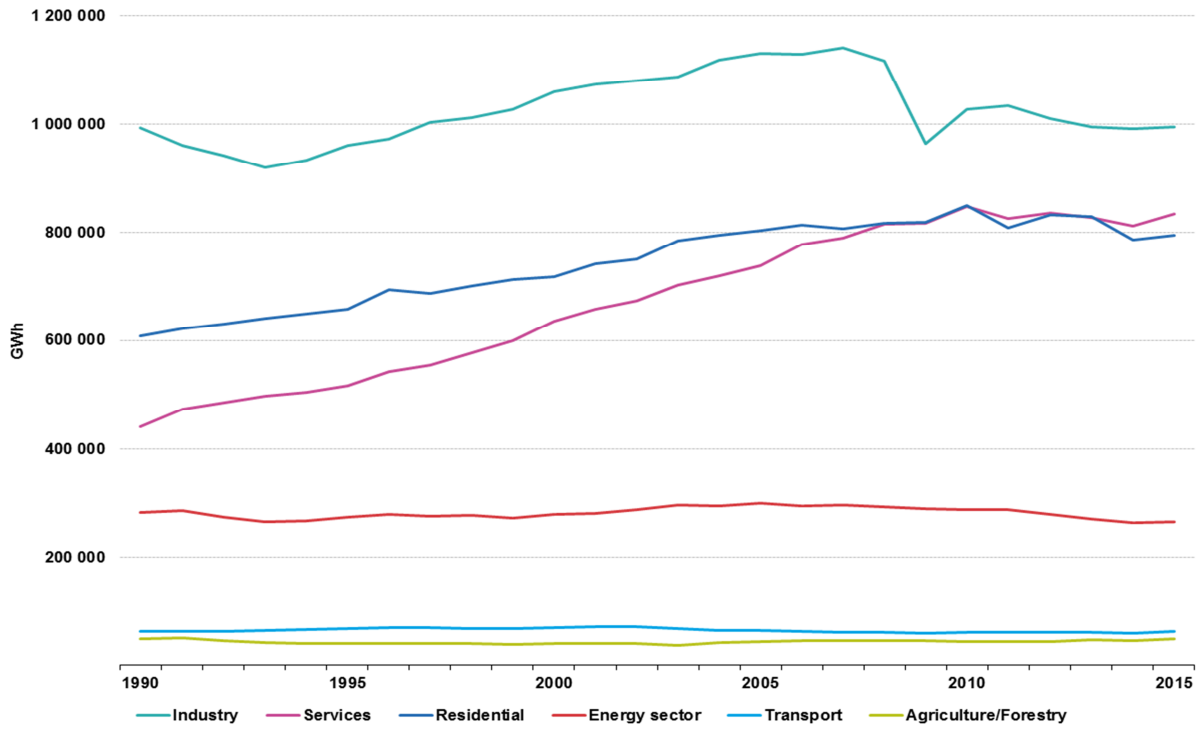

Fig. 1.2 EU-28 final electricity consumption [1]

Considering as reference 1997, it can be seen from Fig. 1.2 that only the services and residential sectors have increased their electric energy consumption. The relevance of the electricity demand in the residential sector is also shown in Fig. 1.3. The scenario represented in Fig. 1.3 highlights the principal role of gas and electricity into residential energy demand up to 2050 [4]. In particular, the electricity consumption will approximately increase of 25% from 2010.

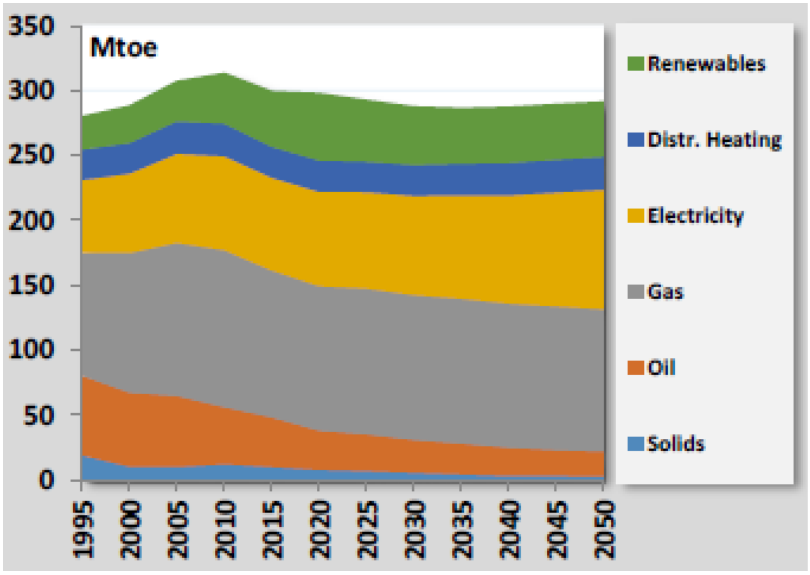

Fig. 1.3 EU-28 residential energy consumption by fuel [4]

Looking at the residential energy demand divided by use, shown in Fig. 1.4, the scenario shows an increase of the usage of electricity for appliances from 2010 up to 2050.

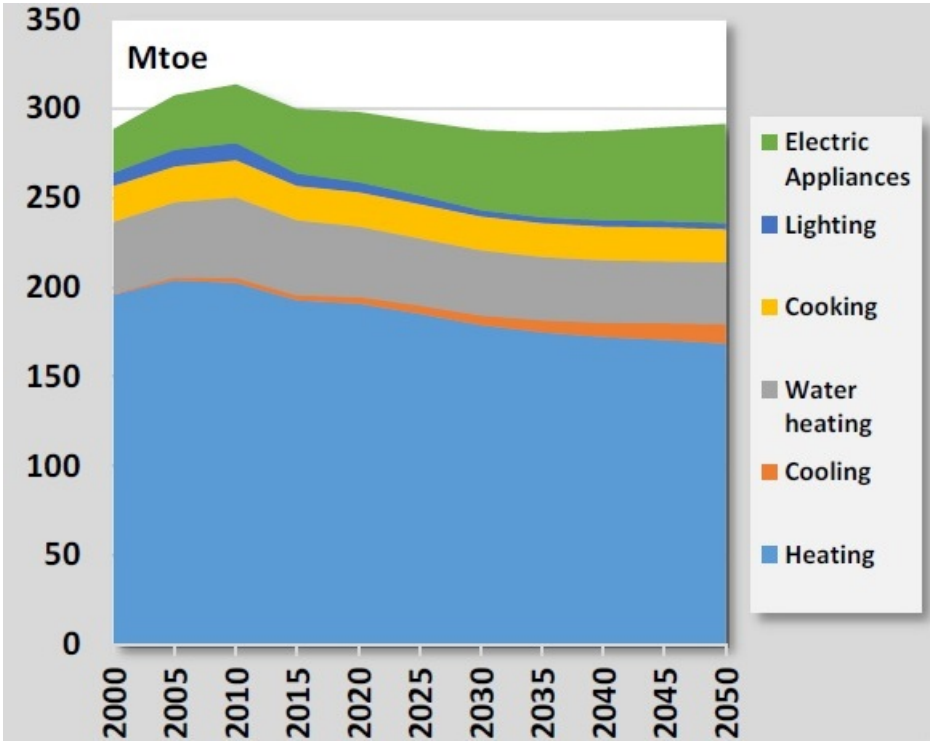

Fig. 1.4 EU-28 residential energy consumption by use [4]

Both Fig. 1.3 and Fig. 1.4 present the energy demand peak between 2010 and 2015. As same as Fig. 1.1, the following descending trend is mainly influenced by the introduction of the Ecodesign Regulations and the European Energy Efficiency Directive 2012/27/EU.

1.2 European Ecodesign Regulation

Ecodesign, also called "sustainable design", is the philosophy of designing products in order to optimise their environmental performance, maintaining unchanged their functional qualities. This behaviour aims to improve the environmental performance of the product throughout its life cycle. The European Directive 2009/125/EC [5] has been introduced in order to establish a framework for the setting of ecodesign requirements for energy-related products. The directive policy tries to counteract the electricity increasing demand and aims to achieve the greenhouse emission targets of EU-28 at 2020. The Directive focuses on the product design phase, that appears to be crucial in order to reduce the future environmental impact during the product's life cycle. A common regulation between the Member States of EU-28 could help the manufactures in applying the implementing measures and it also fulfils the principles of fair competition. The products have to satisfy some criteria in order to be involved into this Directive. For example, the product shall be presented in a significant volume of sales and trade within the Community, about more than 200000 units a year. Furthermore, it must have a significant environmental impact within the Community, showing potential for improvements in terms of environmental impact without entailing excessive costs. The implementing measures should not have negative impact on the functionality of the product from the prospective of the user and on the industry's competitiveness.

1.3 Energy labelling Regulation

The EU Regulation 2017/1360 [6] establishes a framework for the labelling of products placed on the market or put into service that have an impact on energy consumption during their use. This Regulation is addressed both to the industry and to the customers. From the industry point of view, this policy aims to promote innovation and investments in energy efficiency in order to gain competitiveness in the market. From the customer's side, the Regulation provides additional information on the specific energy consumption of the product and it aims to help the customer's choice for less energy consumption products. In order to facilitate the choice between products in terms of energy efficiency, a standardize mandatory label is provided in addition to the product information sheet. The existing label used for this purpose is conforming to the one adopted by Directive 2010/30/EU [7] for energy-related products. An example of this label is shown in Fig. 1.5.

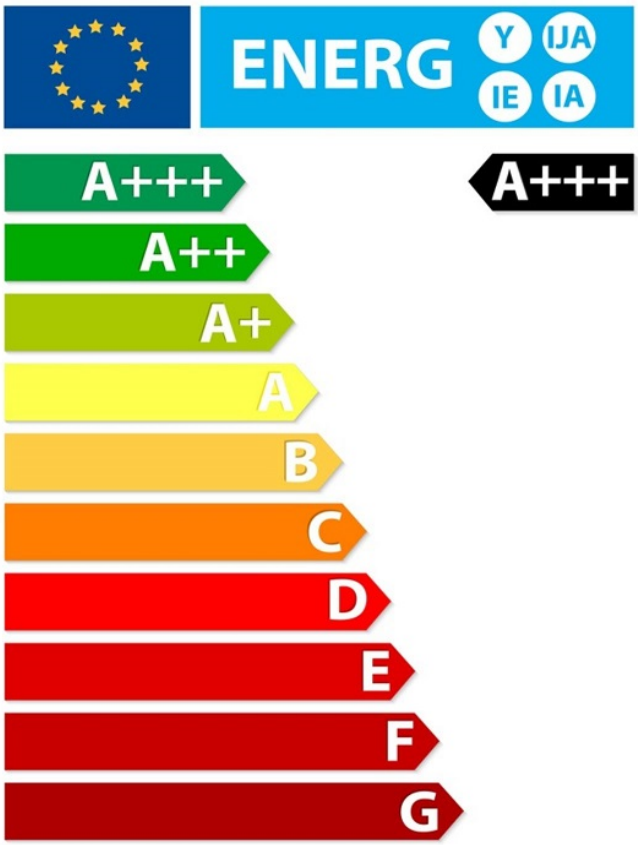

Fig. 1.5 EU Energy Efficiency Label [7]

The label presents a range of energy classes (from G to A) associated to a range of colours (from dark red to dark green). Each step between classes should represent significant cost and energy savings. In addition to the colours scale, the absolute energy consumption has to be indicated to help customers in the evaluation of their energy bills. The label is subjected to periodical rescaling that should take into account two main key factors: the percentage of products sold in the top classes and the technological progress. When the rescaling takes place, the top classes should remain empty to encourage the product innovation process.

1.4 EU Ecolabel: food retail stores

Following the EU Ecodesign Directive, the introduction of an EU Ecolabel has been set through the adoption of Regulation No 66/2010 [8]. This Regulation is strictly related to the Ecodesign Directive and follows the Community policy on sustainability. The strategy aims to promote products with a high level of environmental performance and establishes the criteria for evaluating and applying an EU Ecolabel for them. This policy has been introduced in order to promote the production and consumption of products having a reduced environmental impact along their life cycle. The labelling procedure is characterized by a voluntary initiative from the stakeholders

carried out under the supervision of the European Union Ecolabelling Board (EUEB). In this context, the European SuperSmart project has been instituted in order to remove non-technological barriers in food retail sector, to raise the expertise level for eco-energy supermarkets and to evaluate and start the procedure for establishing an EU Ecolabel for food retail stores [9]. Food retail stores located all across Europe request a large amount of energy that involves different kind of systems, such as heating, cooling and ventilation. In particular, food retail stores contribute in significant share of the EU-28 electricity consumption; for example, around 3% in Germany and near to 4% in France. Another important factor concerning food retail stores is their role concerning the greenhouse gas emissions. Both the direct emissions and the indirect emissions are relevant: the first ones are due to refrigerant leakages, the second ones are caused by the high energy consumption of the stores. One of the first activities of SuperSmart project engaged the supermarket stakeholders in a survey for collecting their attitudes for different themes. The perception towards non-technological barriers has been investigated, focusing in particular on the legislative aspect. The legislative barrier is described as the lack of legislation that considers the supermarket system as a whole. This fact hinders the promotion of energy-efficient supermarkets as a whole and do not punish inefficient ones. Questions are posed about the major legislative EU acts promoting environmentally friendly technologies in the food retail HVAC&R systems. At first, the attitude towards the F-gas regulation has been investigated. The strongest barrier under the F-gas regulation is identified in the lack of qualified personnel for system servicing, which is evaluated as being of importance especially in the South West Europe. Also, the lack of awareness of possible alternatives to HFCs is a medium strength barrier in South Europe. At last, there seems to be a good awareness level of the existence of suppliers for HFC-free systems. The complexity in the legislative framework is considered an important barrier all over Europe, especially in the South West Europe. The expected impact of the EU Ecolabelling for rood retail stores from the stakeholders point of view has been investigated. All respondents, except food retail chains, are quite confident that it could improve their own financial success and sales number. Food retail chains suppose to be the final group implementing the Ecolabel and they believe that this regulation will provide no added value to their customers. However, they are the most aware group regarding the impact on the carbon footprint of their services. They also assert that the Ecolabel would not overload too much their everyday workload and they are aware of the need for training for their staff. System manufactures and components suppliers are quite positive with respect to the impact of the Ecolabel on sales number and the added value of their products. They also seem to be quite ready for the label, as they do not foresee too much impact on the need for training or everyday workload. Servicing, repairing and maintenance stakeholders think that the EU Ecolabel could have

an impact on the carbon footprint of their services and that it will require more training for themselves, although the impact on their workload won't be so relevant. Associations are very cautions and they do not think that the EU Ecolabel might have any significant impact on any aspect of their work. Universities and research institutes imagine an important influence of the EU Ecolabel on their financial success through the added value they can provide.

1.5 EU Ecolabel: household tumble dryers

According to the Ecodesign Directive, the European Commission has introduced regulated measures for some domestic appliances, including household tumble dryers. This domestic appliance meets the prerequisites expresses in the Ecodesign Directive. The sales of household tumble dryers have been estimated at 5.1 million units in 2005, for a global value of 2.2 billion euro; an increase up to 5.9 million units in 2020 will be expected [10]. The energy consumption during use phase has been identified as the main parameter regarding the environmental impact. In 2005, the EU-28 total energy consumption of household tumble dryers has been estimated at 21 TWh and an increase up to 30 TWh in 2020 will be expected. Regulation No 932/2012 [8] has been adopted in order to establish ecodesign requirements for household tumble dryers. The introduction of ecodesign requirements does not have any effect on the product functionality from the end-user's prospective and it should be applied gradually in order to allow manufactures to redesign their products. The calculation of the energy consumption and other parameters of household tumble dryers considers a "standard cycle" which dries cotton laundry having an initial moisture content of 60% to a remaining value of 0%. This type of cycle has to be clearly identified in the appliance under the denomination "standard cotton programme". In the booklet of instructions, the manufacturer shall supply information about the "standard cotton programme" together with the programme time and the energy consumption for main drying programmes at both full and partial load. Regulation No 392/2012 [11] identifies two key parameters for comparing different types of household tumble dryers. The first one is the energy efficiency index (EEI), calculated according to Eq. 1.1.

$$EEI = \frac{AE_c}{SAE_c} \times 100 \tag{1.1}$$

where:

- AE_c: weighted annual energy consumption of the household tumble dryer [kWh/year];
- SAE_c : standard annual energy consumption of the household tumble dryer [kWh/year].

These two last terms are evaluated according to the type of household tumble dryer. The second key parameter is the weighted condensation efficiency. The condensation efficiency is the ratio between

the mass of moisture condensed and drained in the container of a condenser household tumble dryer and the mass of moisture removed from the load by the specific programme. This mass of moisture removed from the load is calculated as the difference between the mass of the wet test load before and after drying. The weighted condensation efficiency considers the average condensation efficiency of the standard cotton programme at both full and partial load, as expressed by Eq. 1.2:

$$C_t = (3 \times C_{dry} + 4 \times C_{dry1/2}) / 7 \tag{1.2}$$

where:

- C_{dry} : average condensation efficiency of the standard cotton programme at full load;
- $C_{dry1/2}$: average condensation efficiency of the standard cotton programme at partial load.

The specific ecodesign requirements for household tumble dryers, provided by the Regulation No. 392/2012 [12], establish that:

- from 1 November 2013, the energy efficiency index (EEI) shall be less than 85 and, for condenser household tumble dryers, the weighted condensation efficiency shall be not lower than 60%;
- from 1 November 2015, for condenser household tumble dryers, the EEI shall be less than 76 and the weighted condensation efficiency shall be not lower than 70%.

Based on these two parameters, two classifications for household tumble dryers were developed, as shown in Table 1.1 and Table 1.2.

Table 1.1

Energy efficiency classes

Energy efficiency class	Energy Efficiency Index (EEI)
A+++ (most efficient)	EEI < 24
A++	24 ≤ EEI < 32
A+	32 ≤ EEI < 42
A	42 ≤ EEI < 65
B	65 ≤ EEI < 76
C	76 ≤ EEI <85
D (least efficient)	85 ≤ EEI

Table 1.2

Condensation efficiency classes

Condensation efficiency class	Weighted condensation efficiency
A (most efficient)	$C_t > 90$
B	$80 < C_t \leq 90$
C	$70 < C_t \leq 80$
D	$60 < C_t \leq 70$
E	$50 < C_t \leq 60$
F	$40 < C_t \leq 50$
G (least efficient)	$C_t \leq 40$

An example of label for condenser household tumble dryers is represented in Fig. 1.6.

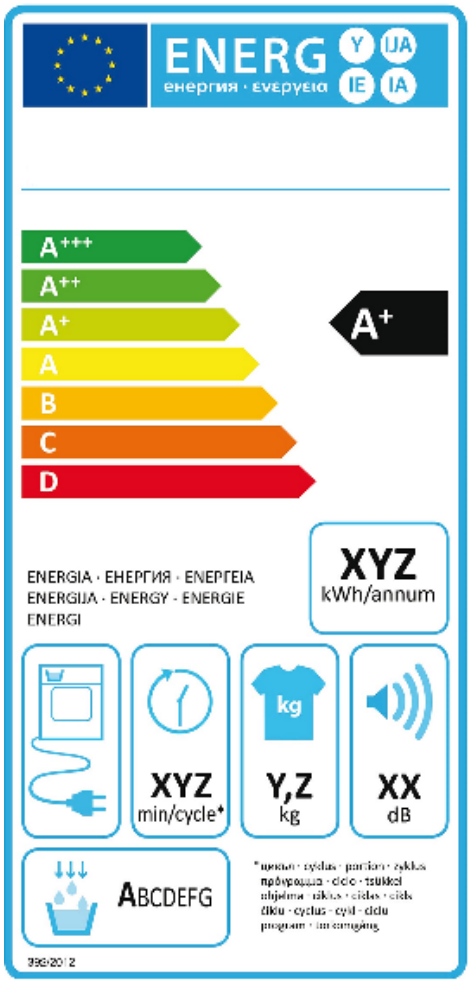

Fig. 1.6 Label for condenser household tumble dryer [12]

As illustrated from Fig. 1.6, the following information shall be included in the label:

- supplier's name or trade mark;

- supplier's model identifier (alphanumeric code);
- the energy efficiency class;
- weighted annual energy consumption AE_c [kWh/year];
- information on the type of household tumble dryer;
- cycle time referring to the standard cotton programme at full load [min];
- rated capacity for the standard cotton programme at full load [kg];
- the sound power level during the drying phase for the standard cotton programme at full load [dB];
- the condensation efficiency class.

1.6 References

[1] Eurostat. "Energy, transport and environment indicators", 2017 edition.

[2] Directive 2012/27/EU of the European Parliament and of the Council of 25 October 2012.

[3] European Council 23/24 October 2014 - Conclusions.

[4] European Commission. "EU Reference Scenario 2016 - Energy, transport and GHG emissions: trends to 2050".

[5] Directive 2009/125/EC of the European Parliament and of the Council of 21 October 2009.

[6] Regulation (EU) 2017/1369 of the European Parliament and the Council of 4 July 2017.

[7] Directive 2010/30/EU of the European Parliament and of the Council of 19 May 2010.

[8] Regulation (EC) No 66/2010 of the European Parliament and of the Council of 29 November 2009.

[9] Minetto S., Marinetti S., Saglia P., Masson N., Rossetti A..Non-technological barriers to the diffusion of energy efficient HVAC&R solutions in the food retail sector. Int. J. of Refrigeration 86 (2018), 422-434.

[10] Commission Regulation (EU) No 932/2012 of 3 October 2012.

[11] European Commission, Commission staff working document - impact assessment implementing Directive 2009/125/EC.

[12] Commission Regulation (EU) No 392/2012 of 1 March 2012.

2 Heat pump tumble dryer

2.1 Technology description

The main technology used for drying textiles in non-professional environments is the tumble dryer. The traditional technology of domestic tumble dryers, based on opened or closed air cycle, has involved the use of electrical heaters to warm up the process air before the entrance in the drum. For an open air cycle configuration, the system is called "air-vented tumble dryer". In a closed loop configuration, the humid air at the exit of the drum is typically dehumidified in a heat exchanger, where the cooling fluid can be external air or tap water; the system is so called "condenser tumble dryer". Among this last type of systems, heat pump tumble dryer (HPTD) technology is the most energy-efficient. In this configuration, a heat pump unit provides heating up and dehumidification of the process air at the same time, as shown in Fig. 2.1.

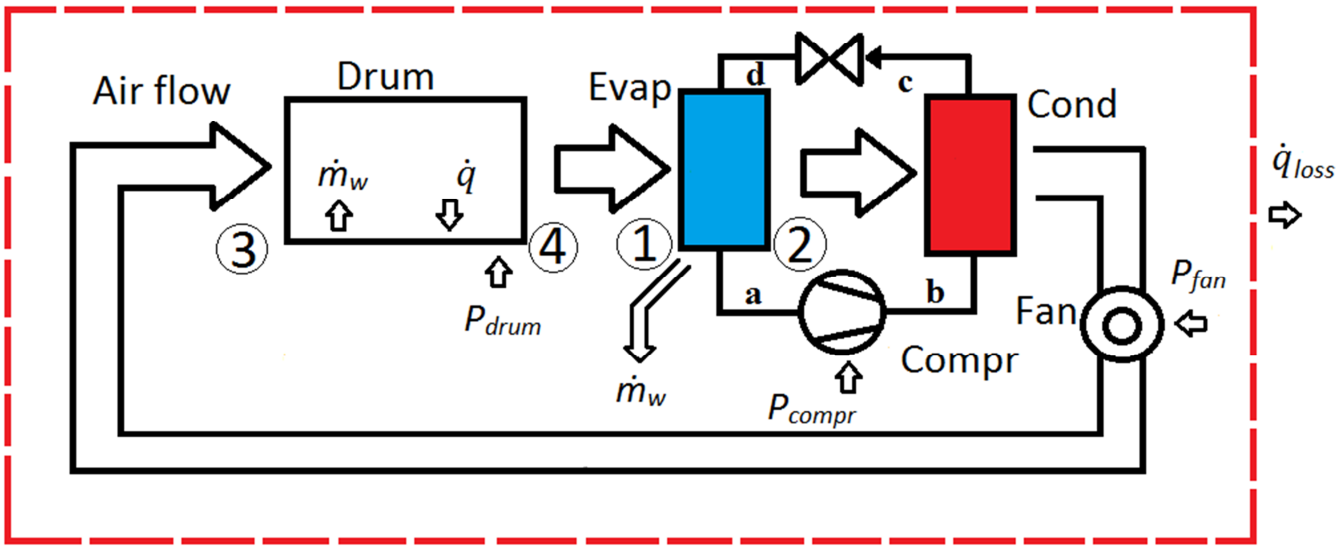

Fig. 2.1 Heat pump tumble dryer (HPTD) layout

The air entering the drum (3) heats up the clothes and causes the removal of moisture from them. Then, the humid air (4) is sent to the heat pump evaporator where the dehumidification process takes place (1-2). When flowing through the condenser, the air flow increases its temperature before re-entering in the drum, enhancing the capability of humidity retention. In Fig. 2.1, the main power inputs are also represented, as heat gains and heat losses of the system, together with the overall water mass balance. In Fig. 2.2, the humid air transformations are represented in the psychrometric chart. The heating of the air flow in the condenser occurs at constant humidity ratio (2-3). Then, the drying process in the drum increases the air humidity ratio and reduces its temperature (adiabatic

saturation). In the evaporator (1-2), the dehumidification process takes place (cooling and dehumidification) and the air reaches the condenser near the saturation conditions. The energy balance of the air cycle is achieved taking into account some thermal losses that occur between the exit of the drum and the inlet of the evaporator (4-1).

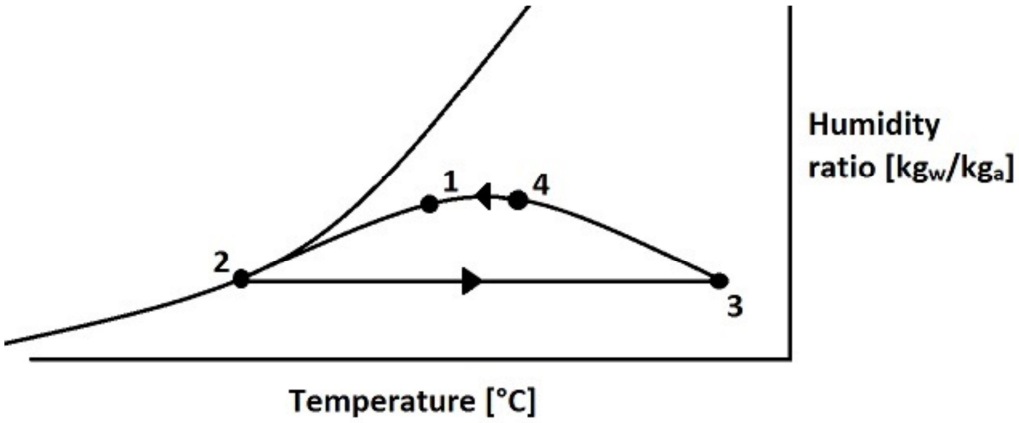

Fig. 2.2 Thermodynamic transformation of air in a HPTD

The heat pump unit is a vapor-compression cycle that includes a compressor, evaporator, condenser and expansion valve. In Fig. 2.3, the thermodynamic transformations of the working fluid in the heat pump unit are represented.

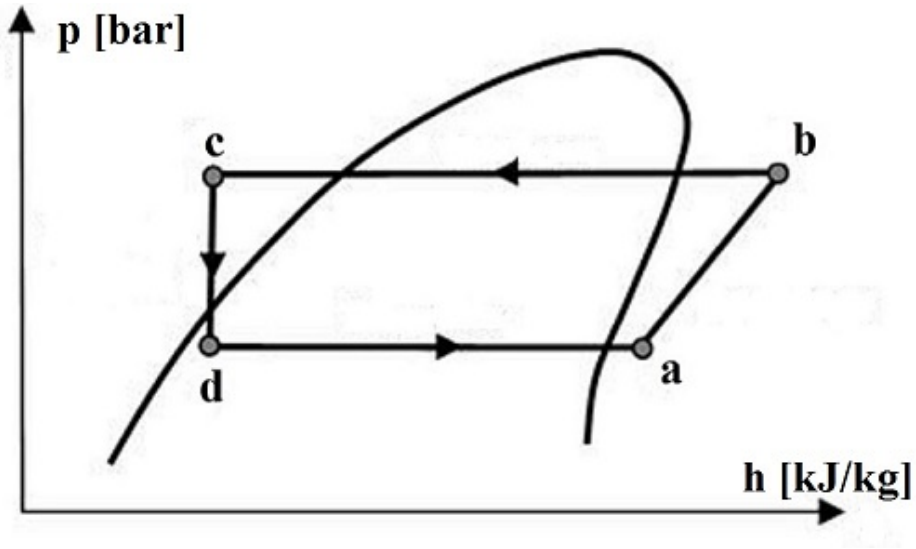

Fig. 2.3 Thermodynamic transformation of refrigerant in HPTD

Compression of the refrigerant (a-b) is realized in the compressor, increasing its temperature and pressure. In the condenser (b-c), the working fluid is involved in the process of desuperheating (until the right side of the saturation curve), condensing (until the left side of the saturation curve) and subcooling. After the condenser, the fluid passes through a throttling device (c-d), reducing its

pressure. In the evaporator (d-a), the fluid absorbs heating from the hot humid air and vaporizes, reaching a superheated state at the compressor inlet.

2.2 Drying process

As shown in Fig. 2.1, the clothes drying into the drum (3-4) involves two main physical processes between the hot air and the wetted clothes. The first one is the heat supply from the air to the clothes in order to evaporate the moisture from their surface. This evaporation involves a second process of mass transfer of water from the clothes to the air due to the different concentration of moisture between them. The heat pump tumble dryer working cycle is typically a transitory process. For this reason, the moisture evaporation rate from the clothes to the air changes along the overall working cycle. A characteristic evaporation rate profile is represented in Fig. 2.4.

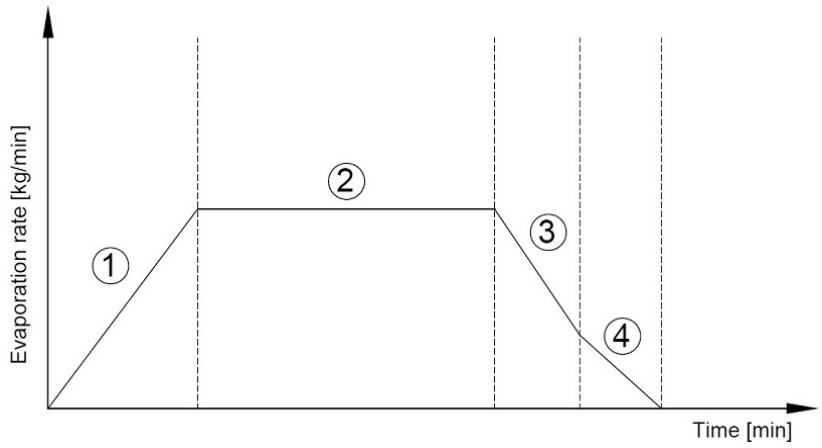

Fig. 2.4 Evaporation rate profile of a drying process

In Fig. 2.4, the curve can be divided into four main regions that present different trends. At the beginning of the process, the heat supply promotes the heating of the moisture inside the clothes in order to increase the water concentration on the their external surface (zone 1). At the end of this first phase, the mass transfer of water from the clothes surface to the air reaches a maximum value. The high concentration of moisture forms a thin film of water on the clothes surface that keeps constant the maximum evaporation rate value until the critical moisture point is reached (zone 2). After, the clothes surface begins to totally dry in some regions, leading to a first drop of the evaporation rate (zone 3). Following, the moisture concentration on the clothes surface drops further due to the continuous expansion of the dry regions all over the clothes surface (zone 4). The drying process ends with the complete removal of moisture from the clothes. Same profiles of the evaporation rate curve are found by Bansal [1], [2] and by Bengtsson [3].

2.3 Performance criteria

Several criteria are used to measure the performance of a heat pump tumble dryer. The first parameter presented in this analysis is the coefficient of performance (COP) of the heat pump unit, as following defined in Eq. 2.1:

$$COP = \frac{h_b - h_c}{h_b - h_a} \tag{2.1}$$

where h is the enthalpy of the refrigerant and the subscripts are referred to points of Fig. 2.1. This parameter considers only the air heating as useful effect of the process. A second criteria used for performance comparing is the moisture extraction rate (MER), defined in Eq. 2.2.

$$MER = \dot{m}_a \cdot (x_4 - x_3) \tag{2.2}$$

In Eq. 2.2, $\dot{m}_a$ is the air mass flow rate, x_4 and x_3 are, respectively, the air absolute humidity at the outlet and at the inlet of the drum. Considering the MER indicator, the drying time of the dryer can be defined as:

$$t_{dry} = \frac{m_w}{MER} \tag{2.3}$$

where m_w is the amount of water removed from the test load over the entire cycle. Another relevant comparing parameter is the specific moisture extraction rate (SMER), expressed in Eq. 2.4:

$$SMER = \frac{MER}{P_{cycle}} \tag{2.4}$$

where P_{cycle} is the total power consumed over the entire working cycle. A high SMER indicates an efficient drying process.

2.4 Heat pump evaporator

The dehumidification process of the hot humid air coming out from the drum takes place in the heat pump evaporator. This component is typically a finned coil where the refrigerant flows inside the tubes and the air flows across the external fins. The refrigerant flow inside the evaporator tubes maintains the external surface temperature below the air dew point temperature. As can be seen from Fig. 2.5, the hot and humid air flow reaches the front of the evaporator at state 1, identified by an enthalpy value of h_1 and absolute humidity value of x_1. Passing through the evaporator, the hot humid air is cooled and dehumidified, leading to a drainage of liquid water from the heat exchanger

that falls into a receiver. After the cooling and the dehumidification process, the air flow leaves the evaporator having an enthalpy value of h_2 and an absolute humidity value of x_2 (section 2).

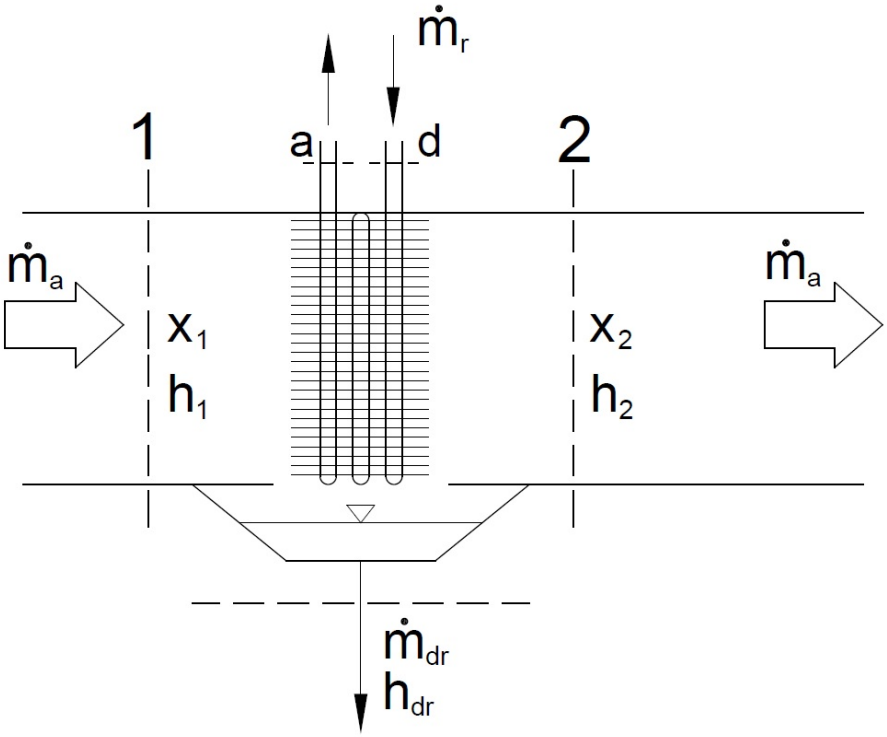

Fig. 2.5 Air cooling and dehumidification

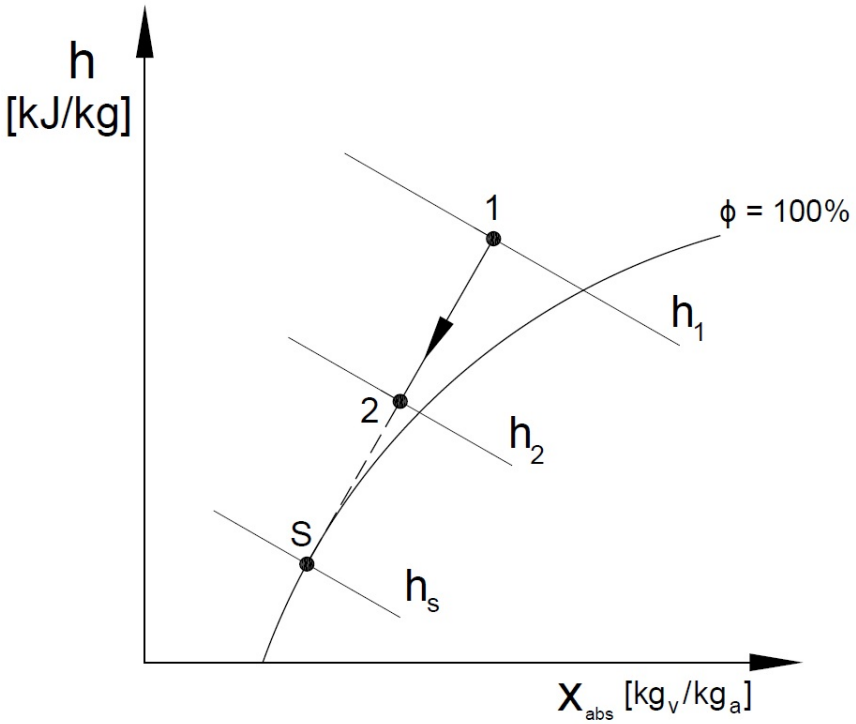

Fig. 2.6 Mollier diagram: cooling and dehumidification

Referring to Fig. 2.5, an energy balance can be applied at steady state conditions (Eq. 2.5):

$$\dot{m}_r h_d + \dot{m}_a h_1 = \dot{m}_r h_a + \dot{m}_a h_2 + \dot{m}_{dr} h_{dr} \tag{2.5}$$

where h_d and h_a are, respectively, the refrigerant enthalpy at the inlet and at the outlet of the evaporator. The drain water mass flow can be written as follows (Eq. 2.6).

$$\dot{m}_{dr} = \dot{m}_a \cdot (x_1 - x_2) \tag{2.6}$$

Substituting Eq. 2.6 in Eq. 2.5 and rearranging, Eq. 2.7 can be obtained:

$$\dot{m}_r (h_a - h_d) = \dot{m}_a [(h_1 - h_2) - (x_1 - x_2) h_{dr}] \tag{2.7}$$

where the enthalpy h_{dr} is calculated at the drain temperature t_{dr}, having a value closed to t_2. In Fig. 2.6, the dehumidification process is represented in the Mollier diagram. The point S is identified by the external surface temperature of the evaporator (supposed constant) and the saturation curve. The equilibrium state 2 lays on the line between points 1 and S and its position depends on the evaporator geometry and the air flow conditions, as the frontal velocity. The exact position of point 2 can be determined through a parameter called by-pass factor, defined in Eq. 2.8:

$$f_{bp} = \frac{h_2 - h_s}{h_1 - h_2} \tag{2.8}$$

The definition of the by-pass factor derives from considering point 2 as the final state of an adiabatic mixing between two fractions of the global air mass flow. The first one is supposed not passing through the heat exchanger and remains at state 1. The second portion of the global mass flow rate passes through the heat exchanger and reaches the saturation condition S at the outlet. Knowing the by-pass factor, the point 2 of Fig. 2.6 is then identified. The drain water mass flow, expressed in Eq. 2.6, is considered the useful effect of the process. For the same refrigerant side conditions, an improvement of this parameter leads to a more efficient use of this component. A study of the dehumidification process is necessary in order to define the possible actions that should be undertaken for achieving the efficiency improvement.

2.5 References

[1] Bansal P., Islam S., Sharma K. A novel design of a household clothes tumbler dryer, Applied Thermal Eng. 30(2010), 277-285.

[2] Bansal P., Islam S., Sharma K. Thermal analysis of a new concept in a household clothes tumbler dryer, Applied Energy 87(2010), 1562-1571.

[3] Bengtsson P., Berghel J., Renstrom R. Performance study of a closed-type heat pump tumble dryer using a simulation model and an experimental set-up, Drying Tech. 32 (2014), 891-901.

3 Condensation overview

3.1 Homogeneous and heterogeneous nucleation

Condensation is a process of phase changing where a single phase α, in equilibrium at a given temperature and pressure, generates a new phase β due to the external condition variation [1]. The stability between these two phases depends from the Gibbs free energy, i.e. G as molar value [J mol^{-1}]. As shown in Fig. 3.1, there is an equilibrium where the two phases have the same Gibbs free energy ($G_\alpha = G_\beta$) at the same temperature; this temperature value is called "equilibrium transformation temperature".

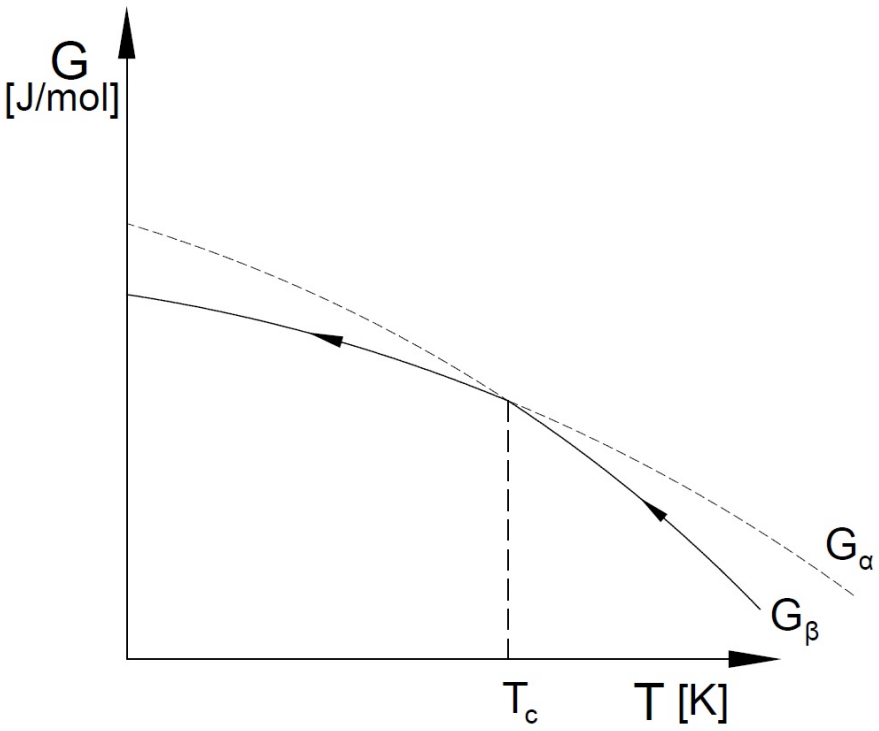

Fig. 3.1 Equilibrium transformation temperature

In order to initiate the phase changing process, an undercooling needs to be applied ($\Delta T = T_c - T$) to the system that generates a difference between the two Gibbs free energies. This difference is the driving force of the process. For small values of the undercooling, the variation of the free energy is expressed by Eq. 3.1:

$$\Delta G(T) = \Delta H - T\Delta S = L - T \cdot \frac{L}{T_c} = \frac{L}{T_c} \cdot \Delta T \tag{3.1}$$

where L is the latent heat of the phase changing (negative value). Thus, the driving force is proportional to the undercooling, as can be seen in Fig. 3.2.

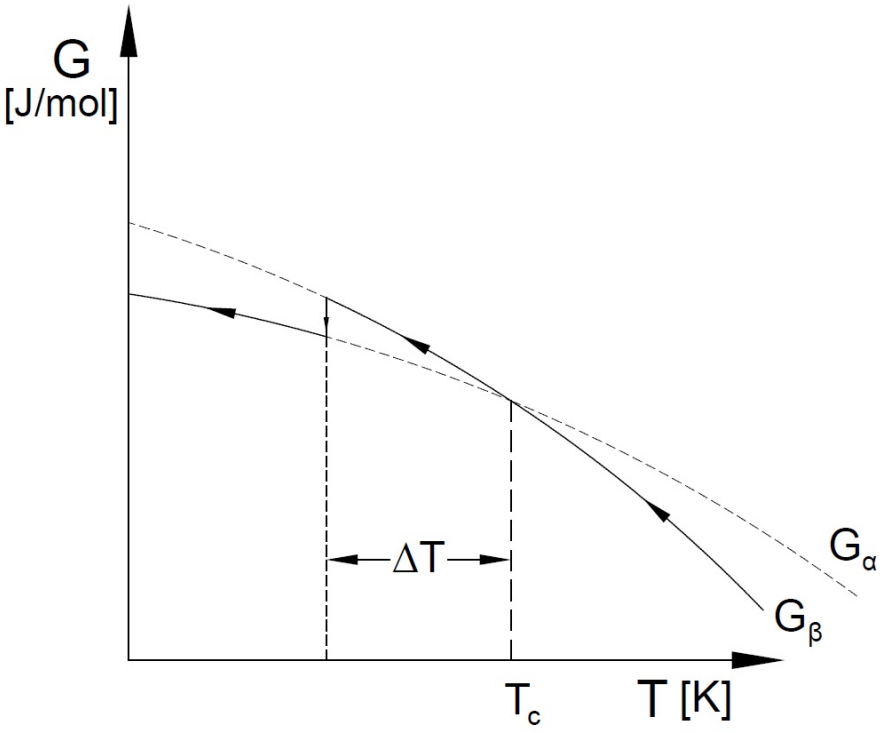

Fig. 3.2 Phase changing due to undercooling

In a homogeneous phase β subject to undercooling, there might be the formation of spherical particles (with radius r) of a new phase α. The free energy variation referring to a volume unit of phase α, considering Eq. 3.1, is expressed by Eq. 3.2:

$$\Delta G_v = \frac{1}{V_m} \cdot \frac{L}{T_c} \cdot \Delta T \tag{3.2}$$

where V_m is the molar volume of phase α. Thus, for the overall spherical particle, the free energy variation ΔG_{volume} is defined in Eq. 3.3:

$$\Delta G_{volume} = \frac{4}{3} \cdot \pi \cdot r^3 \cdot \Delta G_v \tag{3.3}$$

However, the formation of a new particle of phase α originates an interface between the two phases. An additional positive term must be taken into account that is proportional to the surface tension γ [N m^{-1}], expressed in Eq. 3.4:

$$\Delta G_{surface} = 4 \cdot \pi \cdot r^2 \cdot \gamma \tag{3.4}$$

In the end, in order to create a spherical particle of radius r, the total free energy variation ΔG_r required is expressed in Eq. 3.5:

$$\Delta G_r = \Delta G_{volume} + \Delta G_{surface} = \frac{4}{3}\pi r^3 \cdot \Delta G_v + 4\pi r^2 \cdot \gamma \tag{3.5}$$

In Fig. 3.3, ΔG_r is plotted as a function of the radius and it achieves a maximum value when $r = r_c$, that is called "critical radius". This maximum of ΔG_r is a threshold value: if a particle has a radius below the critical one, it will disappear; otherwise, the particle will grow further, having $\Delta G_r < 0$.

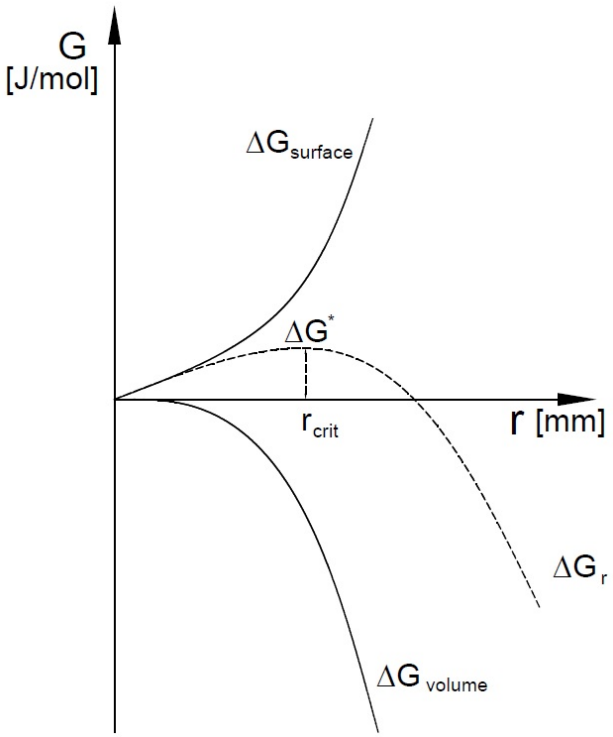

Fig. 3.3 Homogeneous nucleation

The value of the critical radius is expressed in Eq. 3.6, deriving from Eq. 3.5:

$$r_c = \frac{-2\gamma}{\Delta G_v} \tag{3.6}$$

The corresponding value of the free energy variation at r_c is considered a sort of "activation barrier", giving the possibility of nucleation of the new phase, as expressed in Eq. 3.7:

$$\Delta G^* = \frac{16}{3} \cdot \frac{\pi \gamma^3}{\Delta G_v^2} \tag{3.7}$$

Heterogeneous nucleation is the process of nucleation of a new phase that occurs in preferential sites, such as surfaces, grain boundary or impurities. At these sites, for example on surfaces, there is a reduction of the free energy variation surface term because the interface between the substrate and

the new phase is not entirely spherical. Surfaces promote nucleation due to wetting, a property explicated by the contact angle θ between the nucleus and the surface, as represented in Fig. 3.4:

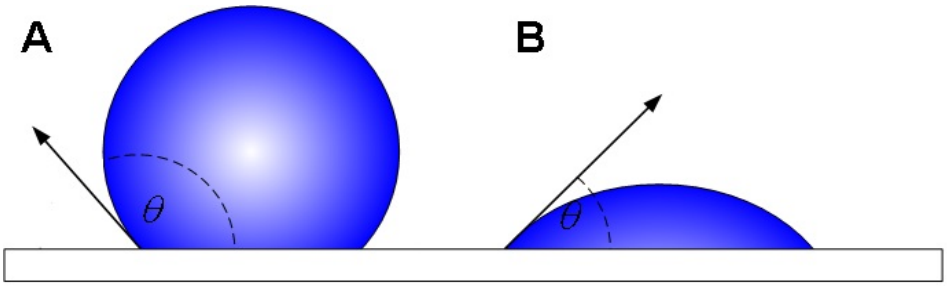

Fig. 3.4 Definition of the contact angle for two different surfaces (A, B) [2]

The total free energy variation for heterogeneous nucleation is equal to the product between the total one for homogeneous nucleation (defined in Eq. 3.5) and a function of the contact angle θ, as expressed in Eq. 3.8:

$$\Delta G_{heterogeneous} = \Delta G_r \cdot f(\theta) \tag{3.8}$$

The function of the contact angle has values between 0 and 1 and it is defined in Eq. 3.9:

$$f(\theta) = \frac{2 - 3 \cdot \cos\theta + \cos^3\theta}{4} \tag{3.9}$$

Being $f(\theta)$ independent from the radius, the critical radius for heterogeneous nucleation is the same one defined for homogeneous nucleation in Eq. 3.6. Besides, the value of the "activation barrier" ΔG^* at the critical radius is lower for heterogeneous nucleation than homogeneous nucleation. This is due to the contact angle that affects the shape of the nucleus. Fig. 3.5 illustrates these considerations.

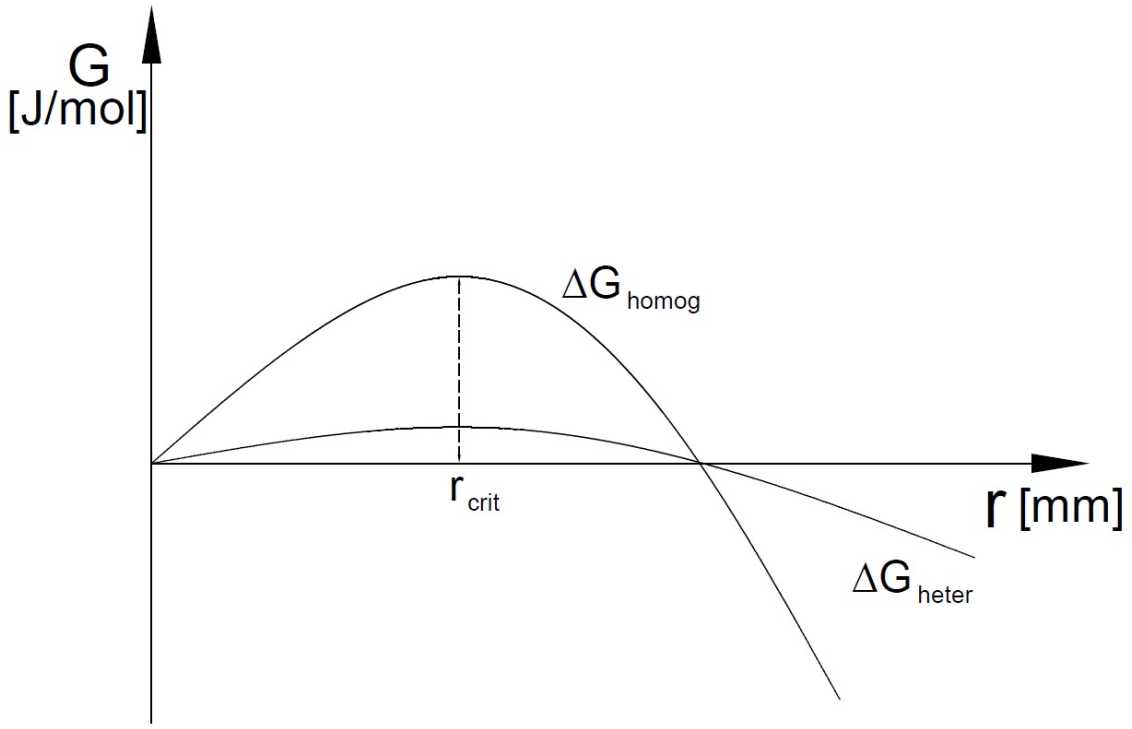

Fig. 3.5 Heterogeneous nucleation

Surface wetting has a high impact on the nucleation rate J of the new phase [nuclei cm^{-3} s^{-1}]. This parameter has an inverse exponential dependence of $\Delta G_{heterogeneous}$, as expressed in Eq. 3.10:

$$J = J_0 \cdot \exp\left(-\frac{\Delta G^*_{heterogeneous}}{k \cdot T_c}\right) \tag{3.10}$$

In Eq. 3.10, J_0 is a kinetic constant (10^{25} nuclei cm^{-3} s^{-1}), k is the Boltzmann constant ($1.38 \cdot 10^{23}$ J K^{-1}), T_c is the condensing temperature [K] and $\Delta G^*_{heterogeneous}$ is the free energy barrier for heterogeneous nucleation [J]. This last term increases with the contact angle of the surface; consequently, the nucleation rate is higher for surfaces with low contact angle. Besides, a small variation of the surface contact angle produces an exponential change of the value of nucleation rate.

3.2 Wettability: models and effects

Wettability represents the ability of a liquid to maintain contact with a solid surface [2]. Surface forces control the wettability on the surface and they may be adhesive or cohesive. Adhesive forces, working between a liquid and a solid, cause the liquid to spread across the surface. Otherwise, the cohesive forces within the liquid cause the drop to avoid contact with the surface. The contact angle θ, previously represented in Fig. 3.4, is the angle at which the liquid-vapour interface meets the solid-liquid interface and it is determined by the resultant between adhesive and cohesive forces.

For a given sessile drop in equilibrium on an ideal surface (flat, rigid, and chemically homogeneous), the net force per unit length acting along the boundary line among the three phases must be zero. The components of net force in the direction along each of the interfaces are given by Young's equation, expressed in Eq. 3.11:

$$\gamma_{SG} = \gamma_{SL} + \gamma_{LG} \cdot \cos\theta \tag{3.11}$$

Eq. 3.11 relates the surface tensions between the three phases and predicts the value of the contact angle knowing the other terms involved. In Fig. 3.6, the relation between the three surface tension is shown:

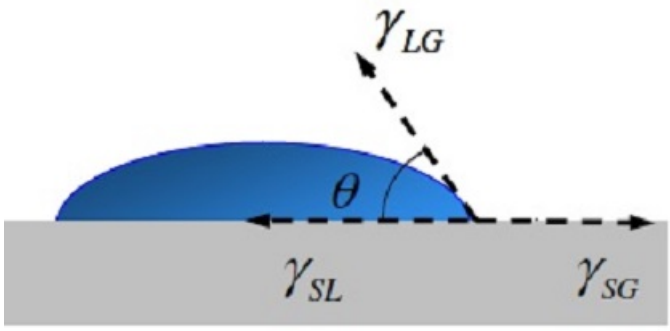

Fig. 3.6 Graphic representation of Young's equation [2]

Real surfaces do not have perfect smoothness or chemical homogeneity and this deviation results in a phenomenon called contact angle hysteresis. The contact angle hysteresis is defined as the difference between the advancing contact angle θ_a and the receding contact angle θ_r, as shown in Fig. 3.7 (θ_t is a generic inclined angle):

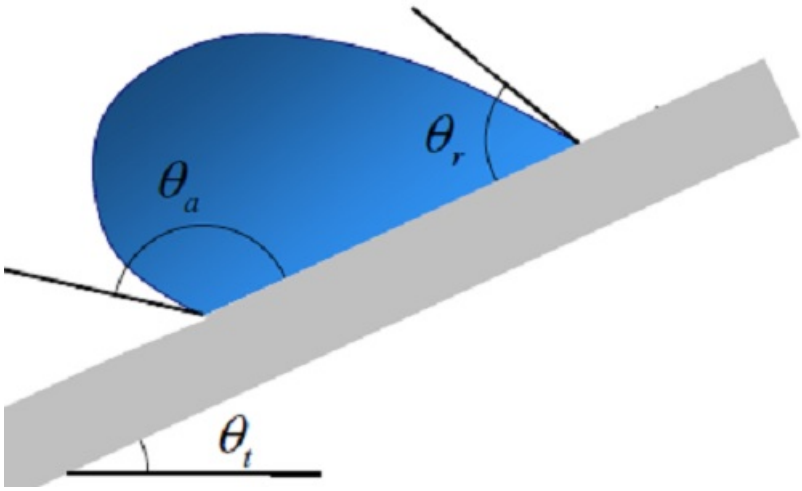

Fig. 3.7. Dynamic contact angles [2]

This phenomenon is essentially the displacement of a triple contact line between the three phases, due to expansion or retraction of the droplet. The advancing contact angle is the maximum stable angle, while the receding contact angle is the minimum stable angle. The hysteresis occurs because there are different thermodynamically stable contact angles on a non-ideal solid surface. The presence of rough texture is another deviation that can characterize a non-ideal surface. There are two different types of rough texture: homogeneous and heterogeneous. The homogeneous type occurs when the liquid fills the grooves of the surface. On the other hand, the heterogeneous one occurs when the droplet is suspended on the rough texture and there is air between the liquid and the surface. When the drop size is sufficiently large compared with the surface roughness scale, two different models can be applied for each of the two wetting regimes. The Wenzel model describes the homogeneous wetting regime and it is summarized by Eq. 3.12:

$$\cos\theta_w = \beta \cdot \cos\theta \tag{3.12}$$

where θ_w is the apparent contact angle corresponding to the stable equilibrium state, β is the roughness ratio (ratio of the true area of the solid surface to the apparent area) and θ is the Young contact angle, defined in Eq. 3.11. In case of heterogeneous wetting regime, the Cassie-Baxter equation explains this type of behaviour , shown in Eq. 3.13:

$$\cos\theta_c = \beta_f \cdot f \cdot \cos\theta + f - 1 \tag{3.13}$$

where β_f is the roughness ratio of the wet surface area and f is the fraction of solid surface area wet by the liquid. Fig. 3.8 gives a simplified representation of the behaviour of a droplet in these two models.

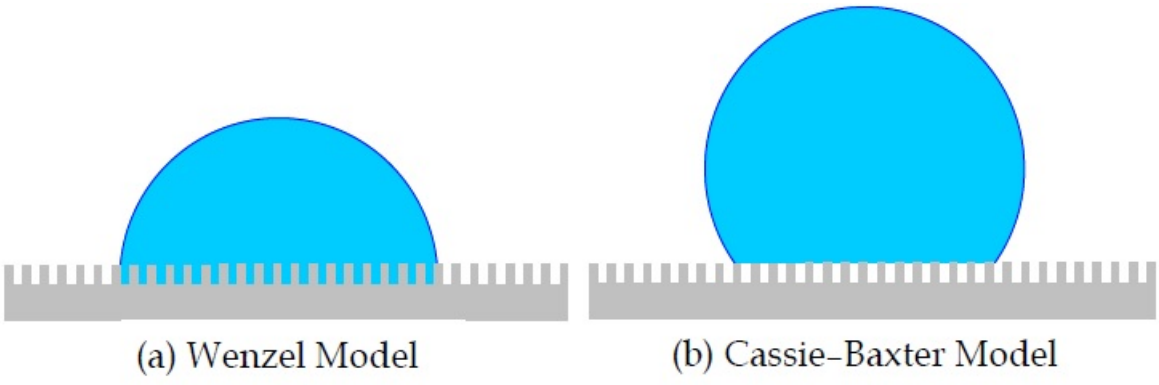

Fig. 3.8 Types of rough surfaces [2]

3.3 Surface coatings

Contact angle ranges from 0° to 180° and each value characterizes a specific surface. Eq. 3.10 highlights the possibility to changing the nucleation rate through the modification of the contact angle of the surface. Considering dehumidification, an increase of the nucleation rate of the condensed phase leads to an increase of the useful effect of the process. For achieving the increase of the drain water mass flow, one of the possible methods could be the usage of a coating applied to the original surface. However, the applied coating should not obstruct the heat transfer process; the thickness of the substrate must be as lower as possible, maintaining a high thermal conductivity and reducing the thermal resistance. Another important characteristic that a coating substrate should possess is to ensure a high renewal frequency of the droplets. The permanence of the droplets on the surface contributes to increase the total thermal resistance of heat transfer and, at the same time, to obstruct the mass transfer process. A fast departure of the droplets from the surface allows to have new fresh sites for nucleation. These considerations on the dehumidification process could be employed to the evaporator of a heat pump tumble dryer. The impact of coatings needs to be carefully addressed with respect to the peculiar boundary conditions typical of tumble dryers, namely extremely high absolute humidity at evaporator inlet. Currently, there are three main types of coating for fin surface available on the market. Each coating is classified according to the contact angle, as follows:

- Hydrophilic coating ($0° < \theta < 90°$);
- Hydrophobic coating ($90° < \theta < 150°$);
- Superhydrophobic coating ($150° < \theta < 180°$).

3.3.1 Hydrophilic coating

Hydrophilic coating allows to modify the surface contact angle to values below 90°. Considering a specific substrate where condensation occurs, for example an external fin, this type of coating leads to have a uniform and thin layer of liquid water on the fin. This film introduces an additional thermal resistance that can deteriorate the total heat transfer process. However, the gravity force helps to remove very quickly the condensate due to its weight and this could lead to an improvement of the drainage ability. The uniformity of this layer does not have negative influence on the air-side pressure drop. Fig. 3.9 shows an example of hydrophilic coating, applied to a finned coil.

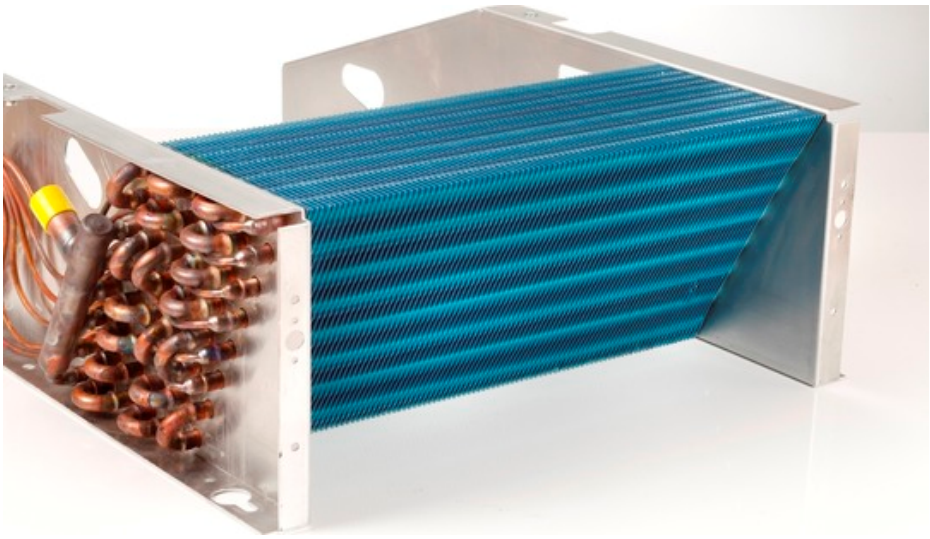

Fig. 3.9 Hydrophilic coating [3]

Studies related to the effects of hydrophilic coating in dehumidification conditions are quite limited in the open literature. Wang et al. [4] have investigated heat and mass transfer characteristics of plain fin-and-tube heat exchangers with and without hydrophilic coating. Tests with dehumidification were conducted with air inlet conditions of 27 °C and relative humidity from 50% and 85%; the inlet cold water temperature has been set to 7 °C. Experimental results have shown a negligible effect of the hydrophilic coating on the sensible heat transfer coefficients. The pressure drops are found about 15-40% lower than those without coating. In addition, the pressure drops for hydrophilic coated surfaces are sensitive to the inlet conditions, unlike the untreated ones that are not influenced by them. Liu and Jacobi [5] have studied the effect of surface hydrophilicity on the air-side performance and the retention and drainage behaviour of slit fin-and-tube heat exchangers. Tests with dehumidification were conducted with air inlet conditions of 23.9 °C of dry bulb temperature and 18.3 °C of dew point temperature; the inlet cold water temperature has been set to 4.4 °C. Experimental results have shown that hydrophilic coatings reduce the wet pressure drop significantly without decreasing the wet sensible heat transfer coefficient. Also, heat exchangers with high wettability retain much less water than hydrophobic ones in dehumidification conditions.

3.3.2 Hydrophobic coating

Hydrophobic coating allows to modify the surface contact angle to values between 90° and 150°. This coating is mainly used to solve corrosion issues, avoiding the contact between the condensate and the surface. The wettability of the surface is reduced and condensation occurs through the formation of single droplets. This type of condensation leads to an increment of the heat transfer area and, consequently, improves the total exchanged heat flux. However, in case of air dehumidification, the air-side pressure drop across the evaporator increases due to the presence of

droplets that originates irregularities on the surface. Fig. 3.10 shows an example of a hydrophobic coating applied to a finned coil. As can be seen from Fig. 3.10, differently from the previous type, the hydrophobic coating covers not only the fin surface, but also the tubes one.

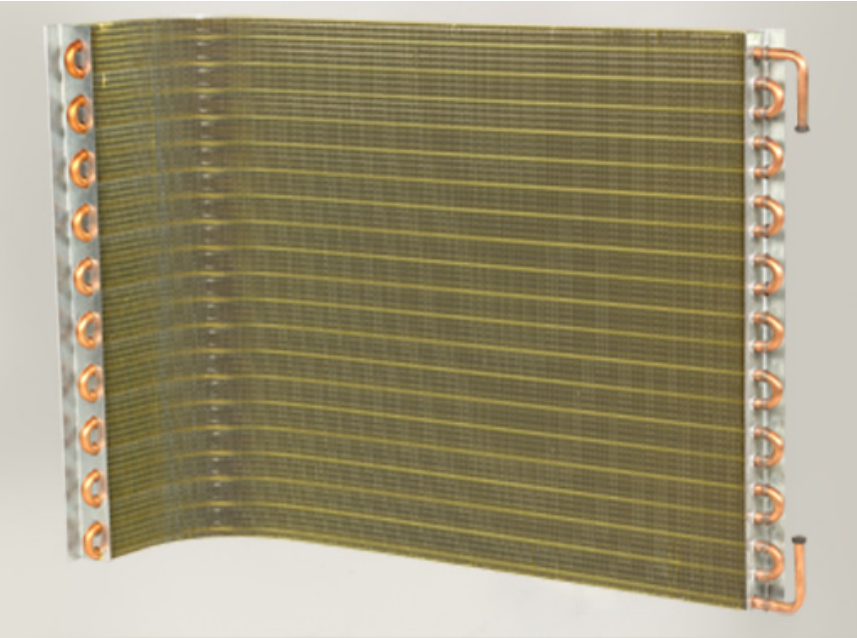

Fig. 3.10 Hydrophobic coating [6]

Also the studies related to the effects of hydrophobic coating in dehumidification conditions are limited in the open literature. Sir et al. [7] have investigated the effect of fin type and fin coating in dehumidification conditions in terms of condensation rate and efficiency. Tests with dehumidification were conducted with air inlet conditions of 38 °C of dry bulb temperature and relative humidity from 65% to 80%; the inlet cold water temperature has been set to 22 °C. Experimental results have shown that, for wavy fin evaporators, the hydrophobic coating has better performance compared to the hydrophilic one in terms of condensation rate and efficiency. For plain fin evaporators instead, the hydrophilic coating has better performance compared to the hydrophilic one in terms of condensation rate and efficiency.

3.3.3 Superhydrophobic coating

Superhydrophobic coating allows to modify the surface contact angle to values between 150° and 180°. This coating gives an extremely protection against corrosion and further reduced the contact angle between the droplet and fin surface. The reduction of the contact area with the substrate facilitates the probability of interaction between droplets, leading to the phenomenon of coalescence. When coalescence takes place, the resultant droplet occupies less substrate area than the sum of the previous occupied by the single droplets. but being more heavy than the single and it

is drained more easily. When this phenomenon occurs between droplets belonging to adjacent fins, there is the formation of a liquid bridge between them. This contact forms a local depression and adhesive forces tend to merge the droplets.

3.4 References

[1] Granozzi G. Richiami di nucleazione e crescita, lecture notes of "Fondamenti di nanoscienza", course at Università degli Studi di Padova.

[2] Chiwoong Choi, Moohwan Kim. Wettability effects on heat transfer. Two phase flow, phase change and numerical modelling, Dr. Amimul Ahsan (Ed. 2011), InTech.

[3] Retrieved from "https://www.beehivecoils.co.uk/products/coils/evaporators.html".

[4] Wang CC, Chang CT. Heat and mass transfer for plate fin-and-tube heat exchangers with and without hydrophilic coating, Int. J. of Heat and Mass Transfer 41(1998); 3109-3120.

[5] Liu L., M. Jacobi A. The effects of hydrophilicity on water drainage and condensate retention on air-conditioning evaporators, Int. Refr. and Air Cond. Conf. at Purdue, 2006.

[6] Retrieved from "http://www.spirotechindia.in/condensing-coils.aspx".

[7] Sir G., Balioglu O., Onbasioglu S.U. An experimental investigation into the effects of fin structure and surface type on the efficiency of heat exchangers used for dehumidification. Adv. Comp. Meth. and Experiments in Heat Transfer XIII, 2014; 123-131.

4 Fin surface characterization

4.1 Fin coatings selection

Evaporators in heat pump tumble dryers usually have aluminium fins without any coating. Applying one of the previous coatings to the bare aluminium surface, it is possible to obtain surfaces with different wettability. This surface modification also interests the condensation type that occurs during the dehumidification process. Surfaces with low contact angles usually presents a filmwise condensation and, according to Eq. 3.10, a higher rate of nucleation. Instead, the surface modification with hydrophobic or superhydrophobic coatings leads to dropwise condensation, due to the high value of the contact angle. Focusing on the analysis of the behaviour of different coatings under dehumidification conditions in HPTD evaporators, a commercial evaporator with bare aluminium fin surface has been treated with a hydrophilic coating and a hydrophobic one, both available on the market. The first part of the evaporator data sheet represents the geometry that is the same for the three samples, as shown in Fig. 4.1.

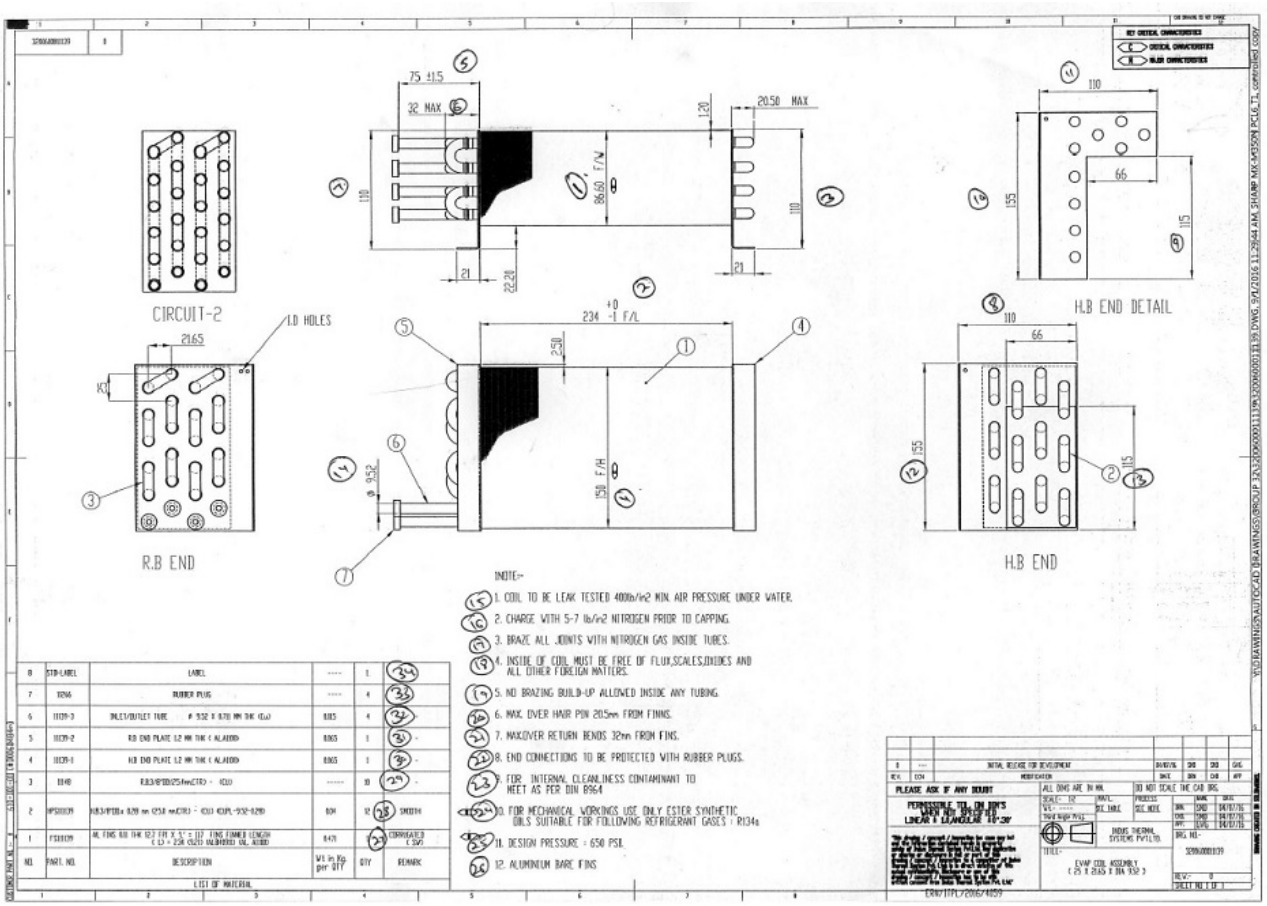

Fig. 4.1 Evaporator data sheet

The second part of the evaporator data sheet, represented in Fig. 4.2, Fig. 4.3 and Fig. 4.4 for each coating type, gives no additional information about its composition.

indus

INDUS INTERNATIONAL FZC, U.A.E

DIMENSIONAL RESULTS

Part Name : Evaporator Coil | Customer Name :ETX | Date : 03.09.2016

Indus Part no & Rev.:-3200600011139 Rev -0 | Sample Size : 4 Nos

Customer Part No. & Rev.: Z400180901 | Qty: 4 Nos

JOB NO -5072

Sr. No.	Dimension & Specification (mm)	Tool used for measurement	Measurement Results					Accepted	Not Accepted
			1	2	3	4	5		
1	F/W 86.60±1.0	Vernier Caliper	86.63	86.54	86.63	86.65		Accept	
2	F/L 234+0/-1	Vernier Caliper	233.65	233.42	233.36	233.45		Accept	
3	110±1.00	Vernier Caliper	110.12	110.41	110.23	110.25		Accept	
4	F/H 150±1.0	Vernier Caliper	150.32	150.42	150.48	150.24		Accept	
5	75 ±1.5	Vernier Caliper	75.32	75.42	75.36	75.54		Accept	
6	32 MAX	Vernier Caliper	28.56	28.54	28.56	28.42		Accept	
7	110±0.1	Vernier Caliper	110.42	110.26	110.21	110.14		Accept	
8	110±1.0	Vernier Caliper	110.32	110.2	110.2	110.12		Accept	
9	115 ±1	Vernier Caliper	115.32	115.42	115.23	115.53		Accept	
10	155 ±1	Vernier Caliper	155.23	155.01	155.12	155.32		Accept	
11	110±1.0	Vernier Caliper	110.12	110.32	110.42	110.23		Accept	
12	155 ±1.0	Vernier Caliper	155.32	155.42	155.26	155.28		Accept	
13	115±1.0	Vernier Caliper	115.25	115.36	115.25	115.24		Accept	
14	Ø 9.52±1.0	Vernier Caliper	9.53	9.52	9.54	9.53		Accept	
15	Coil to be leak tested 400lb/inzmin .air pressure under water	Testing	OK	OK	OK	OK		Accept	
16	Charge with 5-7 lb/in2 Nitrogen prior to capping	pressure guage	OK	OK	OK	OK		Accept	
17	Braze all joints with nitrogen gas inside tubes	Testing	OK	OK	OK	OK		Accept	
18	Inside of coil must be commercially free of flux,scales,oxides and all other foreign matters	Testing	OK	OK	OK	OK		Accept	
19	No brazing buildup allowed inside any tubing	Testing	OK	OK	OK	OK		Accept	
20	Max over hair pin - 20.5mm from fins	Vernier Caliper	18.58	19.05	19.12	18.82		Accept	
21	Max over return bend - 32 mm from fins	Vernier Caliper	26.38	26.35	26.42	26.45		Accept	
22	End Connection to be protected with rubber plugs	Visual	OK	OK	OK	OK		Accept	
23	For internal cleanliness contaminant to be meet as per DIN 8964	Visual	OK	OK	OK	OK		Accept	
24	For mechanical working use only ester synthetic oils suitable for following refrigerant	Testing	OK	OK	OK	OK		Accept	
25	Design pressure ;650 psi	Testing	OK	OK	OK	OK		Accept	
26	Alluminium bare fins	Visual	OK	OK	OK	OK		Accept	
27	Fin 0.11 thk x 12.7 FPI Al corrugated	Micrometer	0.11 x 12.7 FPI Al corrugated	0.11 x 12.7 FPI Al corrugated	0.11 x 12.7 FPI Al corrugated	0.11 x 12.7 FPI Al corrugated		Accept	
28	H.B 9.52 OD X 0.28 (Cu)	Vernier Caliper/ ponit micrometer	9.52 OD X 0.28 (Cu)	9.52 OD X 0.28 (Cu)	9.52 OD X 0.28 (Cu)	9.52 OD X 0.28 (Cu)		Accept	
29	R.B OD -9.52 (Cu)plain	Vernier Caliper	9.52(Cu plain)	9.52(Cu plain)	9.52(Cu plain)	9.52(Cu plain)		Accept	
30	H.B End plate 1.2 Thk (Al)	Micrometer	1.2(Al)	1.2(Al)	1.2(Al)	1.2(Al)		Accept	
31	R.B End plate 1.2 Thk (Al)	Micrometer	1.2(Al)	1.2(Al)	1.2(Al)	1.2(Al)		Accept	
32	Inlet /outlet tube Dia Ø 9.52 x0.71 Thk (Cu)	Vernier Caliper/point micrometer	9.52x0.71 Cu	9.52x0.71 Cu	9.52x0.71 Cu	9.52x0.71 Cu		Accept	
33	Rubber plug	Vernier Caliper/ micrometer	ok	ok	ok	ok		Accept	
34	label	Vernier Caliper/ micrometer	ok	ok	ok	ok		Accept	

Fig. 4.2 Bare Al evaporator data sheet

indus

INDUS INTERNATIONAL FZC, U.A.E

DIMENSIONAL RESULTS

Part Name : Evaporator Coil | Customer Name :ETX | Date : 03.09.2016

Indus Part no & Rev.:-3200600011140 Rev -0 | Sample Size : 4 Nos

Customer Part No. & Rev.: Z408180602 | Qty: 4 Nos

JOB NO -5074

Sr. No.	Dimension & Specification (mm)	Tool used for measurement	Measurement Results					Accepted	Not Accepted
			1	2	3	4	5		
1	F/W 86.60±1.0	Vernier Caliper	86.63	86.72	86.77	86.57		Accept	
2	F/L 234+0/-1	Vernier Caliper	233.96	233.95	233.97	233.93		Accept	
3	110±1.00	Vernier Caliper	110.12	110.32	110.25	110.26		Accept	
4	F/H 150±1.0	Vernier Caliper	150.12	150.32	150.21	150.2		Accept	
5	75 ±1.5	Vernier Caliper	75.08	75.06	75.03	75.09		Accept	
6	32 MAX	Vernier Caliper	26.32	26.5	26.3	26.45		Accept	
7	110±0.1	Vernier Caliper	110.42	110.23	110.24	110.39		Accept	
8	110±1.0	Vernier Caliper	110.12	110.23	110.32	110.42		Accept	
9	115 ±1	Vernier Caliper	115.32	115.42	115.52	115.63		Accept	
10	155 ±1	Vernier Caliper	155.08	155.36	155.42	155.24		Accept	
11	110±1.0	Vernier Caliper	110.42	110.23	110.24	110.15		Accept	
12	155 ±1.0	Vernier Caliper	155.32	155.12	155.03	155.04		Accept	
13	115±1.0	Vernier Caliper	115.32	115.36	115.42	115.26		Accept	
14	Ø 9.52±1.0	Vernier Caliper	9.56	9.52	9.54	9.53		Accept	
15	Coil to be leak tested 400lb/in2min .air pressure under water	Testing	OK	OK	OK	OK		Accept	
16	Charge with 5-7 lb/in2 Nitrogen prior to capping	pressure guage	OK	OK	OK	OK		Accept	
17	Braze all joints with nitrogen gas inside tubes	Testing	OK	OK	OK	OK		Accept	
18	Inside of coil must be commercially free of flux,scales,oxides and all other foreign matters	Testing	OK	OK	OK	OK		Accept	
19	No brazing buildup allowed inside any tubing	Testing	OK	OK	OK	OK		Accept	
20	Max over hair pin - 20.5mm from fins	Vernier Caliper	18.59	19.05	19.12	18.82		Accept	
21	Max over return bend - 32 mm from fins	Vernier Caliper	26.38	26.35	26.42	26.45		Accept	
22	End Connection to be protected with rubber plugs	Visual	OK	OK	OK	OK		Accept	
23	For internal cleanliness contaminant to be meet as per DIN 8964	Visual	OK	OK	OK	OK		Accept	
24	For mechanical working use only ester synthetic oils suitable for following refrigerant	Testing	OK	OK	OK	OK		Accept	
25	Design pressure ;650 psi	Testing	OK	OK	OK	OK		Accept	
26	Blue hydrophilic- coated	Visual	OK	OK	OK	OK		Accept	
27	Fin 0.11 thk x 12.7 FPI Al corrugated	Micrometer	0.11 x 12.7 FPI Al corrugated	0.11 x 12.7 FPI Al corrugated	0.11 x 12.7 FPI Al corrugated	0.11 x 12.7 FPI Al corrugated		Accept	
28	H.B 9.52 OD X 0.28 (Cu)	Vernier Caliper/ ponit micrometer	9.52 OD X 0.28 (Cu)	9.52 OD X 0.28 (Cu)	9.52 OD X 0.28 (Cu)	9.52 OD X 0.28 (Cu)		Accept	
29	R.B OD -9.52 (Cu)plain	Vernier Caliper	9.52(Cu plain)	9.52(Cu plain)	9.52(Cu plain)	9.52(Cu plain)		Accept	
30	H.B End plate 1.2 Thk (Al)	Micrometer	1.2(Al)	1.2(Al)	1.2(Al)	1.2(Al)		Accept	
31	R.B End plate 1.2 Thk (Al)	Micrometer	1.2(Al)	1.2(Al)	1.2(Al)	1.2(Al)		Accept	
32	Inlet /outlet tube Dia Ø 9.52 x0.71 Thk (Cu)	Vernier Caliper/point micrometer	9.52x0.71 Cu	9.52x0.71 Cu	9.52x0.71 Cu	9.52x0.71 Cu		Accept	
33	Rubber plug	Vernier Caliper/ micrometer	ok	ok	ok	ok		Accept	
34	label	Vernier Caliper/ micrometer	ok	ok	ok	ok		Accept	

Fig. 4.3 Hydrophilic Al evaporator data sheet

indus

INDUS INTERNATIONAL FZC, U.A.E

DIMENSIONAL RESULTS

Part Name : Evaporator Coil | Customer Name :ETX | Date : 03.09.2015

Indus Part no & Rev.:-3200600011141Rev -0 | Sample Size : 4 Nos

Customer Part No. & Rev.: Z408180603 | Qty: 4 Nos

JOB NO -5073

Sr. No.	Dimension & Specification (mm)	Tool used for measurement	Measurement Results					Accepted	Not Accepted
			1	2	3	4	5		
1	F/W 86.60±1.0	Vernier Caliper	86.36	86.45	76.52	86.37		Accept	
2	F/L 234+0/-1	Vernier Caliper	233.45	233.69	233.59	233.95		Accept	
3	110±1.00	Vernier Caliper	110.12	110.42	110.36	110.25		Accept	
4	F/H 150±1.0	Vernier Caliper	150.42	150.36	150.24	150.25		Accept	
5	75 ±1.5	Vernier Caliper	75.312	75.36	75.52	75.54		Accept	
6	32 MAX	Vernier Caliper	26.36	26.54	26.36	26.65		Accept	
7	110±0.1	Vernier Caliper	110.42	110.26	110.32	110.42		Accept	
8	110±1.0	Vernier Caliper	110.25	110.14	110.23	110.25		Accept	
9	115 ±1	Vernier Caliper	115.23	115.24	115.58	115.56		Accept	
10	155 ±1	Vernier Caliper	155.36	155.24	155.29	155.25		Accept	
11	110±1.0	Vernier Caliper	110.32	100.25	110.12	110.36		Accept	
12	155 ±1.0	Vernier Caliper	155.32	155.36	155.412	155.24		Accept	
13	115±1.0	Vernier Caliper	115.36	155.24	155.71	155.36		Accept	
14	Ø 9.52±1.0	Vernier Caliper	9.53	9.52	9.54	9.56		Accept	
15	Coil to be leak tested 400lb/in2min .air pressure under water	Testing	OK	OK	OK	OK		Accept	
16	Charge with 5-7 lb/in2 Nitrogen prior to capping	pressure guage	OK	OK	OK	OK		Accept	
17	Braze all joints with nitrogen gas inside tubes	Testing	OK	OK	OK	OK		Accept	
18	Inside of coil must be commercially free of flux,scales,oxides and all other foreign matters	Testing	OK	OK	OK	OK		Accept	
19	No brazing buildup allowed inside any tubing	Testing	OK	OK	OK	OK		Accept	
20	Max over hair pin - 20.5mm from fins	Vernier Caliper	18.36	18.24	19.12	18.82		Accept	
21	Max over return bend - 32 mm from fins	Vernier Caliper	26.38	26.35	26.42	26.45		Accept	
22	End Connection to be protected with rubber plugs	Visual	OK	OK	OK	OK		Accept	
23	For internal cleanliness contaminant to be meet as per DIN 8964	Visual	OK	OK	OK	OK		Accept	
24	For mechanical working use only ester synthetic oils suitable for following refrigerant	Testing	OK	OK	OK	OK		Accept	
25	Design pressure :650 psi	Testing	OK	OK	OK	OK		Accept	
26	I -COAT GREEN	Visual	OK	OK	OK	OK		Accept	
27	Fin 0.11 thk x 12.7 FPI Al corrugated	Micrometer	0.11 x 12.7 FPI Al corrugated	0.11 x 12.7 FPI Al corrugated	0.11 x 12.7 FPI Al corrugated	0.11 x 12.7 FPI Al corrugated		Accept	
28	H.B 9.52 OD X 0.28 (Cu)	Vernier Caliper/ ponit micrometer	9.52 OD X 0.28 (Cu)	9.52 OD X 0.28 (Cu)	9.52 OD X 0.28 (Cu)	9.52 OD X 0.28 (Cu)		Accept	
29	R.B OD -9.52 (Cu)plain	Vernier Caliper	9.52(Cu plain)	9.52(Cu plain)	9.52(Cu plain)	9.52(Cu plain)		Accept	
30	H.B End plate 1.2 Thk (Al)	Micrometer	1.2(Al)	1.2(Al)	1.2(Al)	1.2(Al)		Accept	
31	R.B End plate 1.2 Thk (Al)	Micrometer	1.2(Al)	1.2(Al)	1.2(Al)	1.2(Al)		Accept	
32	Inlet /outlet tube Dia Ø 9.52 x0.71 Thk (Cu)	Vernier Caliper/point micrometer	9.52x0.71 Cu	9.52x0.71 Cu	9.52x0.71 Cu	9.52x0.71 Cu		Accept	
33	Rubber plug	Vernier Caliper/ micrometer	ok	ok	ok	ok		Accept	
34	label	Vernier Caliper/ micrometer	ok	ok	ok	ok		Accept	

Fig. 4.4 Hydrophobic Al evaporator data sheet

4.2 SEM analysis

In order to understand the composition of the three samples fin surface, a SEM analysis has been carried out at the Institute of Condensed Matter Chemistry and Technologies for Energy (ICMATE) of the National Research Council Laboratories in Padova. At first, a sample of the bare aluminium

fin surface has been analyzed, as shown in Fig. 4.5. After, a sample of the hydrophilic aluminium fin surface has been observed, as shown in Fig. 4.6.

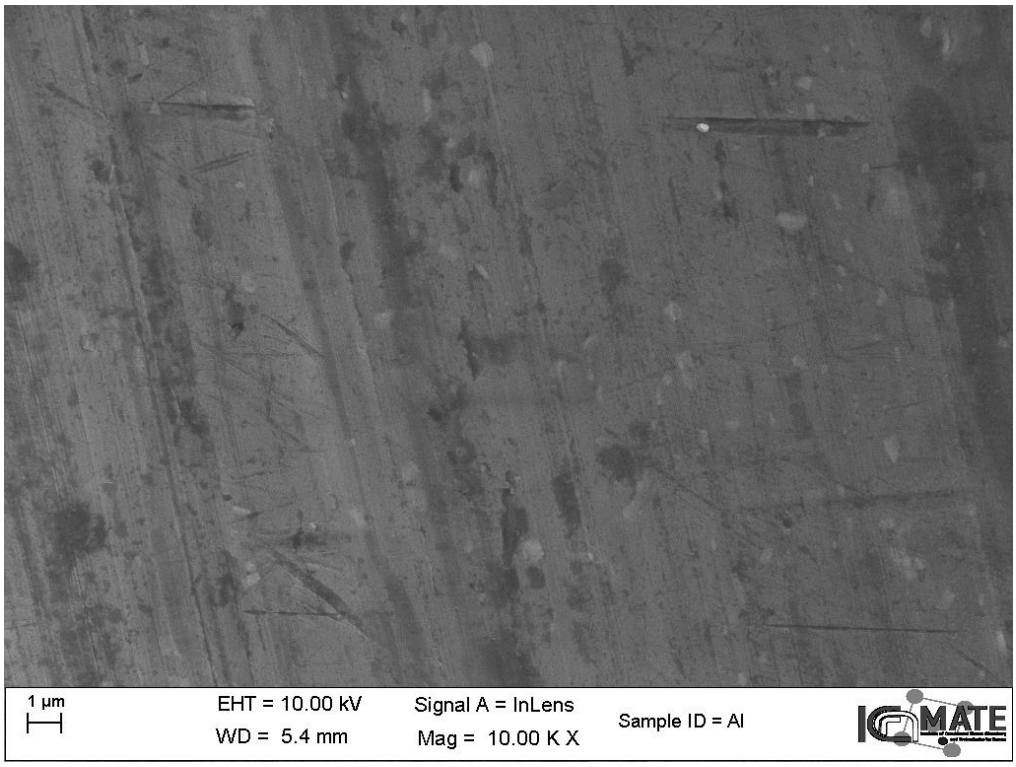

Fig. 4.5 Bare Al SEM analysis

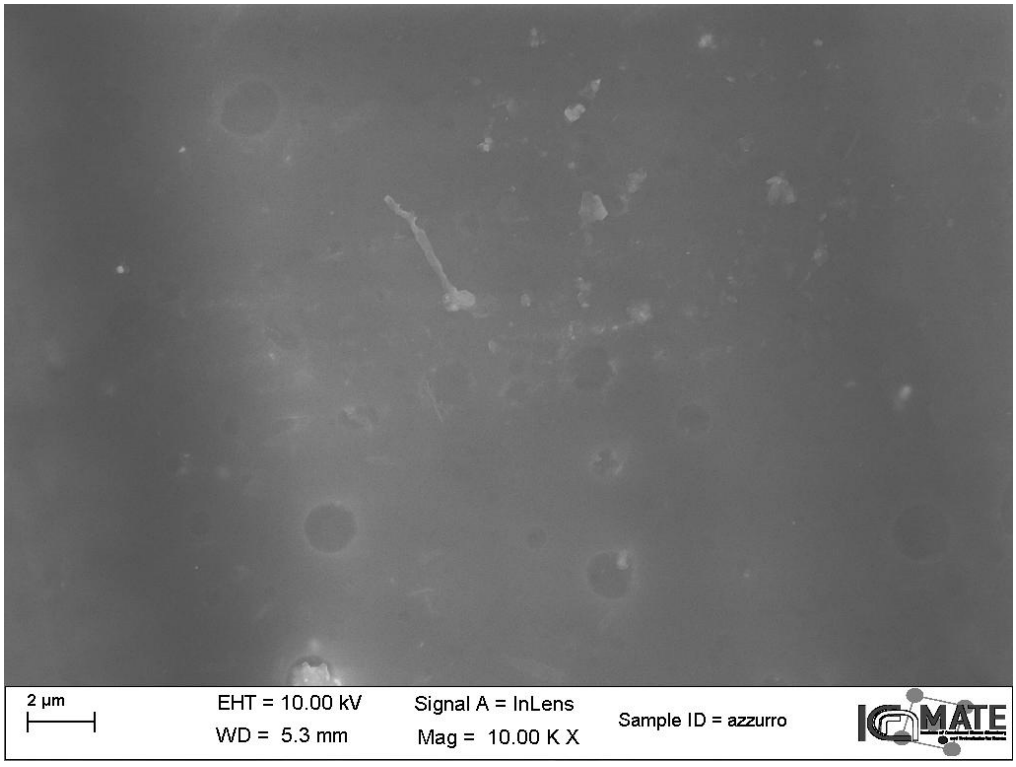

Fig. 4.6 Hydrophilic Al SEM analysis

From the two previous observations, no information can be deduced about the composition of the coatings. For the hydrophobic sample, the SEM analysis has not been employed due to the low conductivity of the coating. Because of the lack of results in this investigation, another procedure for surface characterization has been employed. In order to understand the surface wettability of the three coatings, a contact angle measurement procedure has been carried out.

4.3 Contact angle measurement: experimental apparatus

The experimental apparatus for the contact angle measurement is located at the Institute of Condensed Matter Chemistry and Technologies for Energy (ICMATE) of the National Research Council Laboratories in Padova. This equipment allows making tests for the static and dynamic measurement of contact angle. The sessile drop is located on the sample surface that lies on a horizontal plane. Cycles of accretion and reduction of drop size take place to simulate the motion of the drop on an inclined plane in order to measure the dynamic contact angles. These procedures are realized through the use of a microsyringe that alternately injects and sucks a part of the liquid drop, as shown in Fig. 4.7.

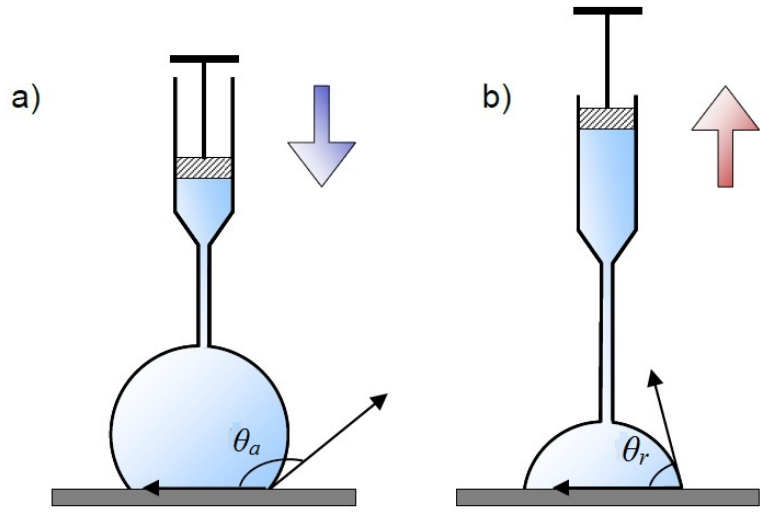

Fig. 4.7 Usage of microsyringe for dynamic contact angle measurement (a: injection, b: suction)

The apparatus hardware is composed of the following elements:

- Computer;
- Video camera for images acquisition;
- Programmable motorized syringe with multi-valve;
- Diffusive illumination system;
- Sample holder;

- System for the needle correct placement.

In Fig. 4.8, a lateral view of the experimental apparatus is showed.

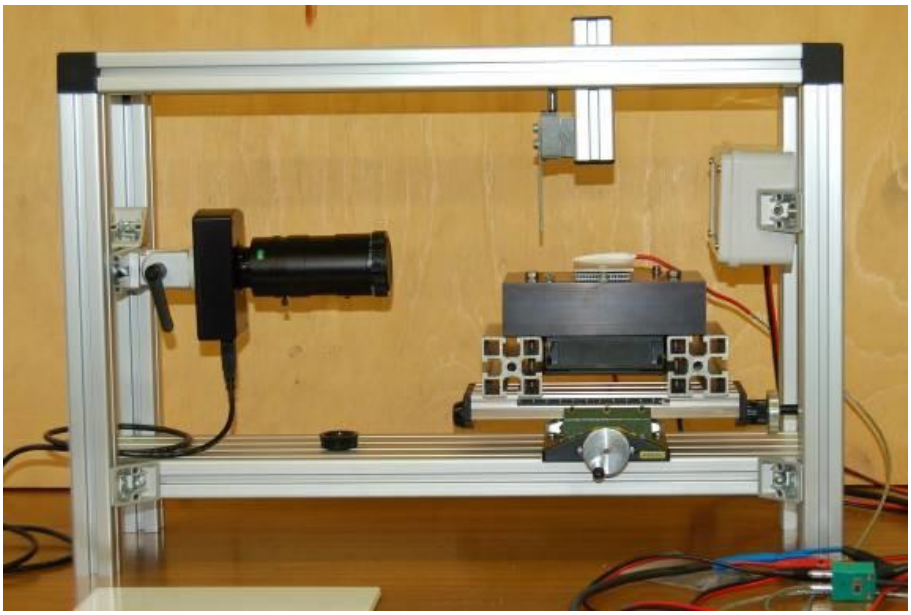

Fig. 4.8 Experimental apparatus

The micropump is equipped with a step by step driver for an overall number of 48000 steps (Kloehn, V6C model). A set of interchangeable syringes is used with volumes between 0.1 ml and 10 ml. The syringe is connected to a three ways rotary valve, integrated with the pump and commanded through software. The video camera for images acquisition (LU-205B model) has a resolution of 1600x1200 pixel, a MLH-10X lens and an USB 2.0 interface, that also allows PC configuration. Two Labview programs are used for the measure of the static and dynamic contact angles. The first one allows to acquiring the recording of the droplet placed onto the analyzed surface. The second one employs the post processing of the previous recording. Through an analysis frame by frame, the resultant contact angles are obtained. In Fig. 4.9, the procedure flowchart of the two programs is represented.

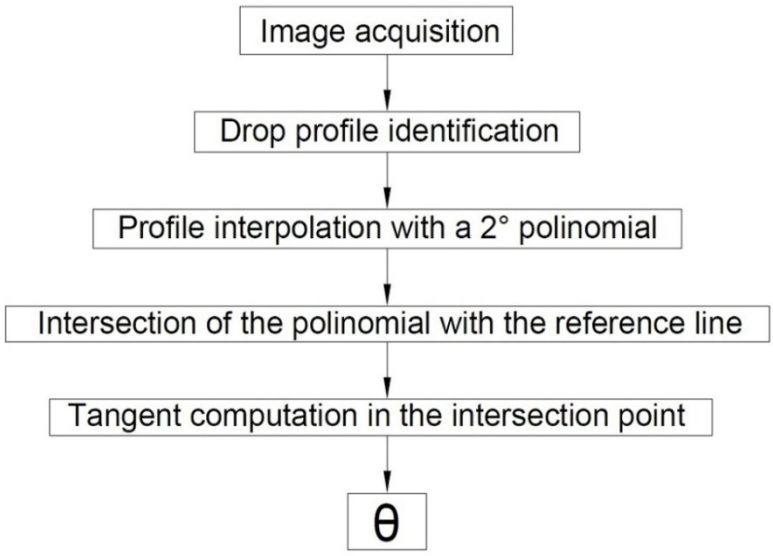

Fig. 4.9 Software flowchart for the contact angle computation

4.4 Procedure for the dynamic contact angles measurement

In real solid surfaces, the static contact angle is not equal to the thermodynamic equilibrium angle, but it is included between two values, previously identified as θ_a and θ_r. From these two values, it is possible to evaluate the contact angle hysteresis. Before positioning the first droplet onto the surface, several steps are mandatory. At first, some cleaning cycles of the liquid distribution system are employed; then, the system is filled of liquid. The selected surface for the test is located onto the sample holder. The horizontality of the surface is checked and the distance between the surface and the syringe needle is adjusted. At last, all the apparatus is obscured with screens for guaranteeing a better quality of the image. After positioning the droplet on the surface, the sample location is regulated in order to align the needle with the drop centre. This procedure allows to an axial symmetric droplet growth, reducing the influence of the needle on the droplet profile. As explained previously, the simulation of the droplet motion on an inclined plane for the dynamic measure of the contact angles is realized through a cyclic procedure. The droplet volume increases and decreases cyclically though the injection and the suction of a part of liquid. Every cycle can be divided in four steps:

- Injection of a fixed amount of liquid in the droplet (initial volume known);
- Waiting (optional);
- Suction of liquid until the initial volume is reached;
- Second phase of waiting (optional).

The injection of liquid has to be regulated in order to reach a constant value of the advancing contact angle. The waiting steps are introduced to allow a regular growth of the droplet, avoiding eventual overpressure. The choice of a cycling procedure is due also to another feature that is

present during the tests. After the first cycle, a decrease in the values of the dynamic angles has been observed. Thus, the cycling procedure aims to understand the surface wettability after the interaction with the liquid.

4.4.1 Image acquisition and analysis

The first Labview program allows to acquire and save the recording, specifying the path, the video type, the refresh rate and the image quality. In this step, a perfect horizontality of the plane has to be assure. During a cycle, the recording is saved in negative black and white. An example of correct acquisition is showed in Fig. 4.10.

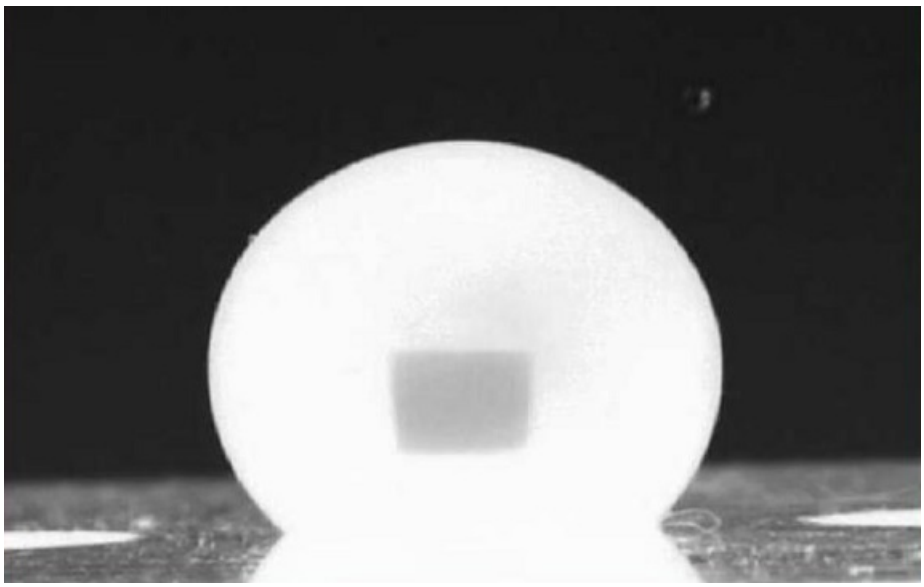

Fig. 4.10 Example of recording

The second program analyzes the previous recording. The region of interest for the study is selected drawing a rectangle that has the low side just over the solid-liquid contact point. This last feature is useful when the recording has unclear images. The base line, instead, is located in correspondence with the contact point.

4.5 Coating fin samples

Three different types of fin surfaces are analyzed in order to characterize their wetting behaviour. All of the fins are made of aluminium, treated with different coatings realized by Indus International (FZC). In Fig. 4.11, Fig. 4.12 and Fig. 4.13, the three types of fin surface coatings are shown.

Fig. 4.11 Bare aluminium fin surface coating

Fig. 4.12 Hydrophilic fin surface coating

Fig. 4.13 Hydrophobic fin surface coating

In Fig. 4.11, the fin surface is made of bare aluminium, without any coating. Fig. 4.12, instead, represents the aluminium fin surface treated with a hydrophilic coating, characterized by a blue colour. The last picture, Fig. 4.13, shows the usage of a hydrophobic coating on the fin surface, marked in green. A rectangular sample of each kind of surface has been considered for the experimental measurement, having a thickness of 0.11 mm.

4.6 Experimental measurement of static and dynamic contact angles

4.6.1 Bare aluminium sample

The first tests were made on a rectangular bare aluminium fin sample. Initially, the static contact angle was evaluated in a certain location, positioning droplets of different sizes. Then, a couple of dynamic tests were performed. Next, the same procedure was repeated in a different location on the sample. Table 4.1 and Table 4.2 resume, respectively, static and dynamic tests for the two zones.

Table 4.1

Static tests on bare aluminium sample

	# Test	Droplet volume [µl]
1° Location	1	8,3
	2	8,3
	3	8,3
	4	12,5
	5	12,5
	6	16,7
	7	16,7
2° Location	10	8,3
	11	8,3
	12	12,5
	13	12,5
	14	16,7
	15	16,7

Table 4.2

Dynamic tests on bare aluminium sample

	# Test	Initial droplet volume [µl]	ΔV [µl/step]	Final droplet volume [µl]
1° Location	8	8,3	0,42	20,8
	9	8,3	0,42	20,8
2° Location	16	8,3	0,42	20,8
	17	8,3	0,42	20,8

4.6.2 Hydrophobic aluminium sample

After the tests on bare aluminium, a sample of hydrophobic aluminium was considered for the study. The same procedure employed previously was applied in the analysis of static and dynamic contact angles of this sample. Table 4.3 and Table 4.4 show the different tests performed in three locations. In the third location, three cycles of accretion and reduction were performed for each of the two tests in order to measure the advancing and the receding contact angles.

Table 4.3

Static tests on hydrophobic aluminium sample

	#Test	Droplet volume [µl]
1° Location	1	8,3
	2	8,3
	3	8,3
	4	8,3
	5	12,5
	6	12,5
	7	16,7
	8	16,7
	9	16,7

Table 4.4

Dynamic tests on hydrophobic aluminium sample

2° Location	# Test	Initial droplet volume [µl]	ΔV [µl/step]	Final droplet volume [µl]	Volume reduction [µl]
	10	8,3	0,42	29,2	\
3° Location (cycle)	11	12,5	0,21	33,3	16,7
	12	12,5	0,21	33,3	16,7

4.6.3 Hydrophilic aluminium sample

At last, a hydrophilic aluminium sample was analyzed for static and dynamic contact angles measurement. However, the experimental procedure cannot be applied in this case because the software doesn't recognize the drop profile. This fact is due to the high hydrophilicity of the surface that warps the spherical shape. For this reason, only an indirect measure of the static contact angle is possible. This measure was performed at first through an image acquisition of a sessile drop on the substrate. Then, the image was analyzed with a CAD software to determine geometrically the static contact angle.

4.7 Experimental results

For each static and dynamic test, the right and the left contact angles of the single droplet are established through an average of the instantaneous values. Then, the mean of these two values has been considered as the contact angle of the single test.

4.7.1 Bare aluminium

In Table 4.5, the values of the static contact angle for the bare aluminium sample are represented. As can been seen, the resulting static contact angle is equal to 76° ±1°. Then, Table 4.6 shows the dynamic contact angles for each tests that bring to an average value is 77° ±1°.

Table 4.5

Static contact angles of bare aluminium sample

#Test	1	2	3	4	5	6	7	10	11	12	13	14	15
Angle [°]	75	76	74	79	78	73	77	79	78	73	71	81	77

Table 4.6

Dynamic contact angles of bare aluminium sample

#Test	Angle [°]
8	74
9	70
16	83
17	82

From the two values , the bare aluminium sample has an advancing contact angle of 77° ±1° that highlights a hydrophilic behavior.

4.7.2 Hydrophobic aluminium

The static experimental measures of the hydrophobic aluminium sample are represented in Table 4.7. The static contact angle has a mean value of 97° ±1°. After, the average values of the dynamic tests are shown in Table 4.8. As can be seen from Table 4.8, the advancing contact angle of the sample has a mean value of 113° ±1° and the receding one is equal to 108°±1°. The value of the advancing contact angle confirms the hydrophobic behaviour of the surface that also shows a low hysteresis.

Table 4.7

Static contact angle of hydrophobic aluminium sample

#Test	Angle [°]
1	105
2	98
3	98
4	101
5	100
6	93
7	90
8	90
9	95

Table 4.8

Dynamic contact angles of hydrophobic aluminium sample

#Test	Advancing angle [°]	Receding angle [°]
8	110	\
9	115	107
10	114	109

4.7.3 Hydrophilic aluminium

The static contact angle of the hydrophilic aluminium sample has been determined through a geometrical procedure. From the analysis of the screenshot represented in Fig. 4.14, the static contact angle of the hydrophilic sample has been found equal to 7° ±1°. This value confirms the high hydrophilic behaviour of the surface.

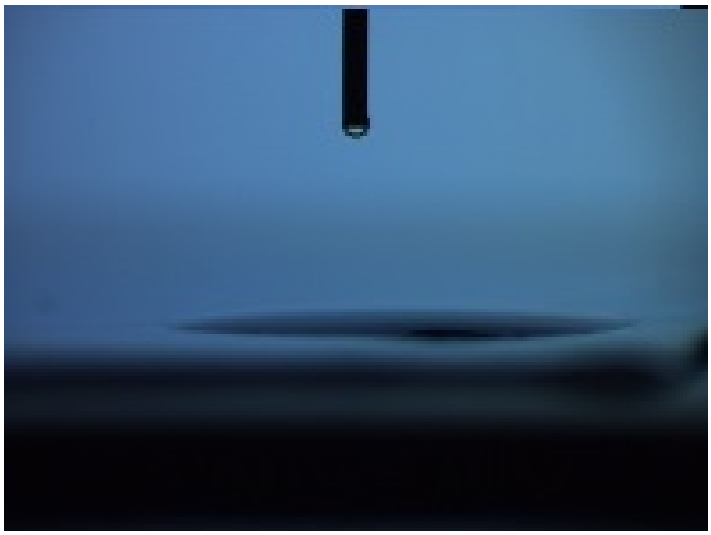

Fig. 4.14 Hydrophilic sample screenshot

4.8 Conclusions

An experimental analysis of the surface wettability of three different fin coating samples has been carried out at the Institute of Condensed Matter Chemistry and Technologies for Energy (ICMATE) of the National Research Council Laboratories in Padova. The static and dynamic contact angles have been measured for the untreated and hydrophobic samples. No dynamic measures has been executed for the third sample due to its high hydrophilicity. The static contact angles have been found equal to 7°, 76° and 97° respectively for the hydrophilic, untreated and hydrophobic samples. The advancing contact angle for the bare aluminium sample has been found equal to 77°. For the hydrophobic sample, the advancing contact angle has been measured equal to 113°.

5 Wind tunnel

5.1 Wind tunnel overview

The testing activity of full/model-scale components that deals with the study of a physical process involving air could be carry out in a wind tunnel system [1]. This equipment allows to achieve repeatable and controlled air conditions for experimental investigations. There are two main different configurations of wind tunnel according the principal duct system: open cycle or closed-loop cycle. In the open cycle configuration, air is taken from the outside and it is conditioned for reaching the desired values of temperature, humidity and velocity. Then, the humid air passes through the test section where dehumidification takes place and, at last, it returns to the ambient. Unlike this configuration, in a closed-loop cycle the air flows continuously in the wind tunnel, without any release to the outside. Another difference between the two configuration types is related to the cost. In general, the open configuration has less fabrication costs than the closed-loop, but it requires more operating costs for maintaining the same working conditions. A typical configuration of these two types is represented in Fig. 5.1.

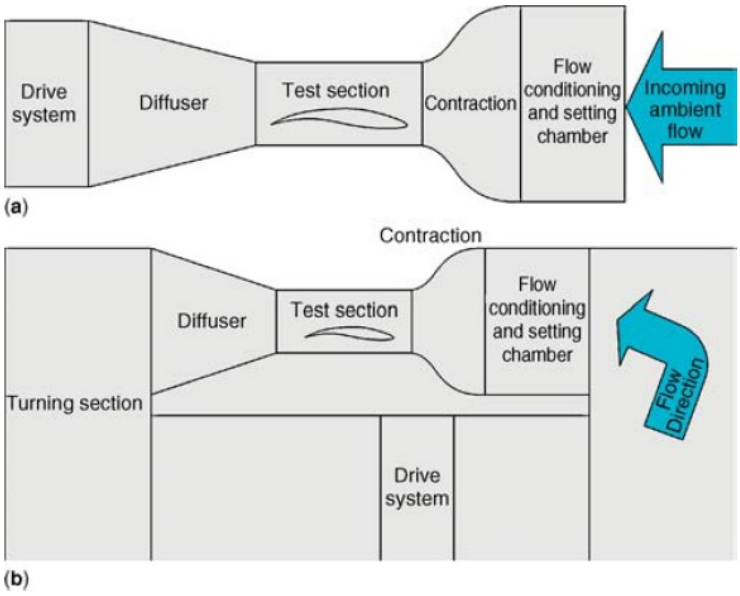

Fig. 5.1 Wind tunnel configuration: open (a) closed-loop (b) [1]

As can be seen from Fig. 5.1, each of the two configurations present the same sequence of the following elements:

- flow conditioning and settling chamber;
- contraction;
- test section;

- diffuser;
- drive system.

All of these components are designed in order to meet specific requirements that are mainly related to the wind tunnel working conditions, the overall equipment cost and space restrictions.

5.1.1 Flow conditioning and settling chamber

In wind tunnels, flow conditioning is necessary in order to reach and achieve the air desired working conditions at the test section inlet. Air temperature and velocity profiles must be as much as possible uniform all over the channel cross section area. These uniform conditions are mainly achieved in the settling chamber, that usually includes a honeycomb, one or more screens and a settling duct. The settling chamber plays a key role in the overall wind tunnel design for assuring repeatable and controlled conditions. Honeycomb elements are mainly used for aligning the flow along axis the tunnel axis, removing swirl and lateral velocity variation. The swirl angle of the incoming flow should be less than 10° for avoiding the stalling of the honeycomb cells, that could bring to an increase of the pressure drop across the component and a non-uniform flow. A honeycomb can be chosen according to its length and its cells size. Cells could have different cross section shape, such as circular, square or hexagonal. The most used type is the hexagonal one, as shown in Fig. 5.2, because it presents the lowest pressure drop coefficient.

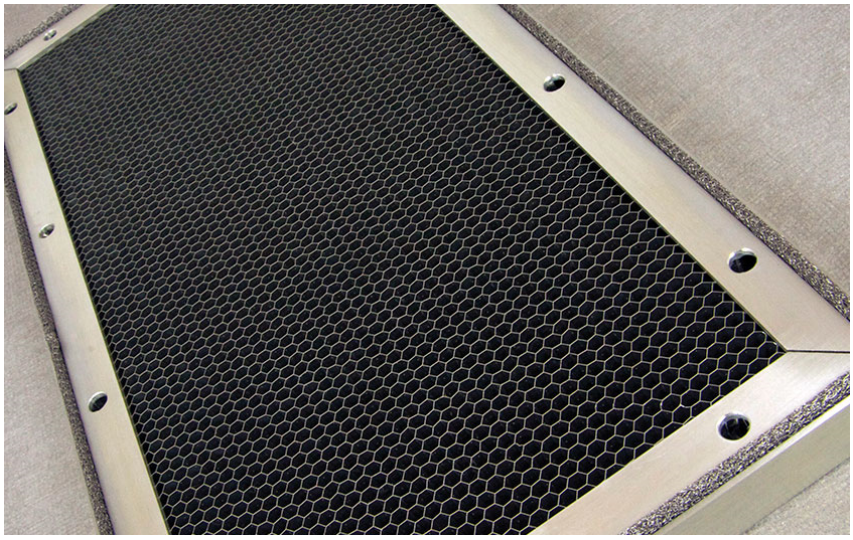

Fig. 5.2 Aluminium honeycomb

Screens are inserted in order to reduce the turbulence levels breaking up large eddies into smaller ones that decay faster. They also promote the flow uniformity by imposing a static drop pressure, which is proportional to velocity squared. In order to reduce drastically the turbulence of the flow, two or more screens can be inserted in series. Screens also provided to the uniformity of the air

temperature and humidity all over the cross section area of the duct. They can be inserted before and after the air flow conditioning elements, like heaters or steam injector systems. Just like honeycombs, screens are characterized by some geometrical parameters: the hole size, the pitch between adjacent holes and the open area, defined as a percentage of the overall screen area. A screen representation is shown in Fig. 5.3.

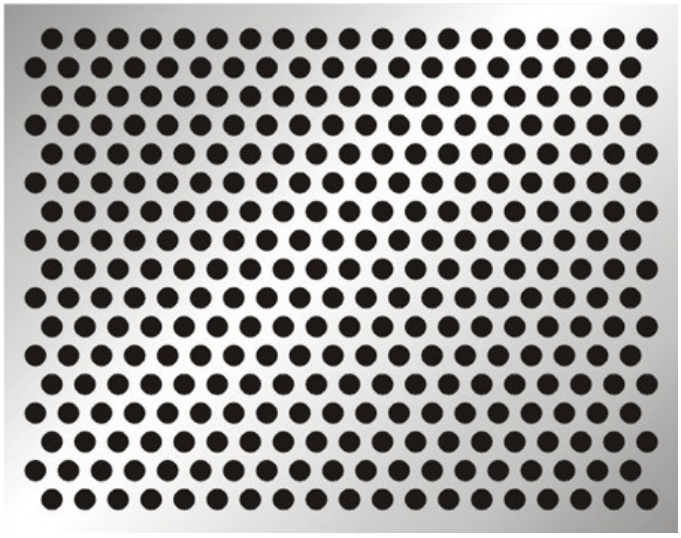

Fig. 5.3 Perforated plate

5.1.2 Contraction

The contraction area is fundamental in order to ensure an uniform flow at the inlet of the test section. This component accelerates and aligns the flow, stretching vortex filament. The shape of the contraction must be properly designed, taking into account costs, geometrical constrains and the desired quality level of the wind tunnel.

5.1.3 Test section

The test section is the principal component of the wind tunnel and it determines the size of the total experimental apparatus. This part contains the analysis sample, which is crossed by the accelerated air flow exiting from the contraction. The majority of measurement instrumentations is located in this section. Design should also account for accessibility issues.

5.1.4 Diffuser

The diffuser decelerates the high-speed flow from the test section in order to achieve static pressure recovery and reducing the load of the drive system. As for the contraction element, the diffuser must be designed according to physical constrains of the apparatus.

5.1.5 Drive system

The drive system generates a volume flow and compensates for the total pressure losses in the apparatus. This element can be a fan or a blower. Fans are classified according to the volume flow rate and the static pressure they can overcome. Fan performance is represented by fan load curves that indicate the pressure loss as a function of the flow rate for different efficiency. The pressure loss estimation in the wind tunnel leads to the knowing of the resistance curve, represented as a function of the flow rate. The points where the fan curves intersect the estimation resistance curve determinate the operating points of the wind tunnel. In order to guarantee stable working conditions, the fan curve or the resistance curve must be adjustable. The drive system choice must also take into account the working noise level.

5.2 Wind tunnel design

The first step of the wind tunnel design deals with the choice of the circuit configuration, open or closed-loop. In the open configuration, air is continually conditioned to the desired working point. Starting from still ambient air, thermal and mechanical powers provides to reach test section inlet conditions, as shown in Eq. 5.1:

$$Q_s + Q_{lat} + P_{fan} = \dot{m}_a \cdot (h_{a,in} - h_{a,amb}) + \dot{m}_a \cdot \frac{w_{a,in}^2}{2} \tag{5.1}$$

In Eq. 5.1, the left side involves sensible and latent thermal powers, related to the temperature and humidity increases and the mechanical power of the fin for reaching the desired inlet velocity. In heat pump tumble dryers, the warm humid air at the evaporator inlet has, respectively, temperature and relative humidity values of 40°C and 90%, on average during the working cycle. In case of an open cycle, the ambient air has to be conditioned for reaching the previous values at the evaporator inlet. A temperature of 20°C and a relative humidity of 50% can be assumed as reference values for the ambient. The increase of the absolute humidity between the two states varies approximately from 7.5 g_v/kg_a to 50 g_v/kg_a. So, the steam flow rate that must be supplied is estimated from Eq. 5.2 and Eq. 5.3:

$$\dot{m}_a \cdot (h_{a,in} - h_{a,amb}) = \dot{m}_a \cdot c_{p.a} \cdot (t_{a,in} - t_{a,amb}) + \dot{m}_a \cdot (x_{a,in} - x_{amb}) \cdot r \tag{5.2}$$

$$\dot{m}_v = \dot{m}_a \cdot (x_{a,in} - x_{amb}) \tag{5.3}$$

where the two indexes are related to the previous states. Considering a volumetric air flow of 300 m^3/h, a typical value for the HPTD application, the necessary steam flow rate is estimated of about 36 kg/h. For producing and injecting this steam mass flow, a vapour generator with about 15 kW

must be installed. Additionally, air sensible heating will require about 2 kW and the drive system power will be estimated in the order of 200 W. The overall power required to run an open wind tunnel can be then estimated in about 17 kW; due to this high value, an open configuration was discarded. So, the closed-loop configuration was taken into account and investigated.

5.2.1 Test section design

The test section should be properly designed in order to accurately reproduce the air dehumidification process realized in the heat pump tumble dryer evaporator. The size of the test samples determinates also the size of the test section and the overall one of the experimental apparatus. Fig. 5.4 represents a drawn of a HPTD evaporator.

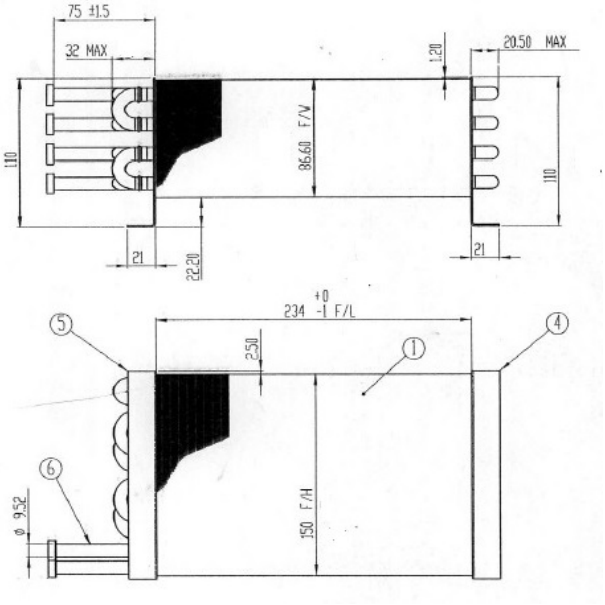

Fig. 5.4 Evaporator geometrical specifications

As can be seen from Fig. 5.4, the evaporator sample has plant dimensions of about 288 mm x 110 mm and an height of about 150 mm. So, a test section of galvanized steel with a square cross sectional area of 300 mm and a length of 500 mm was chosen, according to the standard sizes available on the market. A convergent was inserted to canalize the air flow from the cross sectional area of the test section to the frontal area of the test sample, avoiding also any bypass flow. The heat exchanger is suspended in the middle of the test section height in order to achieve a real time measurement of its weight. The real time measurement of the finned coil weight was obtained with the use of an electronic balance located on the top of the duct. For achieving this measure, the heat exchanger has to be suspended in the middle of the channel; this allocation was realized with a rigid support. The test sample was equipped of two regulation elements that keep the right height of the finned coil in the channel. The suspended heat exchanger, invested by the air flow, tends to swing

backwards due to the drag force. This effect is undesired because it could lead to vibration of the test sample. To solve this issue, two plates having a "L" profile were welded to the sample shoulders in the back. These plates lean against a total number of four screws that inhibit the sample swinging when subject to the air flow. Besides, these screws don't influence the measurement of the heat exchanger weight as they produce only negligible friction forces in the vertical direction. On one side of the test section, a Plexiglas window was located to visualize the condensation process on one border fin. The test section components are represented in Fig. 5.5.

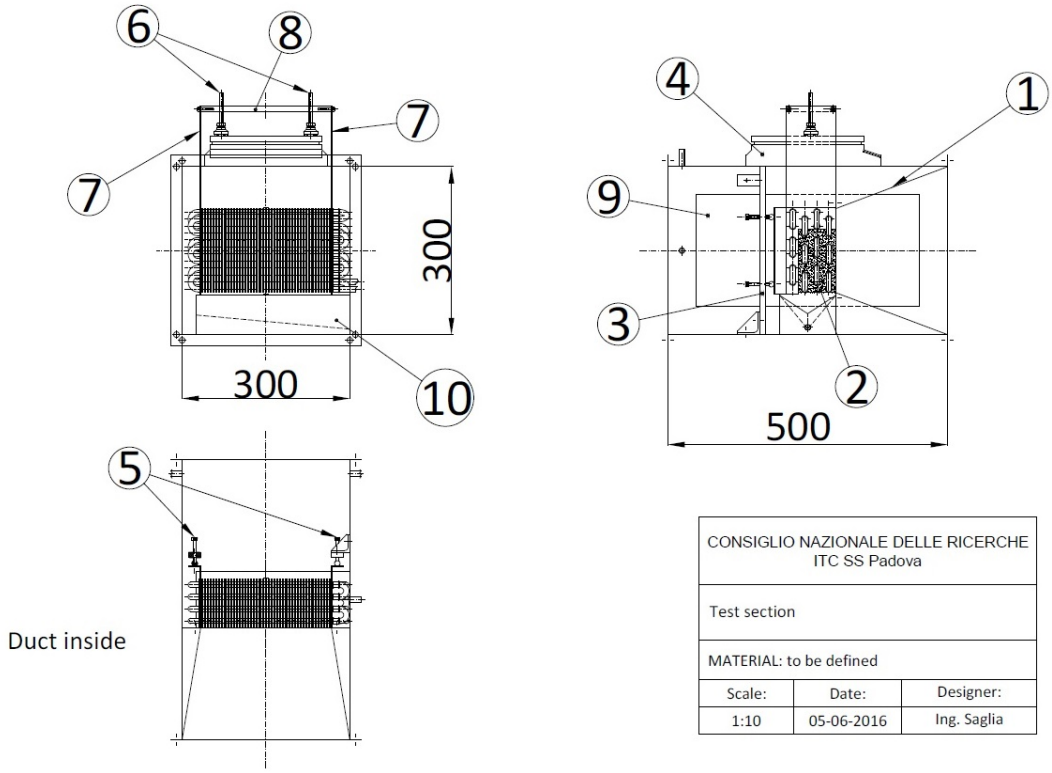

Fig. 5.5 Test section design. 1) Convergent; 2) Finned coil; 3) Screws plate; 4) Balance; 5) M6 screws; 6) Adjustable feet; 7) Finned coil support; 8) Horizontal support; 9) Plexiglas window; 10) Condensate bowl

In a more detail design of the heat exchanger support, two solutions were evaluated as showed in Fig. 5.6 and Fig. 5.7. Solution 1 of Fig. 5.6 provides a heat exchanger support with a couple of plates welded on the top of the sample shoulders. The plate that faces the Plexiglas window is partially cut in order to view the condensation on the border fin. Otherwise, solution 2 provides the replacement of the heat exchanger shoulders with a pair of rigid support having a comb form. This kind of form joints well with the refrigerant tubes of the heat exchanger. Both the solutions have the welded plates on the back for screws location. The vertical plates of the rigid support come out from

the top of the channel and then they are connected together with a horizontal support that lays on the balance for weight measurement, as can be seen in Fig. 5.5.

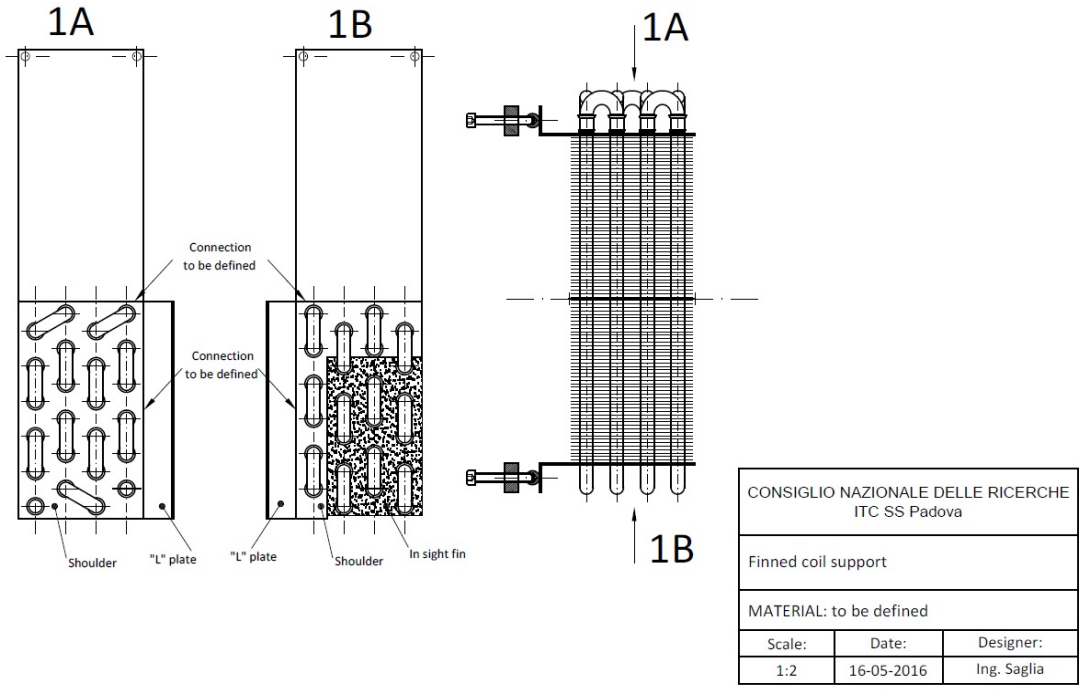

Fig. 5.6 Heat exchanger support (solution 1)

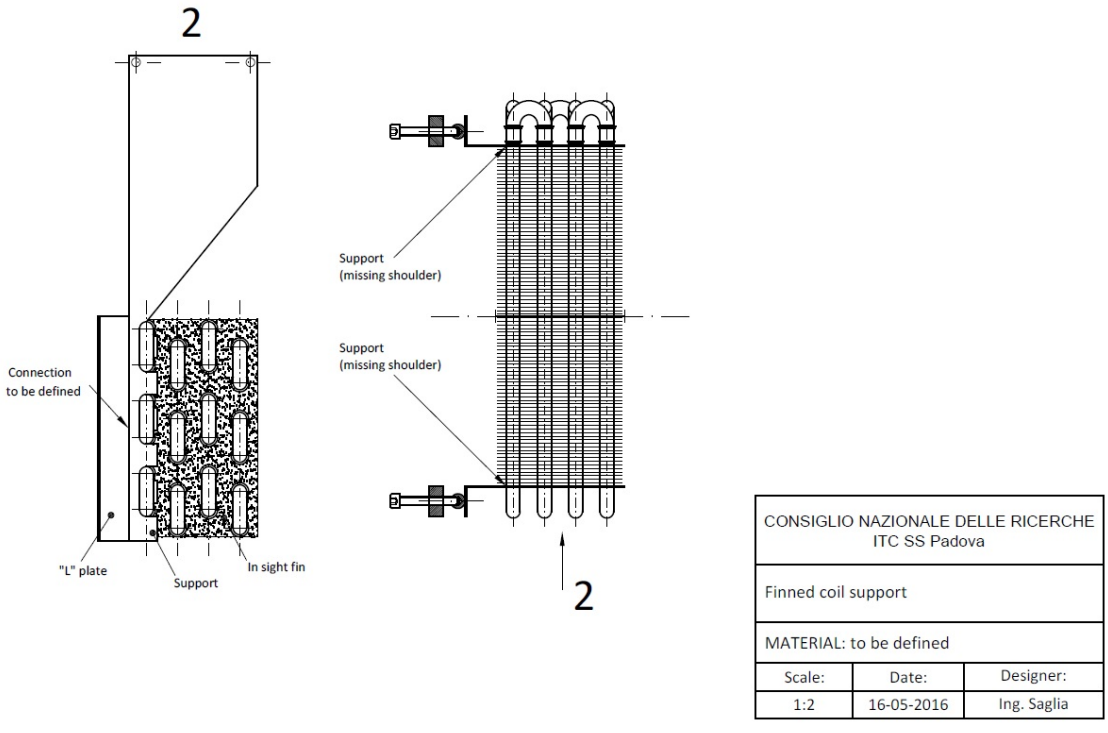

Fig. 5.7 Heat exchanger support (solution 2)

At first, solution 1 was adopted for the test section setup. However, issues related to the connection between the vertical plate and the heat exchanger leaded to rejecting this arrangement. The final adopted solution for the vertical support is represented in Fig. 5.8.

Fig. 5.8 Heat exchanger vertical support

As can be seen from Fig. 5.8, two pairs of hook are coupled with four tubes of the test sample. Each pair is jointed with a vertical rod that comes out from the tunnel inside. These two vertical rods are connected to a transversal bar located on the top of the balance. In the connections points, some dices are inserted for regulating the desired heat exchanger height.

5.2.2 Mixing chamber

The other main element that contributes to the definition of the wind tunnel size is the mixing chamber. In this component, the air flow is heated and humidified in order to reach the desired values of temperature and relative humidity at the inlet of the test section. The mixing process between the air and the injected steam inside the chamber is achieved by an axial fan. The design of this component involves a process of optimization. On one side, the design aims to reduce the overall mixing chamber dimensions, but, on the other side, it has to ensure a good mixing. An

outline of the mixing chamber designed for the experimental apparatus is represented in Fig. 5.9 and Fig. 5.10.

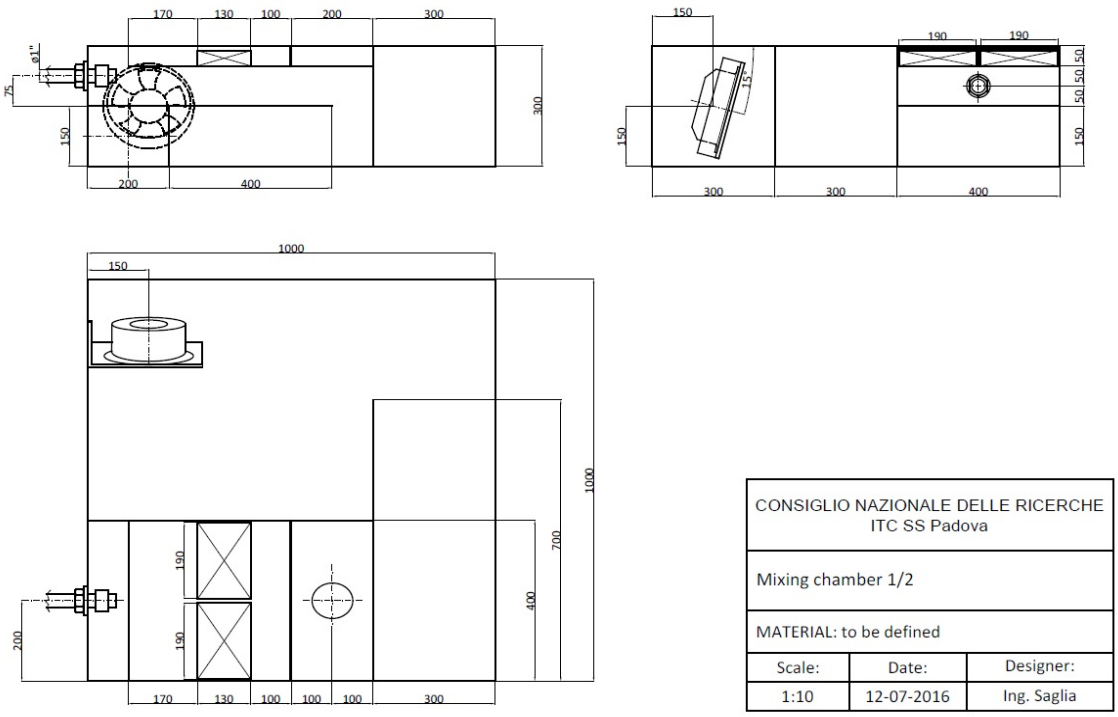

Fig. 5.9 Mixing chamber layout

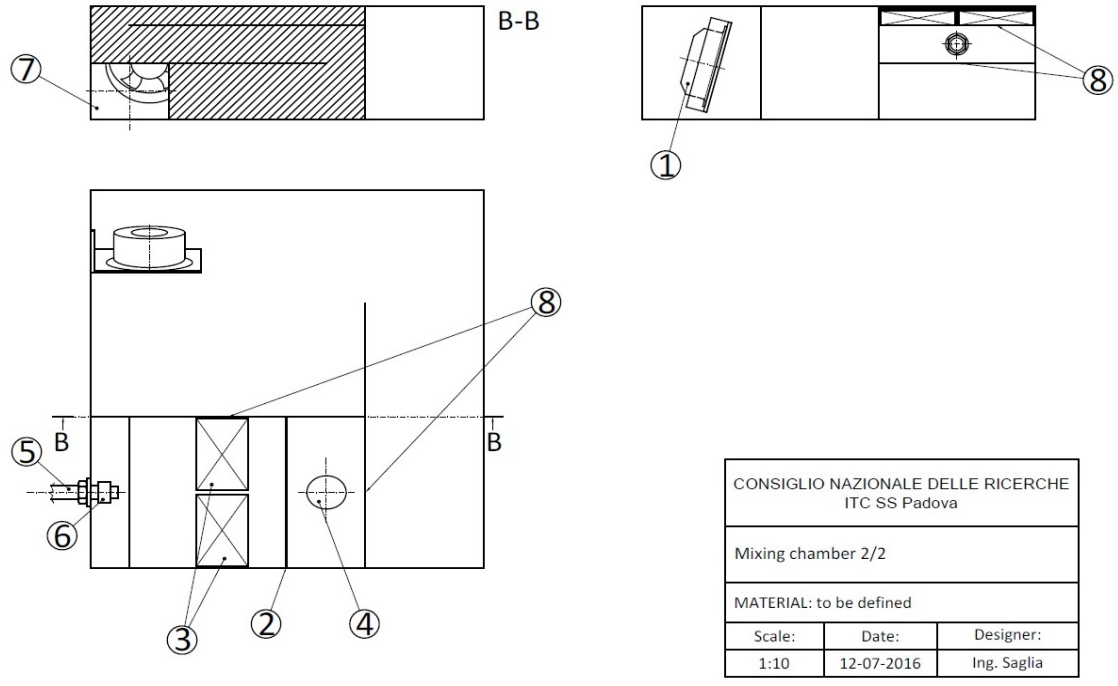

Fig. 5.10 Mixing chamber. 1) EBM fan; 2) Perforated screen; 3) Electrical resistance; 4) Mixing chamber inlet hole; 5) Steam injection tube; 6) Silencer; 7) Passage hole; 8) Separation plate

As can be seen from Fig. 5.9 and Fig. 5.10, the mixing chamber is a parallelepiped with a square base of 1000 mm side and a height of 300 mm, that is the same of the test section. The air flow enters inside the mixing chamber from the top hole and passes through a perforated screen that uniforms the velocity profile. Then, the air is heated passing through two parallel electrical resistances having a total power of 4 kW and it is humidified with the injection of steam, increasing the relative humidity of the air. Before reaching a second section of the chamber, the humid air flow is forced to follow a defined path for improve mixing. The humid air flow is then sent into a second section of the chamber where an axial fan provides further mixing. The fan location arrangement was chosen to assure an optimal mixing degree. At last, the humid air flow exits from the mixing chamber, reaching the inlet of the square duct up to the test section. In Fig. 5.11, the mixing chamber inside is represented.

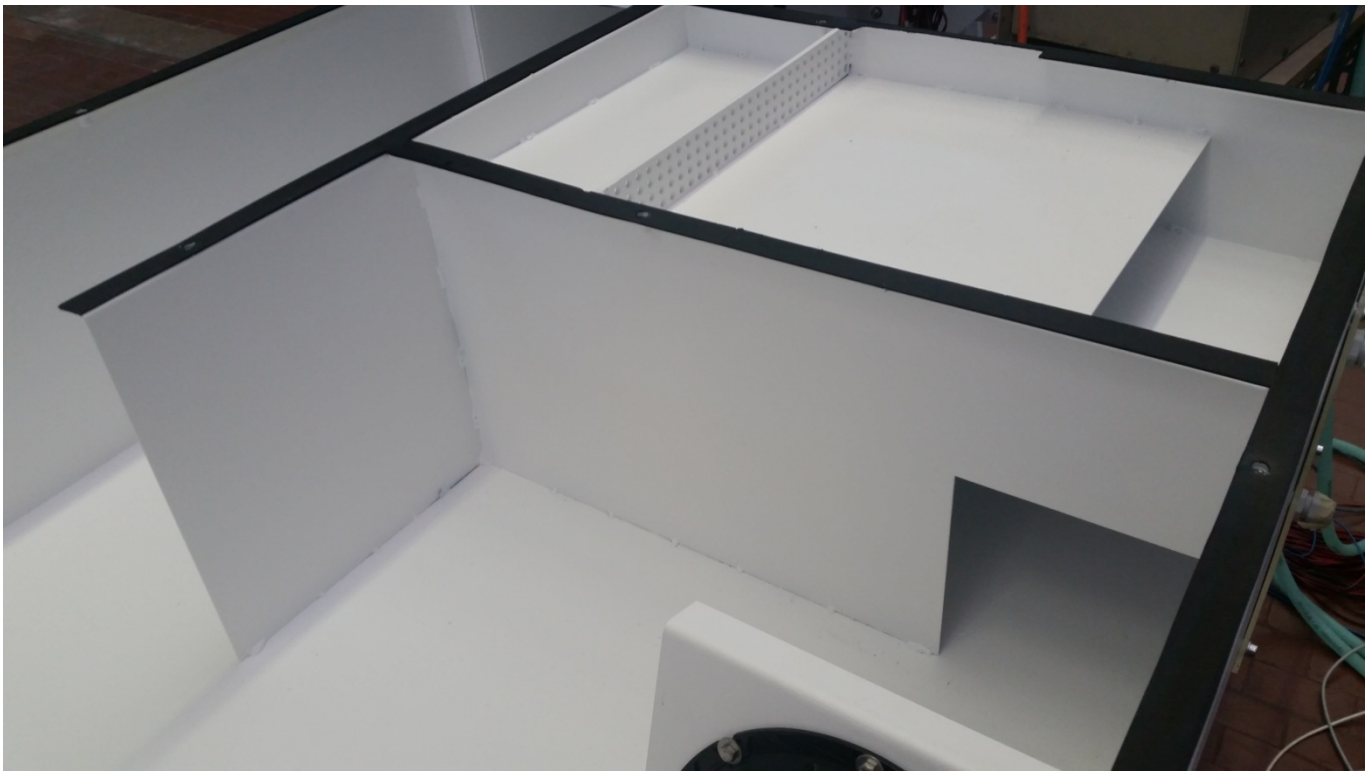

Fig. 5.11 Mixing chamber inside

5.2.3 Wind tunnel global layout

Following the designs of the two main elements of the wind tunnel, a sketch of the experimental apparatus is represented in Fig. 5.12. The overall dimensions of the wind tunnel are about: 6 m in

length, 1 m in height and 1 m in wide. The return duct is located over the one containing the test section; this choice derives from location restrictions.

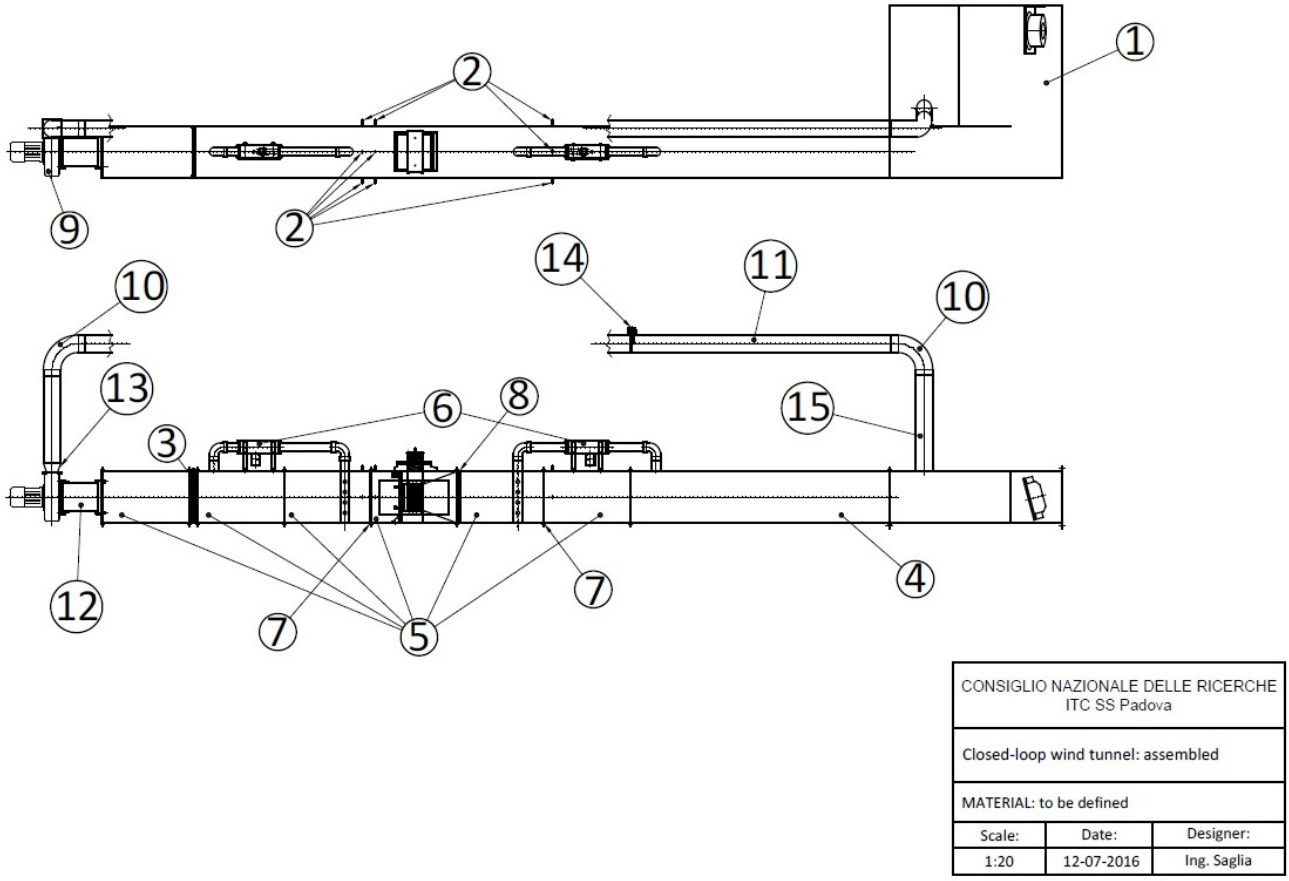

Fig. 5.12 Wind tunnel layout. 1) Mixing chamber; 2) Tube for pressure taps; 3) Air flow regulation device; 4) Steel square duct (300 mm side, 1500 mm length); 5) Steel square duct (300 mm side, 500 mm length); 6) Psychrometer; 7) Square perforated plate (300 mm side, 20 mm length, hexagonal cells); 9) Centrifugal fan; 10) 90° bend; 11) 100 mm tube; 12) Fan inlet junction; 13) Fan-tube connection; 14) Anemometer; 15) Mixing chamber inlet tube.

In Fig. 5.12, starting from the right to the left, the bottom part of the wind tunnel is composed by the mixing chamber, the test section, an air flow regulator and a centrifugal fan. These elements are connected each other with several air duct elements that have standard length of 500 mm or 1500 mm. All of these ducts have the same square cross sectional area of 300 mm. Before and after the test section, the humid air parameters are measured by a psychrometer, located on the top of the channel. These elements are equipped with an axial fan that draws an air sample from the main duct through a tubes grid. Before each tubes grid, a perforated screen is located in order to uniform the air flow. Besides, a honeycomb with hexagonal cells is inserted before the test section for further straightening. After the test section, a regulation element has been provided in order to help the

management of the volumetric air flow into the wind tunnel. The top part of the wind tunnel is composed by a tube of 100 mm of diameter that allows the return of the air flow into the mixing chamber. The equipment for measuring the air mass flow rate is located into this top part of the circuit and sufficient space before and after the instrument was guaranteed for correct readings. Fig. 5.13 shows also an isometric view of the apparatus.

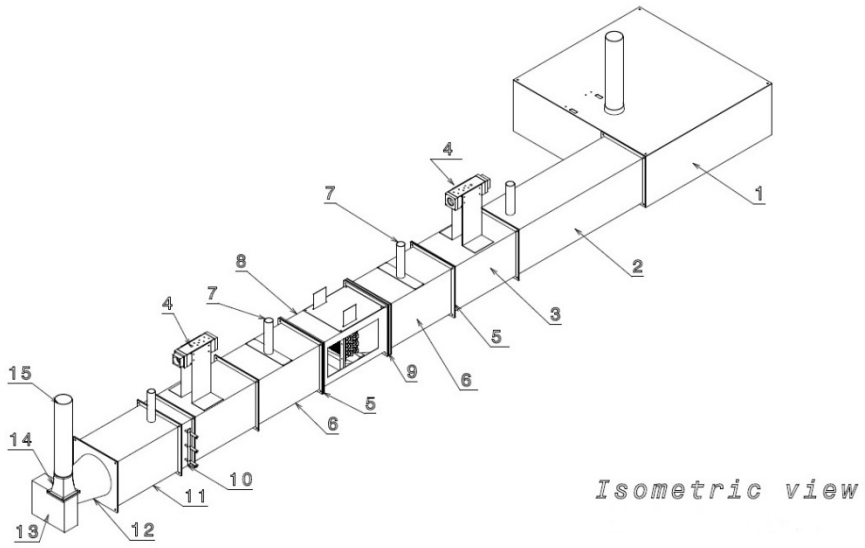

Fig. 5.13 Wind tunnel isometric view. 1) Mixing chamber; 2) 1000 mm duct; 3) 500 mm duct; 4) Psychrometer; 5) Perforated plate; 6) Psychrometer duct; 7) Psychrometer suction grid; 8) Test section; 9) Honeycomb; 10) Adjustable shutter; 11) 500 mm channel with air intake; 12) Duct-fan connection; 13) EBM fan; 14) Fan-tube connection; 15) Return tube.

The wind tunnel was installed at the ITC-CNR of Padua. An electric panel provides to the entire power supply to the experimental apparatus, including the fans, the electrical heaters and the steam generators. A picture of the installation is shown in Fig. 5.14.

Fig. 5.14 Wind tunnel installation

5.2.4 Wind tunnel layout improvements

During the first working year of the experimental apparatus, several layout modifications were carried out in order to improve the accuracy and the repeatability of the tests. At first, the mixing chamber and the square duct up to the second psychrometer were isolated in order to minimize thermal losses to the surroundings. Besides sensible thermal losses, the insulation also provided to avoid condensation on the channel internal sides. For assuring the absence of this phenomenon, a thermocouple was located before the test sample on one channel internal wall for detecting its surface temperature. In addition, an insulating panel was inserted after the second psychrometer in order to avoid conductive thermal losses to the non isolated square channels. An experimental investigation of the velocity and temperature profiles before the first grid temperature detection was carried out. Non-uniform temperature and velocity profiles were found along the square cross section area of the channel. So, an additional screen was inserted before the first temperature grid for levelling out the air flow profiles. The weight measurement setup of the test sample was taken off due to non-repeatability issues during the tests. The test sample location into the duct was then rearranged. A rigid structure was inserted into the test section for keeping the sample in a fixed position. This structure also guarantees a correct transit of the air flow across the heat exchanger.

5.3 Measurement equipment for data acquisition

The main part of the measurement instrumentation is located close by the test section, as can be seen in Fig. 5.15. The properties of the humid air are evaluated before the test section inlet. The dry-bulb and the wet-bulb temperatures of the air flow are measured in a first psychrometer for calculating the humid air enthalpy at the test section inlet. The heat exchanger is fed by coolant

water for achieving air dehumidification. In order to calculated the water side heat transfer rate, the inlet and the outlet temperatures of the coolant are measured. The water volumetric flow rate is measured with a magnetic flow meter. An electronic balance located below the test section allows to measure the drain condensate weight. After the test section, the humid air parameters are evaluated in a second psychrometer and the enthalpy is calculated. In the top tube of the wind tunnel, the measurement of the mass air flow rate is obtained. A hot wire anemometer is inserted in the middle of the tube and a thermocouple measures the air temperature in the same location.

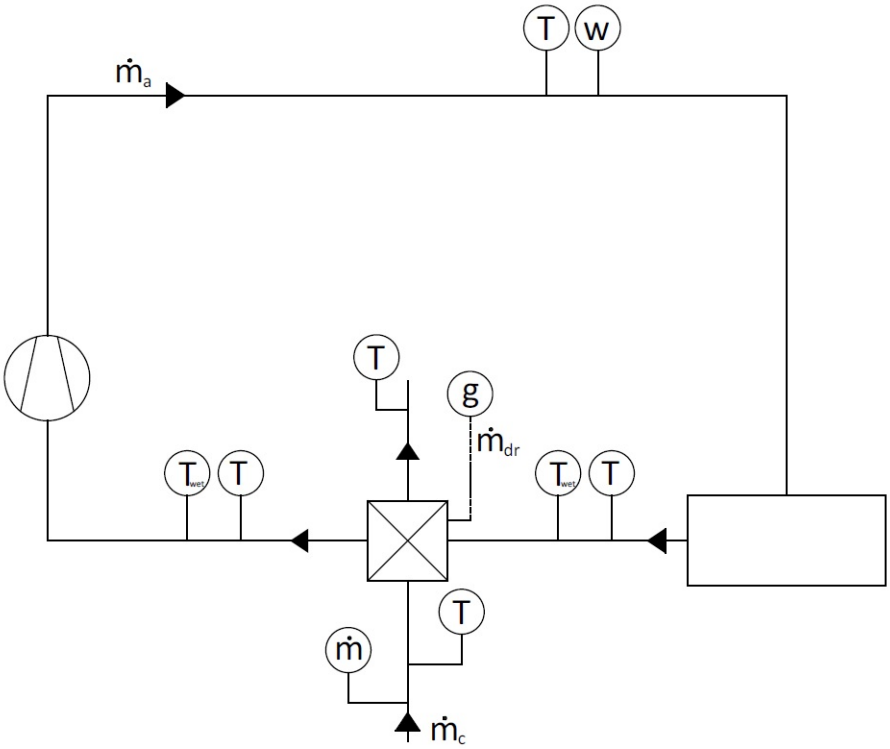

Fig. 5.15 Wind tunnel measurement instrumentation location

5.3.1 Thermocouples

A total number of 33 copper-constantan thermocouples was used in the experimental apparatus for measuring temperature values in different locations. All of the thermocouples were calibrated before the positioning in the test rig in order to obtain an accuracy of ±0.1 °C of the measure; besides, all of them were connected to the same "cold junction". A K170 Ice Point Reference was used for maintaining one of the two thermocouple junctions at a fixed temperature of 0 °C. This equipment allows the connection up to 50 thermocouples; a representation of the Ice Point Reference is shown in Fig. 5.16.

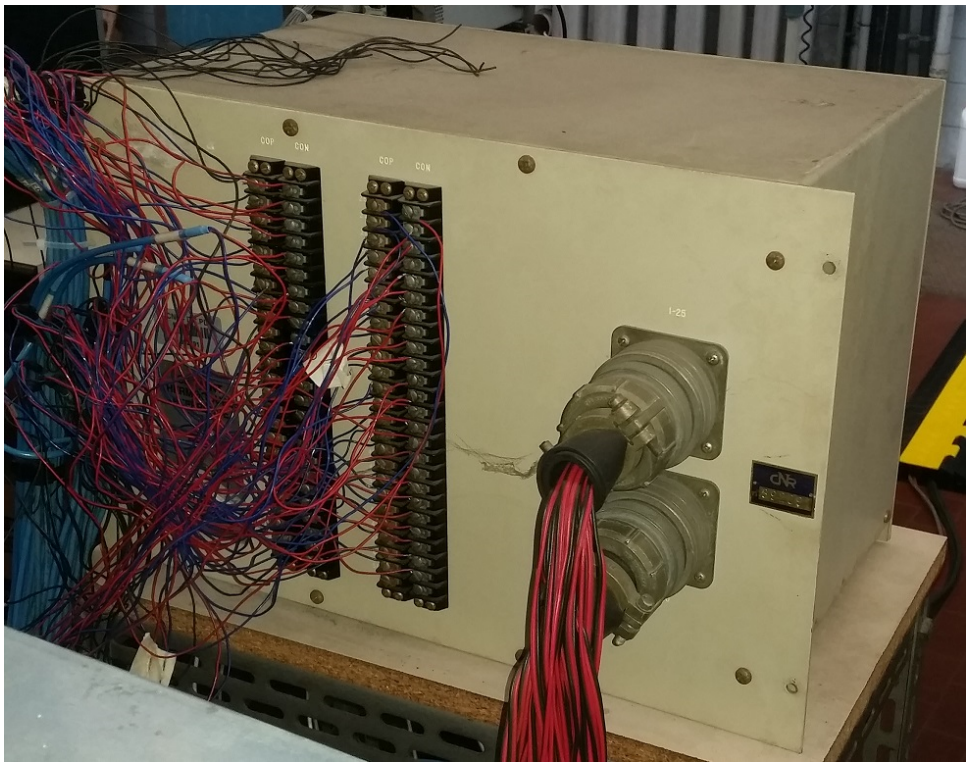

Fig. 5.16 K170 Ice Point Reference

The main part of thermocouples were used for measuring inlet and outlet temperatures of air and water at the test section. One of the two temperature grids, composed of 8 thermocouples, is represented in Fig. 5.17. Eight of them were located into the two psychrometers for obtaining the dry-bulb and wet-bulb temperatures of the air flow. Other thermocouples were used for measuring the ambient temperature near the test section, the vapor temperature after the steam generators and the air temperature in the tube for mass flow rate calculation. One thermocouple was located on the Plexiglas external surface in order to monitoring its temperature. Being this surface without insulation, undesired water condensation on the internal side can occur. In order to avoid this issue, a blow dryer was used to sent hot air to the external surface. From the thermocouple value, the blow dryer power was regulated for keeping the external surface temperature equal to the one in the channel.

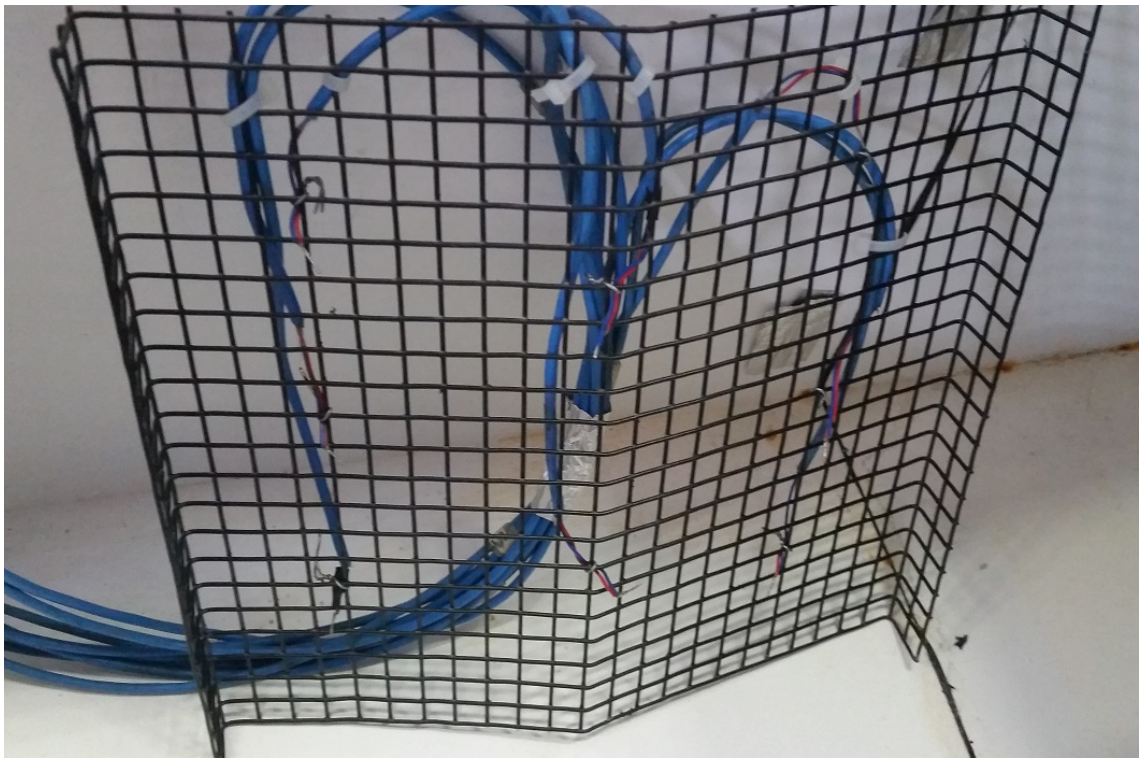

Fig. 5.17 Temperature grid

5.3.2 Relative humidity measurement: psychrometer

Humid air properties have to be evaluated before and after the test section in order to analyze the dehumidification process. The dry-bulb temperature of the humid air can be measured by a thermocouple grid covering the entire cross section area of the duct. On the other hand, the measurement of the wet-bulb temperature of the air flow in the same location is more complicated in absence of electronic instruments. In order to solve this issue, the ANSI/ASHRAE Standard 41.1-1986 [2] indicates a method to measure the air wet-bulb temperature with a psychrometer. An overview of the psychrometer layout is represented in Fig. 5.18. The instrument layout is essentially distinguished into two main parts: the measurement section and the intake system. A fan provides to draw an air sample from one location and to allow its passage across the measurement section. The position of the temperature sensors in the measurement section is fixed in order to avoid measure errors due to the heat produced by the fan operation. The dry-bulb sensors should always be upstream of the wet-bulb ones for obtaining correct readings of the air properties. The moisture evaporation of the wet-bulb sensors leads to incorrect dry-bulb temperature readings if the position of the element is switched. The measurement sensors for dry-bulb and wet-bulb temperatures are usually thermocouples that must guarantee an accuracy of ±0.1 °C of the reading. After the drive system, it is necessary to return the air sample into the drawn location if this sample represents a considerable part of the global air flow.

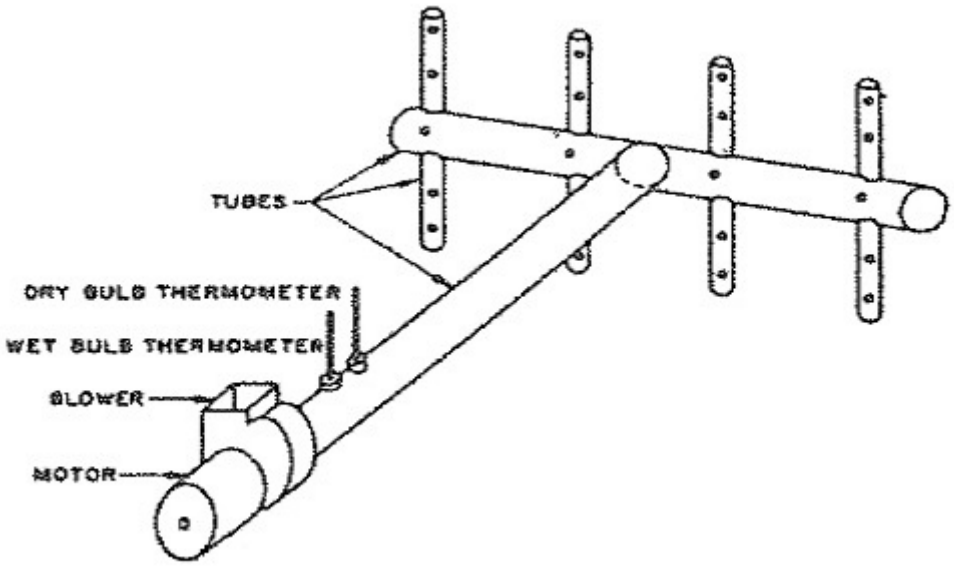

Fig. 5.18 Psychrometer overview [2]

5.3.3 Psychrometer design: measurement section

An example of a wet-bulb element used in the psychrometer measurement section is represented in Fig. 5.19. A frequently used material for the wick is cotton. Cotton has to keep its functionality in time and only distilled water should be used on the wick. If water is continuously supplied by a container, it is important to keep the portion of the wick exposed to the airstream in a length of about 13 mm, that goes from the thermocouple junction to the water reservoir. This length is enough to let the water to reach the wet-bulb temperature before the junction. However, this distance also allows to avoid the wick drying before reaching the optimum wetting of the sensing element. Incoming air conditions at the wet-bulb element have to guarantee a correct reading. Usually, the wet-bulb temperature sensor does not read the true thermodynamic wet-bulb temperature. In fact, the rate of diffusion of moisture from the wetted wick, compared to the rate of diffusion of heat from the sample air to the wetted surface, tends to make the measured wet-bulb temperature lower than the thermodynamic one. On the other hand, heat received by conduction and by radiation from surrounding elements at different dry-bulb temperatures tends to increase the reading of the wet-bulb element. These two effects tend to compensate each other leading to a correct reading of the thermodynamic wet-bulb temperature at certain air velocities. For thermocouple psychrometers, an incoming air velocity of 1.8 m/s is indicative for a properly usage. The wet-blub temperature element must be removed from the psychrometric measurement section each time the container of water has to be reintegrated. For solving this issue, the ANSI/ASHRAE

Standard 41.1-1986 recommends the design of a psychrometric box in order to allow continuous wetting, as showed in Fig. 5.20.

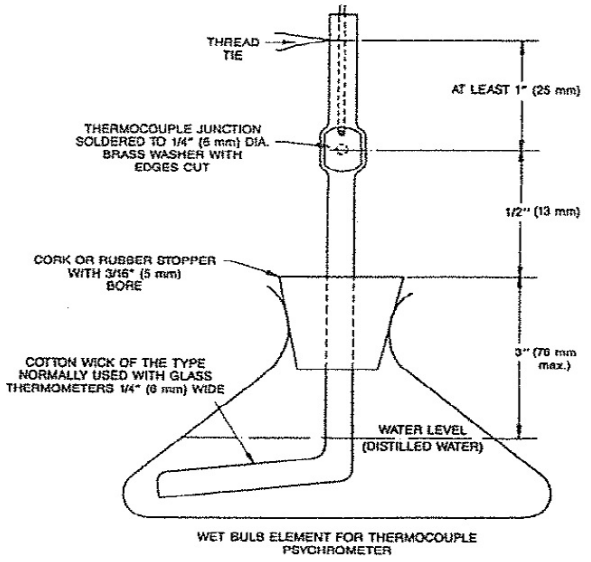

Fig. 5.19 Wet-bulb element for thermocouple psychrometer [2]

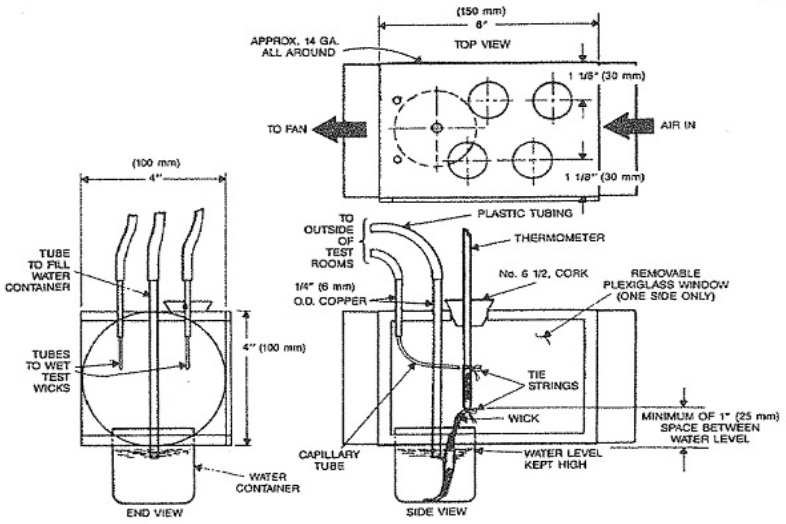

Fig. 5.20 Psychrometer measurement section [2]

At first, the overall size of the box was chosen as suggested from Fig. 5.20. A box with an internal square cross section area of 80 mm side and with a length about 150 mm was considered. These dimensions lead to restrictions in the choice of the fan that allows to take air from the channel and to bring it to the measurement section. As explained before, using thermocouple elements, an air velocity of 1.8 m/s is recommended for correct readings. Having the cross section area of the psychrometer box, the volumetric air flow is calculated according to Eq. 5.4:

$$Q_{v,a} = w_a \cdot A_{box} \tag{5.4}$$

Having A_{box} = 0.0064 m^2 and with w_a= 1.8 m/s, the resulting volumetric flow rate is about $Q_{v,a}$~41 m^3/h. This last value is a considerable part of the volumetric air flow realized in the main channel. So, after the fan, a duct must be provided for returning the air sample into the main channel. In order to minimize the air sample flow path, the measurement section was established to locate on the top of the wind tunnel main square channel. With the values of the design volumetric flow rate and the circuit pressure losses, a suitable commercial axial fan was evaluated. This last element should to be always downstream of the measurement section and instead of putting it outside the box, an integrated solution was considered. This solution causes no problems to the measurement instrumentations because the fan is in suction mode. In order to select a suitable fan that guarantees the balance of the pressure losses and respects the space restrictions, the internal square cross area of the measurement section was reduced to a 60 mm side. The air sample volumetric flow rate was then reduced to a nominal value of about 23 m^3/h. The length of the psychrometer box was increased from 150 mm to 240 mm, in order to allow the housing of the fan. After these first considerations, the psychrometer box was design in details. Six plates compose the measurement section: the top plate, the bottom one and the two plates for air inlet and outlet have a thickness of 10 mm in order to give solidity to the box. The remaining two plates have a thickness of 1 mm due to their covering function; besides, they should be easily removable for inside inspection. The top plate presents seven holes having a 6 mm diameter for allowing the passage of different elements. As can be seen in Fig. 5.20, the first two holes encounter the air flow are predisposed for the dry-bulb thermocouples. After these two elements, another pair of holes is provided for the two wet-bulb thermocouples. These four sensing elements have an accuracy of ±0.1 °C. In the middle of the plate, a hole allows the passage of a plastic tube in order to fill the reservoir for maintaining a high water level. At the plate end, two holes allow to provide water to the test wicks if there are non-wetted zones. The bottom plate, having the same dimension of the top one, presented a single hole where the water container is located. As shown in Fig. 5.20, the minimum distance between the sensing element of the wet-bulb thermocouple and the water level is about 25 mm. The frontal and the back plates are holed for the air inlet and outlet tubes and present the same configuration; the back one also provides to the fan housing. The measurement section design is represented in Fig. 5.21 and a picture of the inside is shown in Fig. 5.22.

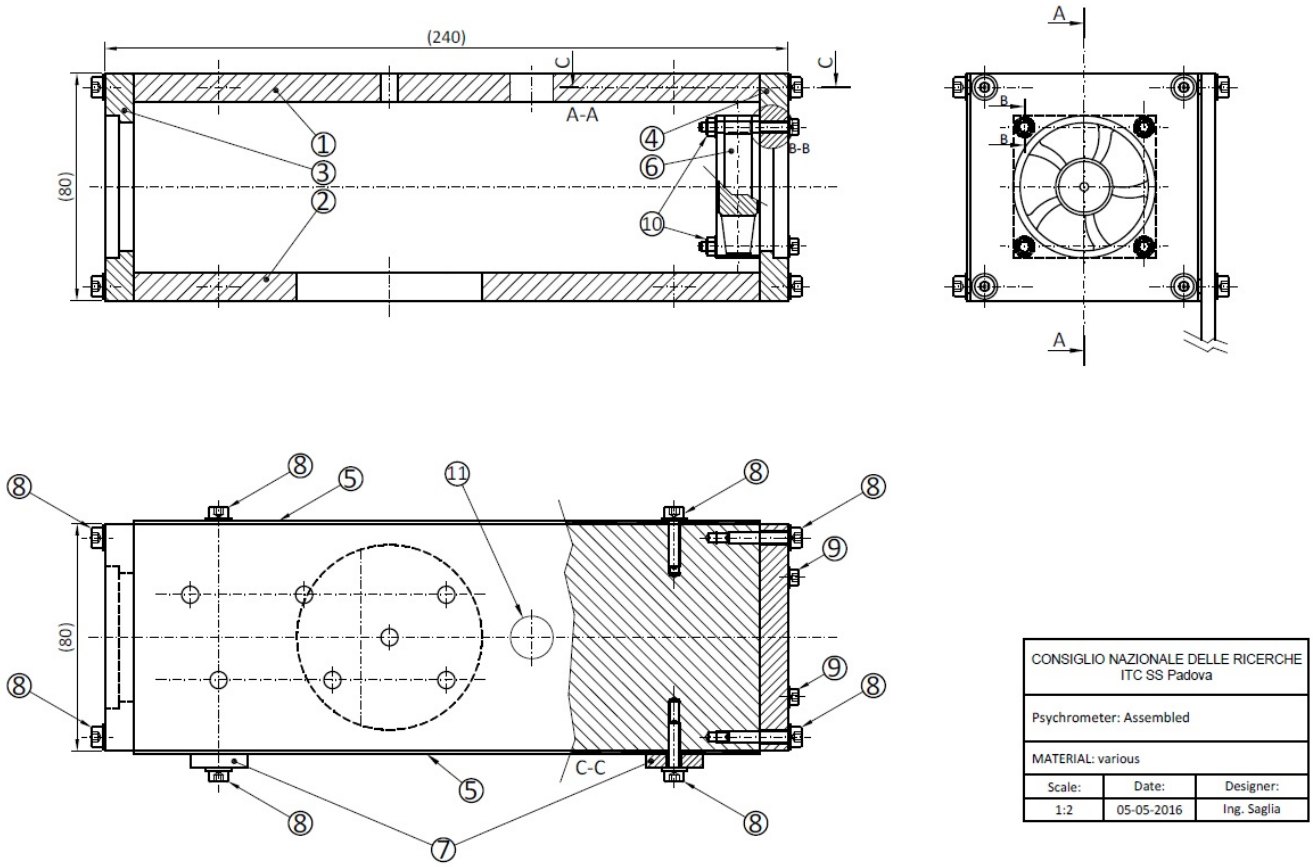

Fig. 5.21 Psychrometer box set. 1) Top plate; 2) Bottom plate; 3) Front plate; 4) Back plate; 5) Side cover; 6) Axial fan; 7) Vertical support; 8) M4 screws; 9) M3 screws; 10) M3 nuts; 11) Inspection hole

Fig. 5.22 Psychrometer box inside

5.3.4 Psychrometer design: tubes grid

The tubes grid allows to draw air from the duct and sent it to the measurement section. This component is composed of a principal collector tube and other transversal perforated tubes embedded into it. The grid is inserted vertically into the channel and every hole faces the incoming air for the sampling. The number of holes of each tube increases from the top to the bottom of the duct. This feature is due to the different path of the air for reaching the measurement section. In order to ensure an uniform sample, more air has to be drawn at the bottom duct. The diameter of the principal collector was chosen equal to 50 mm for keeping the same size until the measurement section inlet. One edge of the collector touches the bottom part of the channel. The transversal tubes have a diameter of 20 mm and they are closed with a stopper at the both ends. Each tube has a different number of passing holes of 10 mm diameter and, in the middle, they are provided of a 16 mm diameter hole. Fig. 5.23 shows a sketch of the tubes grid, while Fig. 5.24 represents a picture of the component.

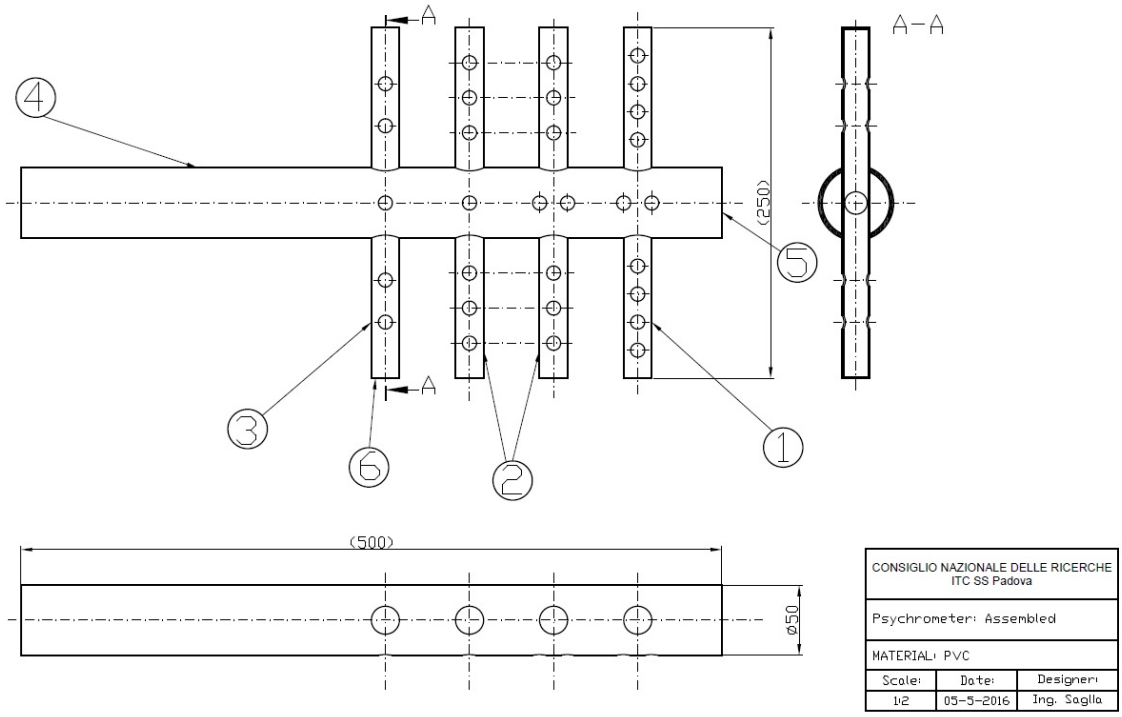

Fig. 5.23 Tubes grid design. 1) 8 holes tube; 2) 6 holes tube; 3) 4 holes tube; 4) Collector; 5) 50 mm stopper; 6) 20 mm stopper

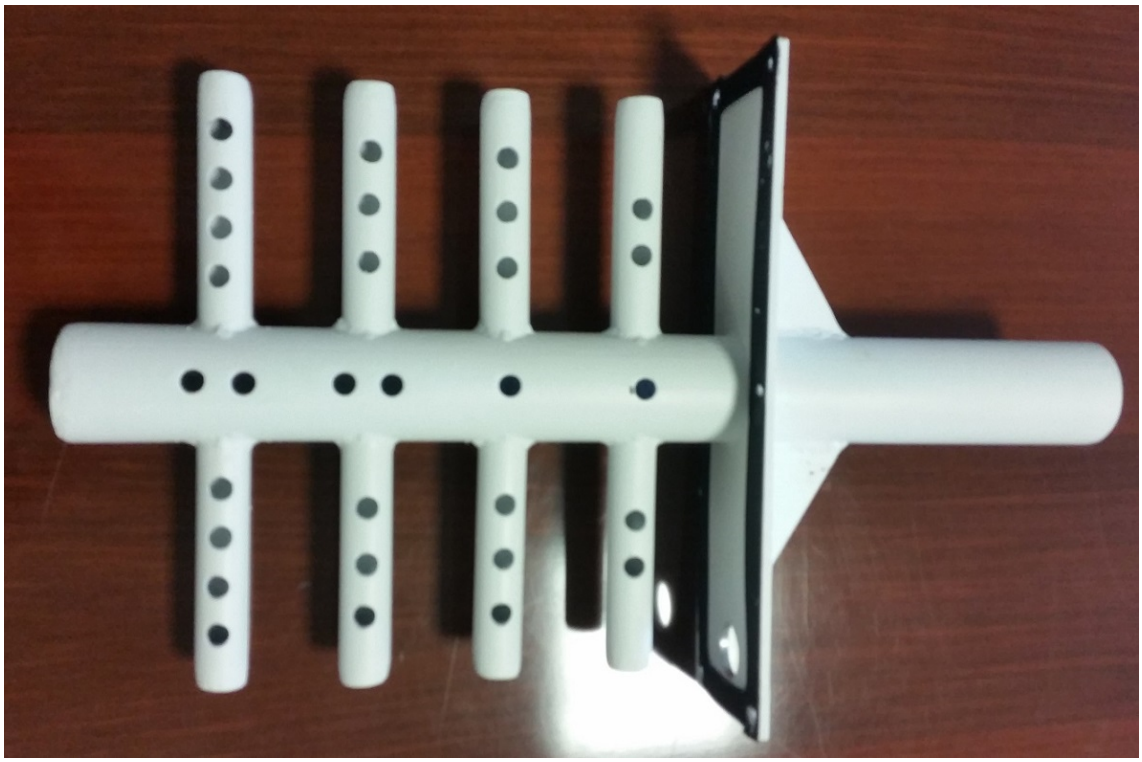

Fig. 5.24 Tubes grid

5.3.5 Psychrometer installation

The two psychrometers are located at first on the top of the channel with a rigid support. They take an air sample from the channel and, after the passage in the measurement section, reject it to the tunnel inside. During the wind tunnel tuning activity, a non-uniform distribution of the air sample was observed between the temperature sensors in each psychrometer. A low ambient temperature could influence the measurement of the wet-bulb elements, leading to miscalculation of the humid air parameters. Experimental tests in no dehumidification conditions were performed at different air inlet temperature at the test section. For relevant difference between the inlet air temperature and the ambient one, the calculated absolute humidity presented different values before and after the test section. Despite the insulation of each psychrometer from the surroundings, issues in miscalculation still remained. So, the psychrometers were located inside the channel, immediately after each temperature grid. The sample velocity for correct measurement of the humid air parameters was assured and the water reservoir has been filled before each test. A representation of the final installation is shown in Fig. 5.25.

Fig. 5.25 Psychrometer final arrangement

5.3.6 Anemometer

In top tube of the apparatus, a hot wire anemometer was inserted in order to acquire the air velocity in the middle of the duct. The instrument presents an accuracy of ±2% of the reading. The values of the maximum velocity at the centre of the tube and the cross section area, the air volumetric flow rate could be calculated. In the same location of the anemometer, a copper-constantan thermocouple was inserted in order to measure the temperature of the air , with an accuracy of ±0.1 °C. The temperature value is useful for calculating the air density. The air mass flow rate can be obtained from Eq. 5.5:

$$\dot{m}_a = 0.9 \cdot w_{a,\max} \cdot \rho_a \cdot A_{tube} \tag{5.5}$$

In Eq. 5.5, the correction factor 0.9 has been obtained through experimental measurements of the velocity distribution along the tube cross section area in turbulent conditions. Besides, experimental measures of the temperature distribution were carried out along the same cross section area, allowing to consider a mean air density value in Eq. 5.5. In Fig. 5.25 a picture of the anemometer sensing element in the tube is shown and, in Fig. 5.26, the external installation of the anemometer and the thermocouple is shown.

Fig. 5.25 Anemometer sensing element

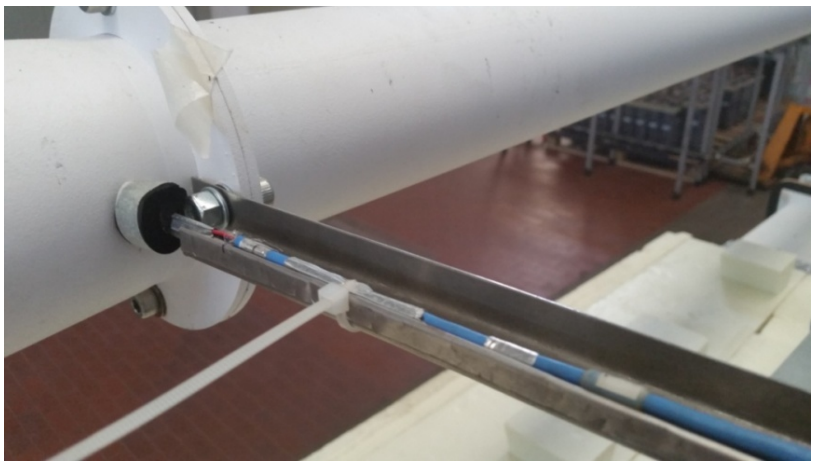

Fig. 5.26 Air mass flow measurement installation

5.3.7 Condensate measurement

During tests in dehumidification conditions, the condensate water falls into a bowl under the finned coil and it is drained outside the channel into a receiver. In order to measure the water condensation rate during tests, the receiver weight is acquired by an electronic balance. A Radwag precision electronic balance (model PS600R2) was used with an accuracy of ±0.01 g. A picture of the measurement set-up is shown in Fig. 5.27.

Fig. 5.27 Condensate measurement set up

5.3.8 Data acquisition unit

The Agilent 34970A, shown in Fig. 5.28 was used as data acquisition unit. The unit is composed by three modules inserted into the back. Each module is composed of 20 channels and can acquire different signals as resistance, AC and DC voltage, AC and DC current. The reading rates can reach values of 500 reading per second on a single channel, while the scan rates can reach up to 250 channels per second. In the experimental apparatus, the Agilent 34970A acquires all of the thermocouple DC voltages, the anemometer DC voltage, the water flow meter DC voltage and the resistance signals of the two NTC thermistors located on the steam generators. The unit communicates though a GPIB interface with the computer acquisition software.

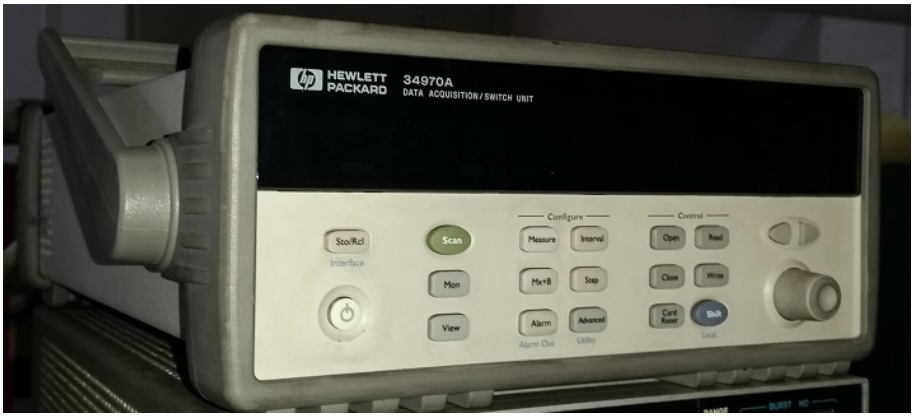

Fig. 5.28 Agilent 34970A

5.4 External equipment and control system

The external equipment allows to keeping the desired air and water conditions during experimental tests. An overview of the equipment location in the test rig is shown in Fig. 5.29.

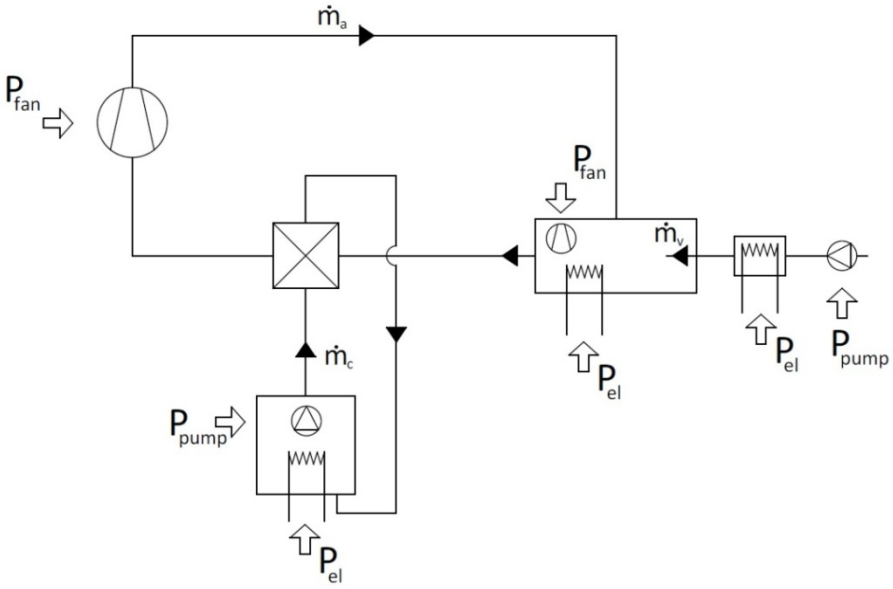

Fig. 5.29 External equipment layout

5.4.1 Chiller

For providing continuous water supply to the test sample at a fixed temperature and flow rate, a chiller was used. The Thermo Scientific NESLAB ThermoFlex2500, represented in Fig. 5.30, is able to set the process fluid temperature from 5 °C to 40 °C, with a temperature stability of ±0.1 °C. Using R134A as refrigerant, a cooling capacity of 2200 W is declared at 20°C. The unit is equipped with a pump that provides the complete recirculation of the coolant from and to the test sample. For regulating the water flow rate, a 3-way valve is installed between the chiller outlet and inlet.

Fig. 5.30 ThermoFlex2500 chiller

5.4.2 Water flow meter

Between the chiller outlet and the test sample inlet, a magnetic flow meter was located for measuring the water volumetric flow rate. A Yokogawa magnetic flow meter model AXF005G, shown in Fig. 5.31, was used in the experimental apparatus. The current output of 4-20 mA was converted into a voltage signal for communication with the acquisition software.

Fig. 5.31 Water flow meter

5.4.3 Electrical heaters and steam generators

Two electrical heaters of a total power of 4 kW are located in the mixing chamber. These elements are positioned in parallel and heat up the incoming air from the top tube before the steam injection. The humidification process is achieved by two steam generators represented in Fig. 5.32, located near the mixing chamber. These components provide a total power of 3 kW; the outlet steam of each generator is mixed before entering in the chamber. Each generator is provided of a diaphragm pump that draws water from a reservoir. The pump duty cycle is set through the use of a function generator, represented in Fig. 5.33. On the external side of each generators, a thermistor is installed for monitoring the wall temperature. In order to avoid high temperatures and electrical damages, an upper limit of the wall temperature was fixed; beyond this value, the power supply is cut off. At the outlet of each steam generator, the fluid temperature is measured by a thermocouple.

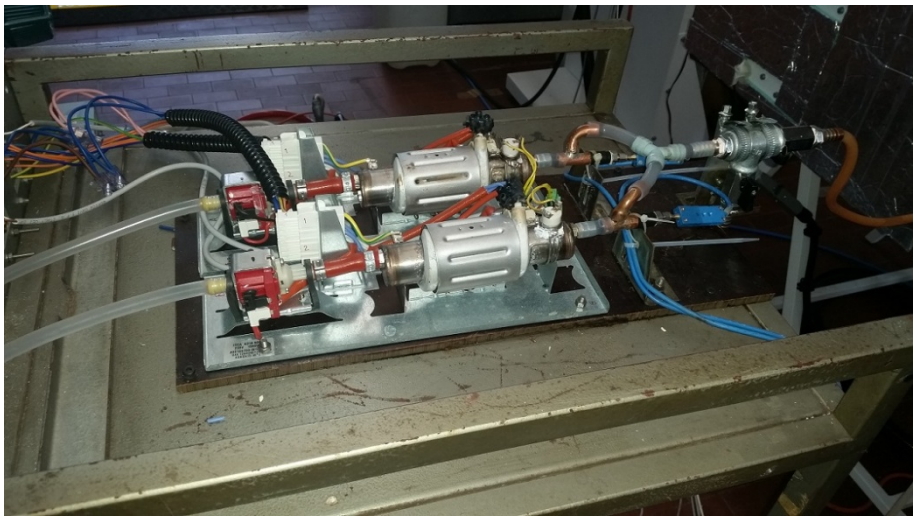

Fig. 5.32 Steam generators

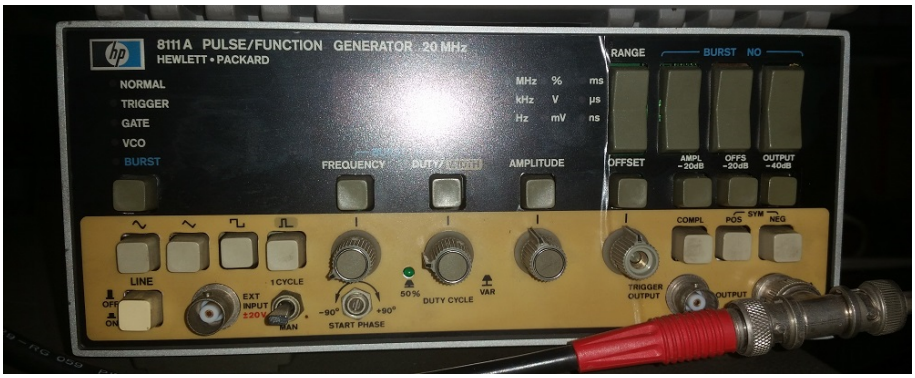

Fig. 5.33 Pulse/function generator

5.4.4 Function generator

Both the electrical heaters and the steam generators are powered in parallel. For providing the power supply, a HP 3497A data acquisition/control unit was used, as shown in Fig. 5.34. This unit communicates with the control software though a HPIB protocol. The requested power dictated by the software is supplied through two output channels 0-10 V range. A power regulator is located between the control unit and the steam generators. In the same way, another power regulator provides to control the electrical heaters power.

Fig. 5.34 HP 3497A

5.4.5 Acquisition & Control software

A Labview program provides to the data acquisition and to control the power supply of the heaters and the steam generators. The main program acquires and stores the measurement data coming from the Agilent, elaborating part of them for having real time values of specific parameters. The sampling frequency of the main program is set at 0.17 Hz. The front panel interface of the program is represented in three parts: Fig. 5.35, Fig. 5.36, Fig. 5.37. Before each test, the inlet set point values of air and absolute humidity and water temperature are established. As can be seen from Fig. 5.35, the main air parameters are acquired and displayed in the front panel, such as the mean temperature at the two grids, the respective enthalpy and the mass flow rate. The temperature values of the eight thermocouples of each grid are also represented as a function of time in two x-y graphs, as shown in Fig. 5.36. The values of the humid air enthalpy are calculated with the air parameters obtained into the psychrometers. For each psychrometer, the dry-bulb and wet-bulb temperatures are displayed as the calculated values of dew point temperature, absolute and relative humidity. An indicator also highlights the real time difference between the two absolute humidity for monitoring the test conditions. In Fig. 5.37, the second part of the front panel is shown. The water inlet and outlet temperatures are displayed as the mass flow rate. The electrical heaters power can be fixed manually. A diagram of the control procedure is represented in Fig. 5.38. For keeping air to a fixed temperature value at the heat exchanger inlet, a PI controller provides to regulate the electrical heaters power acting on the difference between the first grid mean temperature and the set point value. As for the heaters, the steam generators power and the duty cycle of the pumps can be fixed manually. For keeping air to a fixed absolute humidity value at the heat exchanger inlet, a second PI controller modulates the power of the steam generators according to the difference between the absolute humidity at the first psychrometer and the set point value. The steam generators wall

temperatures are also displayed. At last, the weight of the water condensate receiver is acquired it is represented as a function of time in a x-y graph.

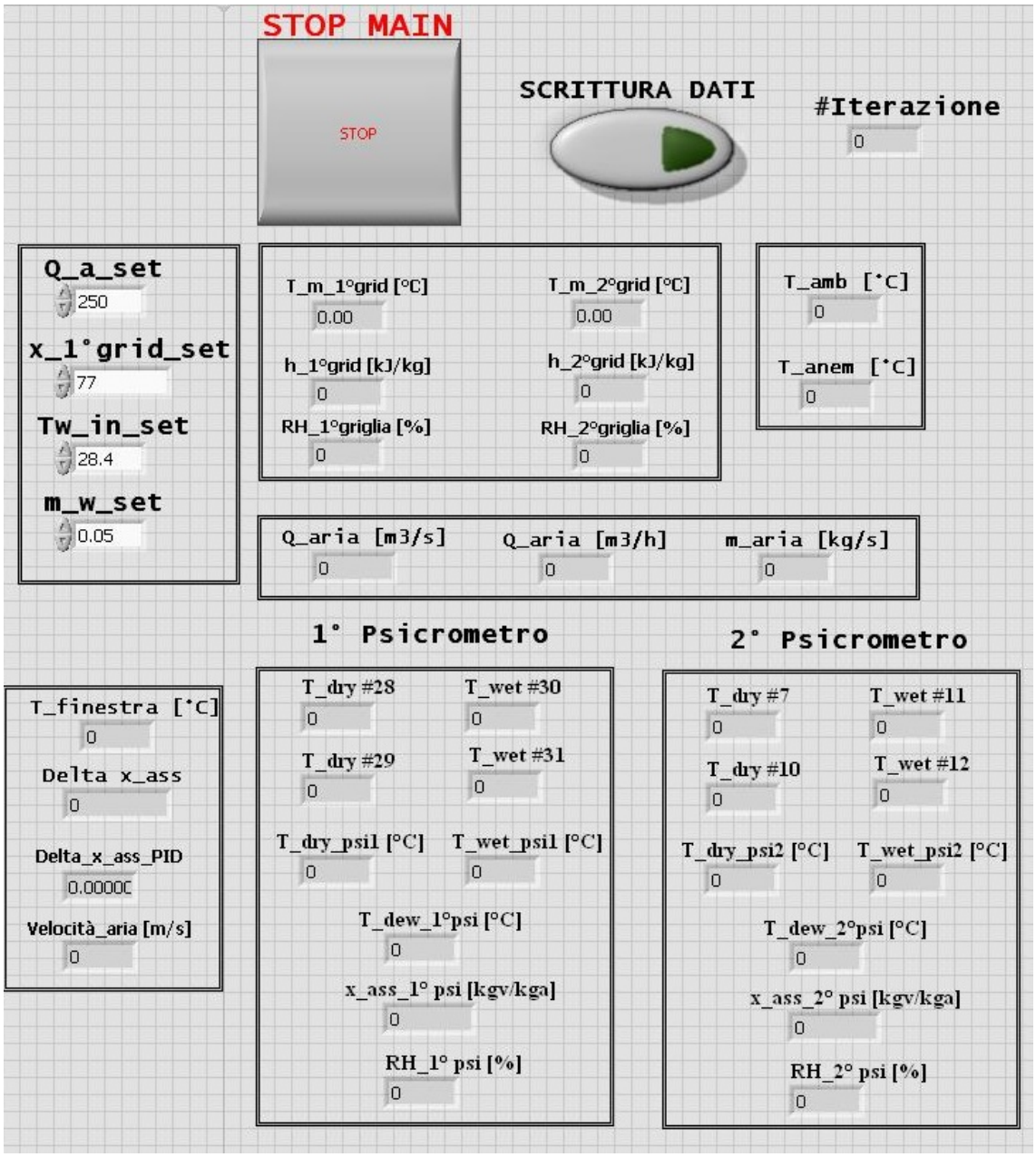

Fig. 5.35 Main program front panel (part 1)

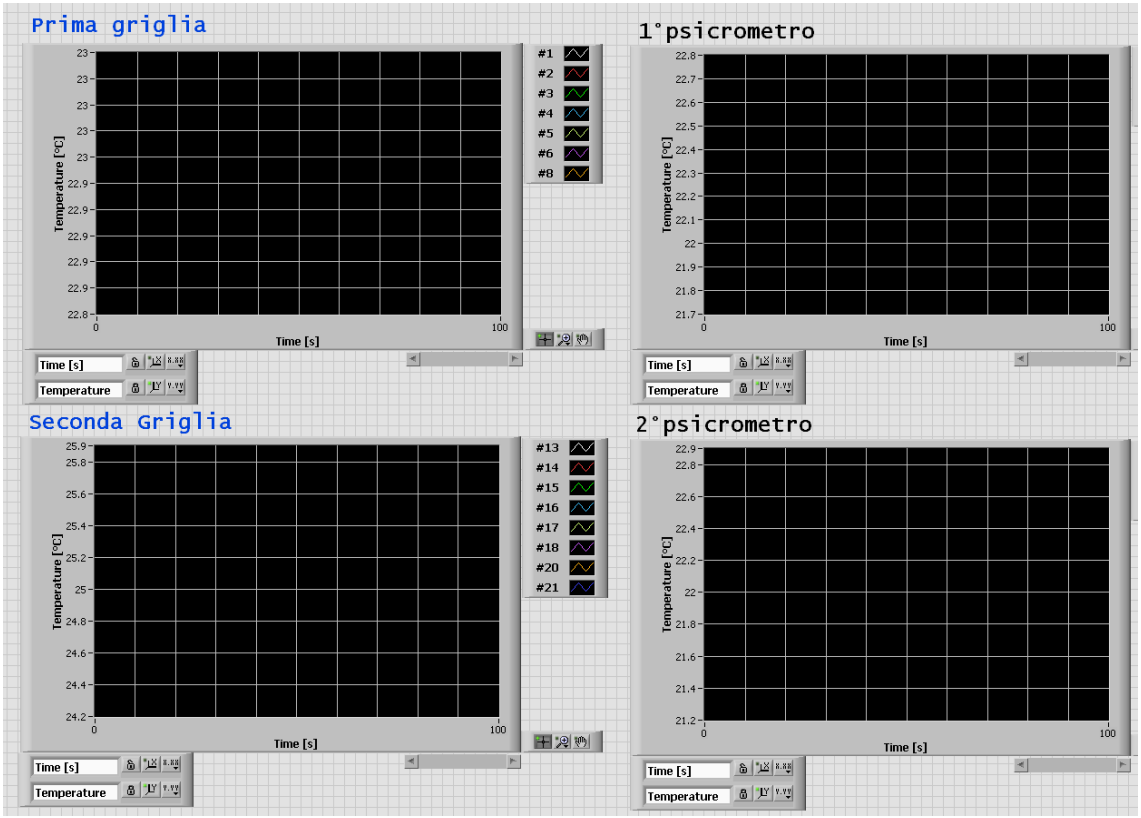

Fig. 5.36 Main program front panel (part 2)

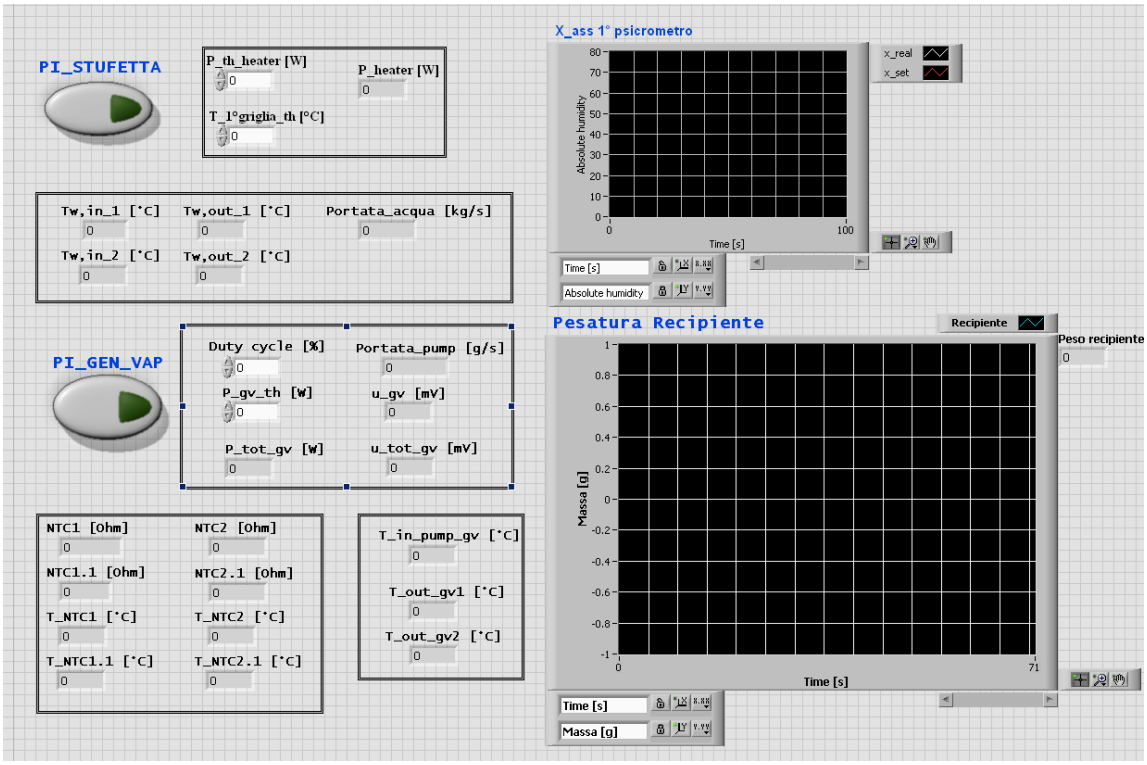

Fig. 5.37 Main program front panel (part 3)

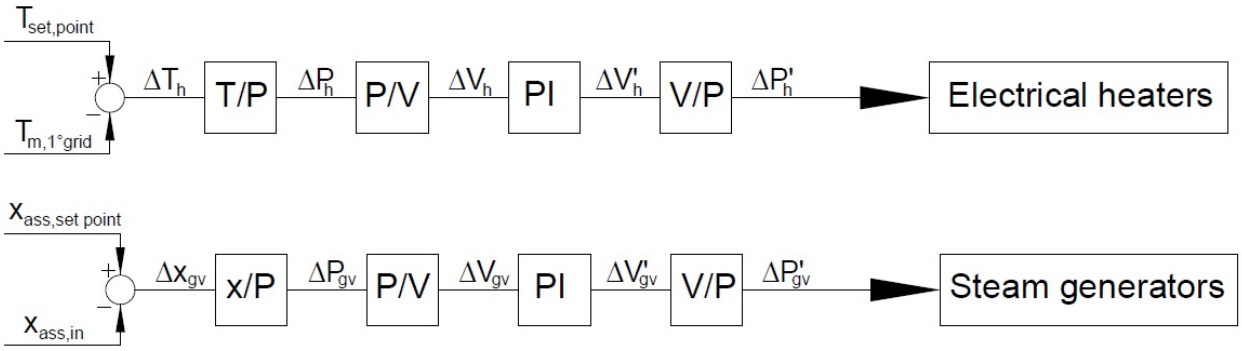

Fig. 5.38 Control diagram

5.5 References

[1] Cattafesta L., Bahr C., Mathew J., Fundamentals of wind-tunnel design, Encyclopedia of Aerospace Eng., 2010.

[2] ANSI/ASHRAE Standard 41.1-1986 (RA 2001), Standard Method for Temperature Measurement.

6 Experimental tests in dry and wet conditions for a plain fin sample and model comparison

6.1 Activity overview

Firsts experimental tests were carried out on a heat exchanger with plain fins. In order to characterize this sample, an evaluation of the air side sensible heat transfer coefficient as a function of the frontal air velocity was performed. After tests in dry conditions, further tests were carried out in dehumidification conditions at different relative humidity of the inlet air at the test section. Experimental results were then compared with different dehumidification models to achieve good predictions.

6.2 Experimental methods

6.2.1 Description of the test sample

This sample had the same geometry shown in Fig. 4.1, but it was built with plain fins of 0.12 mm thickness; the whole geometrical characteristics are described in Table 6.1. The fins were made of bare aluminium, having the same static and advancing contact angles as explained in Section 4.7. The coolant path into the sample is characterized by one inlet tube and one outlet tube. This arrangement was required by the need of a water Reynolds Number higher than 10000 in the air side heat transfer coefficient evaluation. In Fig. 6.1, a representation of this arrangement is shown.

Fig. 6.1 Heat exchanger water circuit

Table 6.1

Test sample geometrical characteristics

Length [mm]	234
Width [mm]	88
Height [mm]	155
Tubes arrangement	Staggered
N° rows	4
N° tubes per row	6
Fin pitch [mm]	2
Rows pitch [mm]	21.5
Tubes pitch [mm]	25
External diameter [mm]	9.52
Fin type	Plain
N° fins	117
Tube thickness [mm]	0.711
Fin thickness [mm]	0.12

6.2.2 Air side heat transfer coefficient evaluation procedure

Tests in dry conditions were performed in order to evaluate the air side heat transfer coefficient at different air velocities. The tunnel was opened, thus resulting in an open air circuit; then, for all the tests, the air temperature at the inlet of the test section was kept equal to the ambient one, while the inlet water temperature was maintained constant at 55 °C. The water inlet conditions were achieved through the use of electrical resistances; one of them was incorporated with a temperature PID controller for keeping constant the inlet water temperature. The water circulation was achieved by a centrifugal pump that assured a constant flow rate of 240 l/h for all the tests. So, the resulting Reynolds Number was higher than 10000. After the pump, the magnetic water flow meter was located. A picture of the water equipment is represented in Fig. 6.2. Dry test conditions are summarized in Table 6.2.

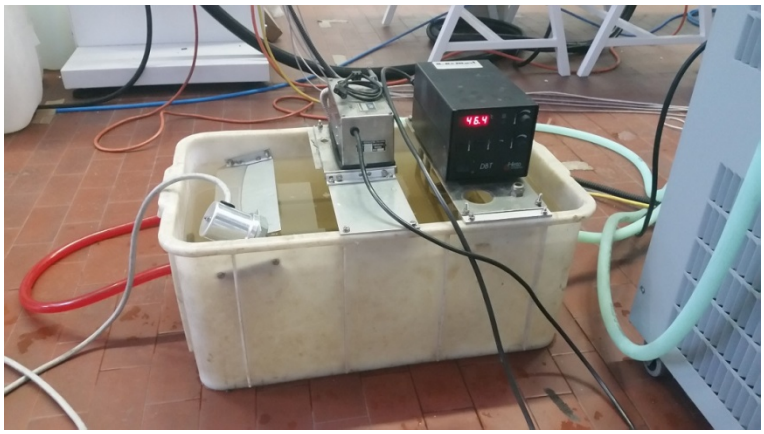

Fig. 6.2 Water electrical heaters

Table 6.2

Dry test conditions

$T_{a,in}$ [°C]	$RH_{a,in}$ [%]	$w_{a,fr}$ [m/s]	$T_{w,in}$ [°C]	$\dot{m}_w$ [g/s]	Re_w
26	50	0.8-2.8	55	68	10600-10700

6.2.3 Dehumidification tests procedure

Before each test, the balance was previously zeroed and the psychrometer water reservoirs were filled. The water in the chiller was cooled in order to reach the desired temperature at the heat exchanger inlet of the specific test. For all the tests, the air inlet temperature and the air flow rate were maintained constant, respectively, to 43 °C and 250 m^3/h. The relative humidity was increased from 30% up to 92%. The inlet coolant temperature and coolant flow rate were kept constant, respectively, to 25 °C and 180 l/h. The condensate water mass flow was calculated as weight difference of the balance between successive acquisitions. An experiment started with the circulation of the air flow, bringing it to the desired temperature and velocity. The first step of each test was the evaluation of the thermal losses along the test section to the surroundings, fixed the air inlet temperature, as described in Appendix A. These losses must be taken into account due to the high temperature difference between the tunnel inside and the ambient temperature. After reaching steady state conditions, the thermal losses evaluation lasted for 15 minutes. Next, the water initiated to circulate for cooling the heat exchanger, maintaining the temperature of the entire external surface below the dew point temperature of the inlet air. The recording was carried out after reaching steady state conditions and it lasted for 30 minutes. Tests dehumidification conditions are summarized in Table 6.3.

Table 6.3

Dehumidification test conditions

$T_{a,in}$ [°C]	$Q_{v,a}$ [m³/h]	$RH_{a,in}$ [%]	$x_{ass,in}$ [g_v/kg_a]	$T_{w,in}$ [°C]	$\dot{m}_w$ [g/s]	Re_w
43	250	30-92	17-50	25	50	7800

6.3 Data reduction

The post processing of the data was carried out according to rate equation and energy balances between air and coolant sides. The thermodynamic properties of the fluids were evaluated with Refprop 9.1 [1], allowing to calculate the mass flow rates. For tests without dehumidification, a log-mean temperature difference (LMTD) method was used. On the other hand, for tests in dehumidification conditions a log-mean enthalpy difference (LMED) method was employed. The uncertainty analysis of the data was also performed according to JCGM 100:2008 [2], both in dry and in dehumidification conditions. The values of the accuracy of the instruments and the uncertainties of the calculated parameters are reported in Table 6.4.

Table 6.4

Accuracy of the instruments and uncertainties of calculated parameters

Accuracy	
Thermocouple	±0.1 °C
Anemometer	±2% of the reading
Water flow meter	±0.35% of the reading
Balance	±0.01 g
Uncertainty	
RH	±1.5%
Q_w	±2.4%
Q_a (dry conditions)	±2.7%
Q_a (DH conditions)	±5.2%

6.3.1 Data reduction in dry conditions

Test in dry conditions were performed in order to evaluate the air side heat transfer coefficient. For the two fluids, the heat transfer rates were calculated according to the mass flow rate and the temperature change of each side, as expressed in Eq. 6.1 and Eq. 6.2:

$$Q_a = \dot{m}_a \cdot c_{p,a} \cdot (t_{a,out} - t_{a,in}) \tag{6.1}$$

$$Q_w = \dot{m}_w \cdot c_{p,w} \cdot (t_{w,in} - t_{w,out}) \tag{6.2}$$

A log-mean temperature difference (LMTD) method was used for evaluating the overall heat transfer coefficient, as shown in Eq. 6.3.

$$Q_{m,d} = U_d \cdot A_e \cdot \Delta t_{ml} \cdot F \tag{6.3}$$

In Eq.6.3, $Q_{m,d}$ is the arithmetic mean of the heat transfer rates of each fluid, U_d is the overall heat transfer coefficient in dry conditions, A_e is the external heat transfer area and Δt_{ml} is defined as follows (Eq. 6.4):

$$\Delta t_{ml} = \frac{(t_{a,in} - t_{w,out}) - (t_{a,out} - t_{w,in})}{\ln\left(\frac{t_{a,in} - t_{w,out}}{t_{a,out} - t_{w,in}}\right)} \tag{6.4}$$

In Eq. 6.3, F is the correction factor equal or less than one due to non-pure counterflow conditions. However, its value is close to the unit for the considered geometry. The overall heat transfer coefficient, related to the external heat transfer surface, can be expressed as shown in Eq. 6.5:

$$U_d = \frac{1}{\frac{A_e}{\alpha_i \cdot A_i} + \frac{A_e \cdot \ln(r_e/r_i)}{2 \cdot \pi \cdot l \cdot k_{Cu}} + \frac{1}{\alpha_e \cdot \Omega_e^*}} \tag{6.5}$$

where α_i and α_e are, respectively, the internal and external convective heat transfer coefficients and Ω_e^* is the overall external surface efficiency. Usually, the conductive term referred to the heat exchanger tube is negligible respect to the others. For the calculation of the internal convective heat transfer coefficient, the correlation proposed by Gnielinski [3] was used.

6.3.2 Data reduction in dehumidification conditions

Tests in dehumidification conditions were characterized by the presence of latent heat in the overall heat transfer rate. This contribution was taken into account considering the air enthalpy difference, as shown in Eq. 6.6:

$$Q_a = \dot{m}_a \cdot (h_{a,in} - h_{a,out}) \tag{6.6}$$

Air enthalpy at the inlet and at the outlet of the test section were calculated from values of the dry bulb temperature, the wet bulb temperature and the ambient pressure. The test section energy balance is expressed in Eq. 6.7:

$$Q_a - Q_{diss} = Q_w + Q_{dr} \tag{6.7}$$

where Q_{dr} and Q_{diss} are, respectively, the heat transfer rates related to the condensate and the thermal losses to the surroundings. These terms are defined as follows:

$$Q_{dr} = \dot{m}_{dr} \cdot h_{dr} \tag{6.8}$$

$$Q_{diss} = Q_a\big|_{Q_w=0} \tag{6.9}$$

In Eq. 6.8, the enthalpy of the condensate is calculated at the air outlet temperature.

6.4 Air side heat transfer coefficient evaluation

Following the procedure explained in Section 6.2.2, the air side heat transfer coefficient for the untreated plain fin sample was evaluated. Tests were carried out at different air volumetric flow rates and with a constant coolant flow rate in turbulent conditions (Re_w > 10000). For these tests, a maximum relative discrepancy between air and water heat transfer rates ($|Q_a\text{-}Q_w|/Q_{m,dry}$) was found equal to ±2%. The air side heat transfer coefficient and the overall external surface efficiency can be expressed as a function of the frontal velocity [4], as shown in Eq. 6.10:

$$\alpha_e \cdot \Omega_e^* = a \cdot w_{a,fr}^b \tag{6.10}$$

where coefficients a and b have to be calculated from experimental data. The frontal velocity at the heat exchanger is obtained from Eq. 6.11:

$$w_{a,fr} = \frac{\dot{m}_a}{\rho_a \cdot A_{fr}} \tag{6.11}$$

where the air density is calculated at the inlet air temperature. Test results are shown in Fig. 6.3 and summarized in Table 6.5

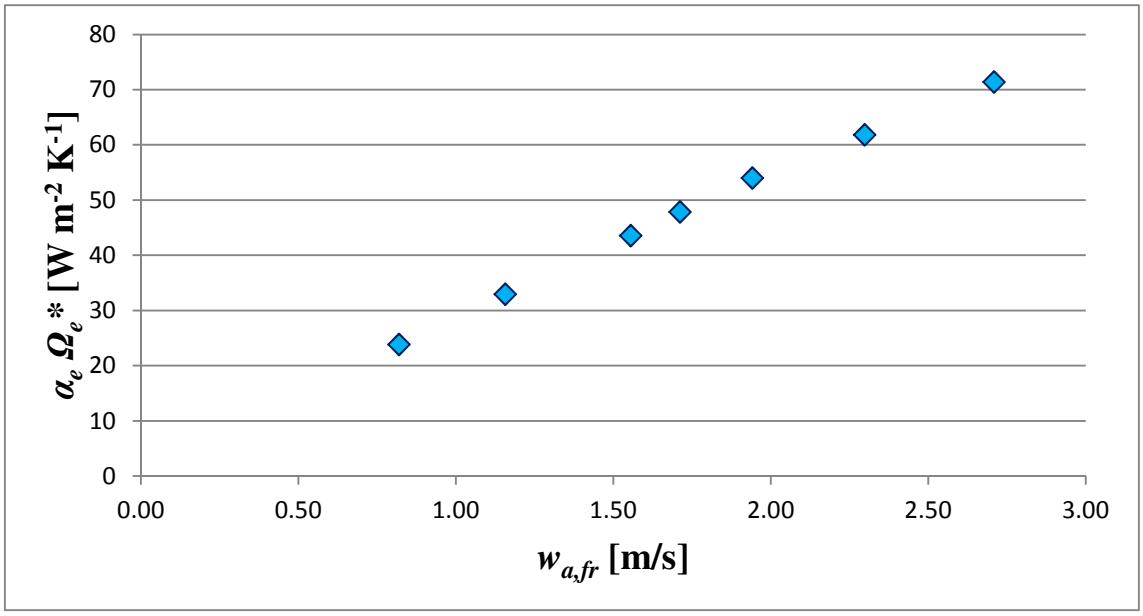

Fig. 6.3 Air side heat transfer coefficient for the sample with bare plain fins

Table 6.5

Air side heat transfer coefficient results

$w_{a,fr}$ [m/s]	0.82	1.16	1.56	1.71	1.94	2.3	2.71
$\alpha_e \Omega^*_e$ [W m^{-2}K^{-1}]	24	33	44	48	54	62	71

Tests have shown an increase of the air side heat transfer coefficient with the increase of the air frontal velocity. In order to evaluate the coefficients *a* and *b* of Eq. 6.10, a power regression was performed on the data. The resultant correlation is expressed in Eq. 6.12:

$$\alpha_e \cdot \Omega_e^* = 28.88 \cdot w_{a,fr}^{0.921} \tag{6.12}$$

Experimental data of Fig. 6.3 were compared with two literature heat transfer correlations for plain fin-and-tube heat exchangers. The first correlation was proposed by Gray & Webb [5], while the second one was described by Wang [6]. The comparison between the experimental data and the two correlations values is shown in Fig. 6.4 for different air frontal velocities.

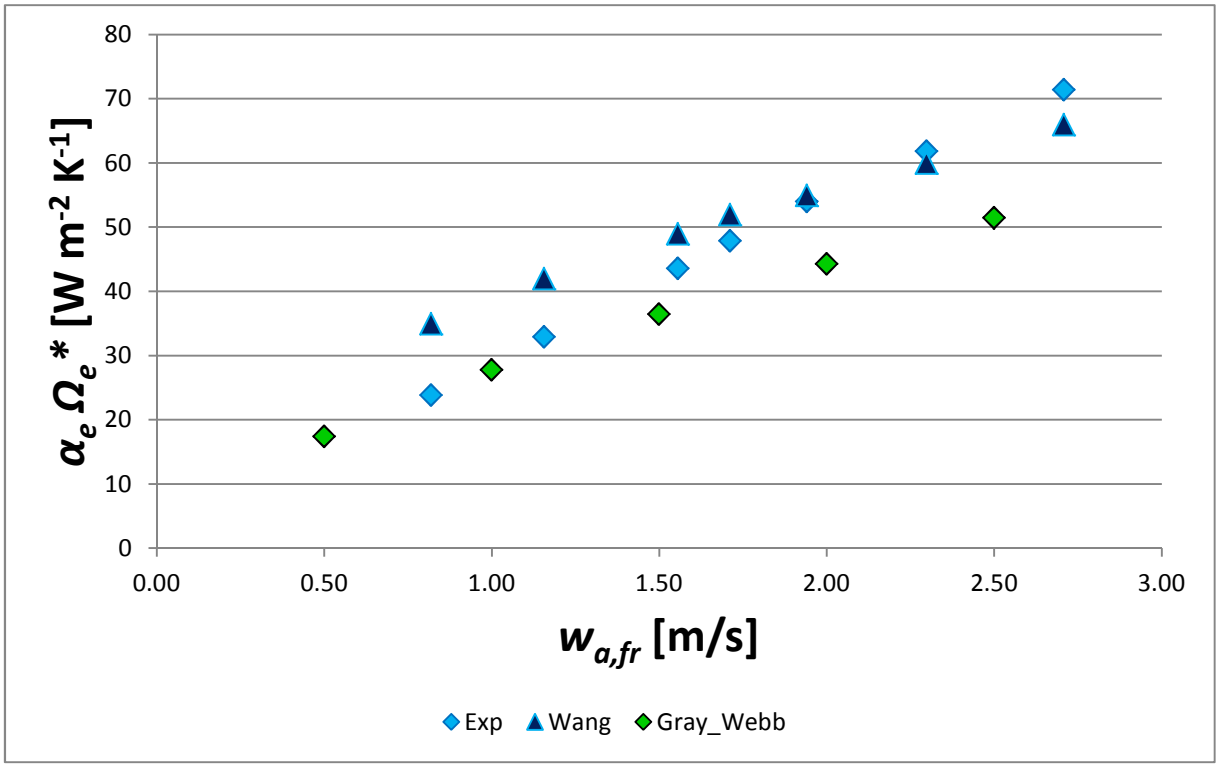

Fig. 6.4 Experimental results and literature comparison

As can be seen from Fig. 6.4, the Gray & Webb correlation presents good predictions of experimental results at air frontal velocities between 0.5 and 1.5 m/s; for higher air frontal velocities, this correlation underestimates the experimental data. On the other side, the Wang correlation shows values closed to the experimental ones for air frontal velocities higher than 1.5 m/s. Differences between experimental data and correlations values can be ascribed to several factors. At first, the Gray & Webb study is referred to an older kind of heat exchangers than the one investigated by Wang. Moreover, the Gray & Webb heat transfer correlation was obtained from a number of 16 samples having with an external diameter higher than the analyzed heat exchanger (9.52 mm). Due to this difference, the correlation range of validity is not fully respected. On the other side, the Wang heat transfer correlation was obtained from a number of 76 samples and its range of validation is fulfilled by the investigated sample. In the end, other differences between experimental data and correlation results can be caused by the contact resistance and the data reduction method.

6.5 Tests in dehumidification conditions and model comparison

Tests in dehumidification conditions were carried out according to the procedure described in Section 6.1.3; inlet temperatures and flow rates of the two fluids were kept constant. The relative discrepancy between air and water heat transfer rates was defined as follows (Eq. 6.13):

$$\delta = \frac{|(Q_a - Q_{diss}) - (Q_w + Q_{dr})|}{Q_{m,w}} \tag{6.13}$$

This relative difference presented an average value equal or lower than ±8%. In Eq. 6.13, $Q_{m,w}$ is the arithmetic mean between the two numerator terms in brackets. Results at different air inlet absolute (relative) humidity are shown in Fig. 6.5 and summarized in Table 6.6, where the sensible heat transfer is reported.

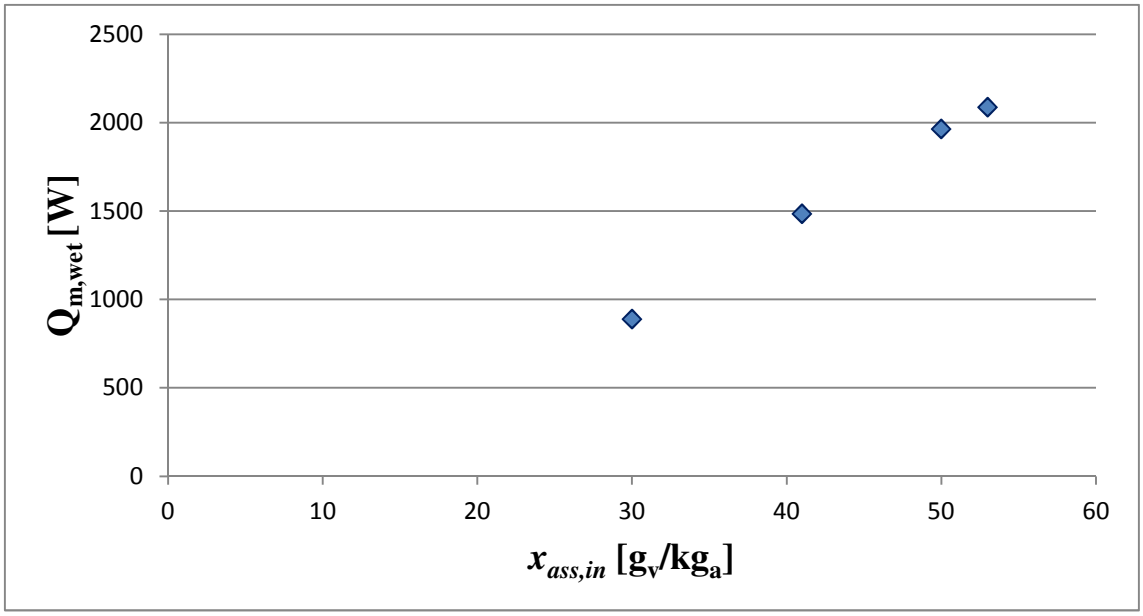

Fig. 6.5 Heat transfer rates at different air inlet absolute humidity

Table 6.6

Dehumidification tests results

RH_{in} [%]	$x_{ass,in}$ [g_v/kg_a]	Q_{sens} [W]	Q_{tot} [W]
54	30	768	919
70	41	606	1496
88	50	434	2020
92	53	389	2143

As can be seen from Fig. 6.5, the heat transfer rate increases with the increase of the air inlet absolute (relative) humidity, because the latent heat transfer rate is promoted by a more relevant concentration difference of humidity between the incoming air and the external tube surface.

6.5.1 Experimental and LMED method results comparison

Experimental results in dehumidification conditions represented in Fig. 6.5 were compared with numerical results obtained with a simulation model implemented in a commercial software, which is based on a nodal analysis [7]. With this method, the finned coil is divided into several elements, Each element, or node, is identified through an index. The air and coolant circuits are defined by two arrays referred to the nodes. The calculation procedure follows an iterative method. The first iteration begins with the assumption that, for each node, the air inlet temperature is equal to the one of the first tube row. Then, every node is solved for heat transfer and coolant pressure variation. The procedure begins from the refrigerant outlet nodes where the boundary conditions are defined and continues from one node to the previous one backwards the coolant flow. The outlet air temperature of each node is used as inlet to the following one. After several iterations, the method converges toward the solution. In presence of latent heat transfer, the adopted approach is proposed by Threlkeld [8], i.e. a log-mean enthalpy difference (LMED) method for calculating the total heat transfer rate, as expressed in Eq. 6.14:

$$Q_{m,w} = U_w \cdot A_e \cdot \Delta h_{ml} \tag{6.14}$$

In Eq. 6.14, U_w is the overall heat transfer coefficient in dehumidification conditions, A_e is the external heat transfer area and Δh_{ml} is defined as follows:

$$\Delta h_{ml} = \frac{(h_{a,in} - h_{a,s2}) - (h_{a,out} - h_{a,s1})}{\ln\left(\frac{h_{a,in} - h_{a,s2}}{h_{a,out} - h_{a,s1}}\right)} \tag{6.15}$$

In Eq. 6.15, $h_{a,s2}$ and $h_{a,s1}$ are, respectively, the enthalpy of saturated air at coolant outlet and inlet temperatures. The comparison between experimental and simulation results at different air inlet absolute humidity is represented in Table 6.7.

Table 6.7

Experimental vs. LMED model results

RH_{in} [%]	$x_{ass,in}$ [g_v/kg_a]	Q_{exp} [W]	Q_{mod} [W]	Deviation [%]
54	30	919	967	-5
70	41	1496	1274	17
88	50	2020	1624	24
92	53	2143	1701	26

As can be seen from Table 6.7, the model shows a good prediction of the experimental results only for tests with inlet absolute humidity up to 30 g_v/kg_a. For tests at higher inlet absolute humidity, the model underestimates the total heat transfer rate than the experimental ones. This difference is highlighted in Fig. 6.6:

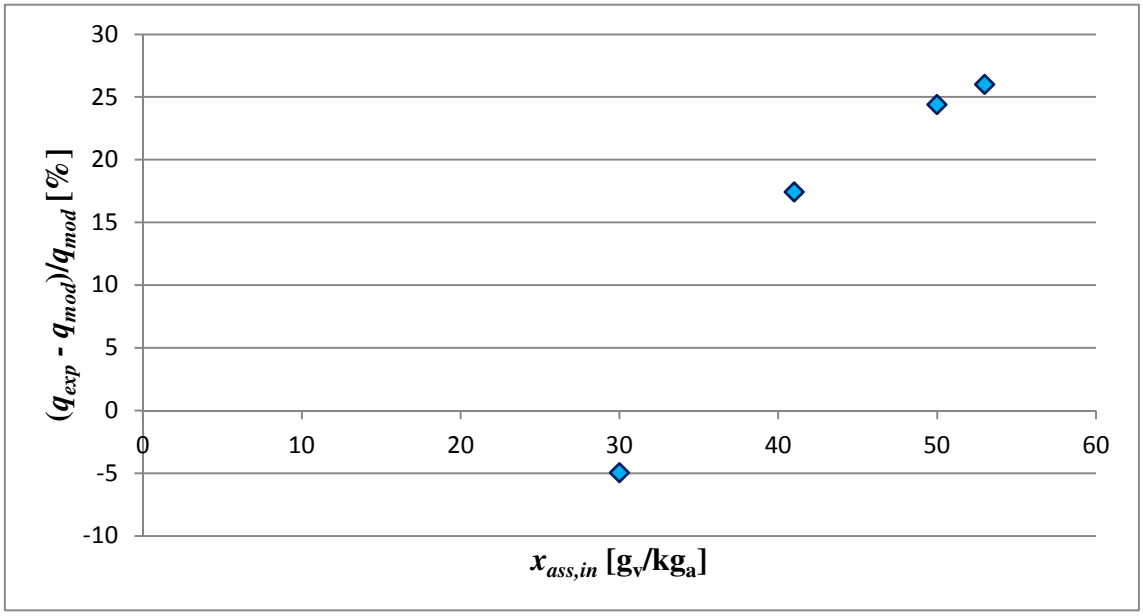

Fig. 6.6 Comparison between experimental and LMED results

As can be seen from Fig. 6.6, the relative discrepancy from model and experimental results increases with the increase of the air inlet absolute humidity. For tests with inlet absolute humidity higher than 30 g_v/kg_a, the relative difference presented values from 15% up to 26%. Same results of relative difference were obtained applying the LMED method to the overall heat exchanger, considering constant the properties of the fluids. In order to investigate these high values of relative discrepancy, a check of the model hypothesis was carried out. The LMED method was developed in order to analyze the simultaneous heat and mass transfer phenomena in dehumidification conditions. Eq. 6.14 has been obtained considering the analogy of heat and mass transfer, thus assuming a unit value of the Lewis Factor. The Lewis Factor is defined as follows in Eq. 6.16:

$$\frac{\alpha_e}{h_m \cdot c_{p,a}} = Le^{2/3} \tag{6.16}$$

where α_e is the air side heat transfer coefficient [W m^{-2} K^{-1}], $c_{p,a}$ is the air specific heat at constant pressure [J kg^{-1} K^{-1}] and h_m is the mass transfer coefficient [kg m^{-2} s^{-1}]. However, some studies in typical air conditioning conditions have suggested that the Lewis Factor may be deviated from being one, mainly due to the mass transfer coefficient value. Experimental results by Hong [9] indicated a value of the Lewis Factor between 0.7 and 1.1. Seshimo et al. [10] suggested a value of 1.1. Eckels and Rabas [11] also showed values of 0.75-1.0 in their tests on plain fin and tube heat exchangers. Wang et al. [12] pointed out that Lewis Factor ranged from 0.6 to 1. Due to these considerations, a calculation of the Lewis Factor for the previous tests described in Table 6.5 was been necessary. Pirompugd et al. [13] provided an equation for the evaluation of the Lewis Factor of a finned coil in dehumidification conditions, as explained in Eq. 6.17:

$$Le^{2/3} = 2.282 \cdot N^{0.2393} \cdot \left(\frac{s_f}{D_0}\right)^{(0.0239N+0.4332)} \cdot \left(\frac{A_e}{A_t}\right)^{(0.0321N+0.0747)} \cdot \mathrm{Re}_{D_0}^{\left(-0.01833N-0.1094\frac{s_f}{D_0}-0.0026\frac{p_t}{D_0}-0.03012\frac{p_r}{D_0}+0.0418\right)} \tag{6.17}$$

In Eq. 6.17, N is the number of the tube rows of the finned coil, s_f is the fin spacing, D_0 is the outside tube diameter, A_t is the outside tube area and p_t and p_r are, respectively, the tube and rank pitches. Applying Eq. 6.17 at the test conditions expressed in Table 6.1, a Lewis Factor of 0.5 was calculated for each tests. For this reason, the assumption of a unit Lewis Factor of the LMED method was not verified and an alternative dehumidification model was considered.

6.5.2 Modified LMED method (m-LMED)

An alternative dehumidification method was considered, developed and validated by Xia et al. [14]. This method is a modification of the LMED model and it includes the Lewis Factor value in the calculation of the overall heat transfer coefficient. The total heat transfer rate of the modified method (m-LMED) is expressed by Eq. 6.18:

$$Q_{m,w} = U_{w,M} \cdot A_e \cdot \Delta h_{ml} \cdot F \tag{6.18}$$

where $U_{w,M}$ is the modified overall heat transfer coefficient. An evaluation of $U_{w,M}$ can be expressed neglecting the conductive heat transfer resistances related to the condensate and the tube, as shown in Eq. 6.19:

$$U_{w,M} = \frac{1}{A_e} \cdot \left[\frac{b}{A_i \alpha_i} + \frac{c_{p,a}}{A_e \alpha_e \Omega_e^*} \cdot \left(1 - \frac{Le^{2/3} - 1}{Q_s / (Q_{m,w} - Q_s) + Le^{2/3}} \right)^{-1} \right]^{-1} \quad (6.19)$$

In Eq. 6.19, b is a linear coefficient relating the enthalpy of saturated humid air to dry-bulb air temperature, evaluated at the coolant inlet and outlet temperatures. The internal convective heat transfer coefficient is calculated with [3], while the external heat transfer coefficient and the heat transfer surface efficiency is derived from Table 6.4. The Lewis Factor is calculated with Eq. 6.17 and the heat transfer rates of the specific test are derived from Table 6.5. When the Lewis Factor is equal to unit, $U_{w,M}$ is equal to U_w and the m-LMED method is the same as the LMED method.

6.5.3 Experimental and m-LMED method comparison

The experimental results were then compared with the m-LMED method predictions. In Eq. 6.19, the internal heat transfer coefficient was calculated according to Gnielinski, while the air side heat transfer coefficient and the overall fin efficiency was derived from Eq. 6.12. The b coefficient was evaluated between the outlet and inlet coolant temperatures. The relative discrepancy between experimental and m-LMED model results is represented in Fig. 6.7:

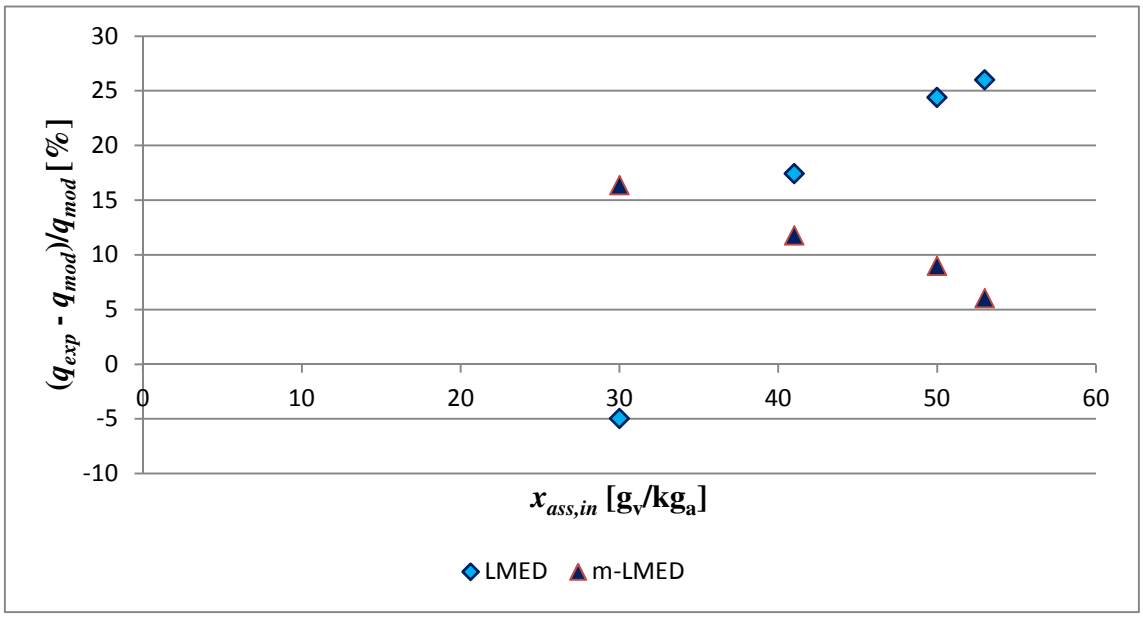

Fig. 6.7 Comparison between experimental and m-LMED results

As can be seen from Fig. 6.7, the relative discrepancy between experimental and m-LMED model results decreases with the increase of the air inlet absolute humidity. The relative difference decreases from about 16% up to 6% for the higher value of inlet absolute humidity achieved in the experimental tests. The comparison represented in Fig. 6.6 is also reported in Fig. 6.7. The different

trends obtained with the use of the two methods highlight the importance to consider the Lewis Factor value for achieving good model predictions.

6.6 Conclusions

Experimental tests in no dehumidification conditions were carried out on a plain fin heat exchanger in order to evaluate the air side heat transfer coefficient. A relation between the air side heat transfer coefficient, the surface efficiency and the air frontal velocity at the sample inlet was found. Further tests in dehumidification conditions were performed for comparing experimental results with a dehumidification model. At first, a log-mean enthalpy difference (LMED) method was considered for comparing the results. Good model predictions was found for tests with air inlet absolute humidity up to 30 g_v/kg_a; for higher values of this parameter, the relative difference between experimental and model results increased. The model assumption of a unit value of the Lewis Factor was not verified for tests with air inlet absolute humidity higher than 30 g_v/kg_a; a Lewis Factor equal to 0.5 was calculated. An alternative model was then considered, based on a modification of the previous log-mean enthalpy difference method (m-LMED). This model included the Lewis Factor value in the calculation of the overall heat transfer coefficient. For tests with air inlet absolute humidity higher than 30 g_v/kg_a, relative differences below 10% was found between experimental results and m-LMED predictions. The main finding of this activity was the awareness that LMED methods, successfully applied to heat exchangers under dehumidifying conditions typical of air conditioning (air inlet absolute humidity 10-20 g_v/kg_a), fail in predicting heat transfer rates when inlet specific humidity is higher than 30 g_v/kg_a. This means that modified LMED methods, taking into account the Lewis Factor, are required to properly simulate heat exchangers in heat pump tumble dryers.

6.7 References

[1] REFPROP 9.1, NIST Standard Reference Database

[2] JCGM 100:2008 “Evaluation of measurement data-Guide to the expression of uncertainty in measurement.

[3] Gnielinski V., Chapter Gb, VDI-Heat atlas, VDI Verlag, 1993.

[4] Wilson E.E., A basis of rational design of heat transfer apparatus, ASME Journal of Heat Transfer 37 (1915), 47-70.

[5] Gray D.L., Webb R.L., Heat transfer and friction correlations for plate finned-tube heat exchangers having plain fins, Heat transfer, Proceedings of the International Heat Transfer Conference 6 (1986), 2745-2750.

[6] Wang C.C., Chi K.Y., Chang C.J., Heat transfer and frictional characteristics of plain fin-and-tube heat exchanger, part II: Correlation, Int. J. of Heat and Mass Transfer 43 (2000), 2693-2700
[7] Casson V., Cecchinato L., Del Col D., Fornasieri E., Zilio C., An innvovative model for the simulation of finned coil evaporators, Heat transfer 4 (2002), 285-290.
[8] Threlkeld JL., Thermal Environmental Engineering, New York; Prenticc-Hall, Inc, 1970.
[9] Hong K., Fundamental characteristics of dehumidifying heat exchangers with and without wetting coating. Ph.D. Thesis, Department of mechanical engineering, the Pennsylvania State University, USA, 1996.
[10] Seshimo Y., Ogawa K., Marumoto K., Fujii M., Heat and mass transfer performances on plate fin and tube heat exchangers with dehumidification, Transactions JSME 54 (1988), 716-721.
[11] Eckels P.W., Rabas T.J., Dehumidification: on the correlation of wet and dry transport process in plate finned-tube heat exchangers, ASME J. of Heat Transfer 109 (1987), 575-582.
[12] Wang C.C., Chang C.T., Heat and mass transfer for plate fin-and-tube heat exchangers, with and without hydrophilic coating, Int. J. of heat and mass transfer 41 (1998), 3109-3120.
[13] Pirompugd W., Wang C.C., Wongwises S., Finite circular fin method for heat and mass transfer characteristics for plain fin-and-tube heat exchangers under fully and partially wet surface conditions, Int. J. of Heat and Mass Transfer 50 (2007), 552-565.
[14] Xia L., Chan M.Y., Deng S.M., Xu X.G., A modified logarithmic mean enthalpy difference (LMED) method for evaluating the total heat transfer rate of a wet cooling coil under both unit and non-unit Lewis Factors, Int. J. of Therm. Sci. 48 (2009), 2159-2164.

7 Experimental investigation of air dehumidification in heat exchangers with different fin coatings

7.1 Experimental methods

7.1.1 Test samples

An experimental study was carried out for analyzing the impact of fin coatings on heat exchanger behaviour in dehumidification processes. The same commercial evaporator, currently used in heat pump tumble dryers, was considered in this investigation. The evaporator geometrical characteristics are summarized in Table 7.1.

Table 7.1

Test samples geometrical characteristics

Length [mm]	234
Width [mm]	88
Height [mm]	155
Tubes arrangement	Staggered
N° rows	4
N° tubes per row	6
Fin pitch [mm]	2
Rows pitch [mm]	21.5
Tubes pitch [mm]	25
External diameter [mm]	9.52
Fin type	Wavy
N° fins	117
Tube thickness [mm]	0.711
Fin thickness [mm]	0.11

Three test evaporator samples, having the same geometrical characteristics but treated with different fin coatings, were investigated in this analysis. One sample is characterized by fins of untreated aluminium and it considered the baseline of the study. The other two heat evaporators are respectively treated with a hydrophilic coating and a hydrophobic one. These two treatment are currently available on the market and their wettability has been characterized in Section 4. Similarly in Section 6.4, the behaviour of each sample under dry conditions was investigated, as explained in Appendix B.

7.1.2 Test procedure

In the test rig, experimental tests were carried out in order to reproduce the air conditions at the tumble dryer evaporator inlet. In a heat pump tumble dryer (HPTD), the hot and humid air exiting from the drum is sent to the heat pump evaporator for the dehumidification process. The inlet air conditions at the evaporator change along the working cycle of the tumble dryer, that typically lasts for two hours and a half. In Fig. 7.1 and Fig. 7.2, the typical temperature and relative humidity profiles at the evaporator inlet of a heat pump tumble dryer are sketched.

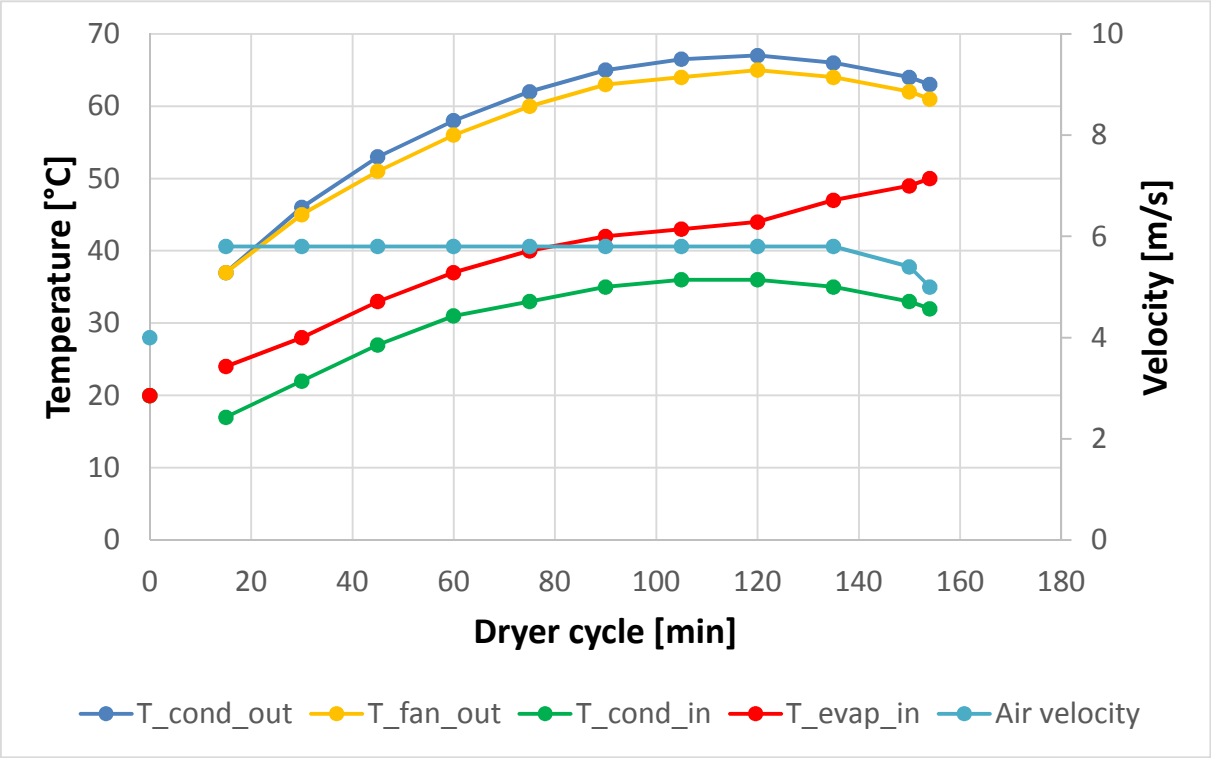

Fig. 7.1 Air temperature at the evaporator inlet (red line)

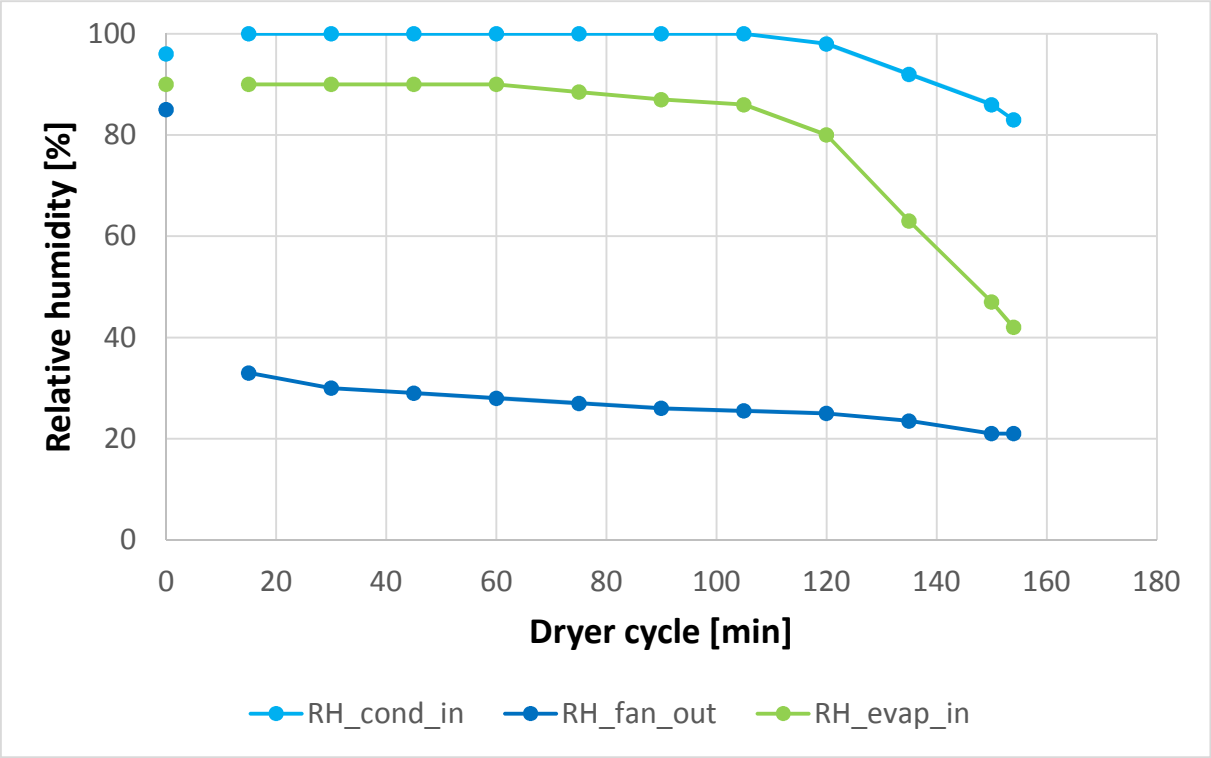

Fig. 7.2 Air relative humidity at the evaporator inlet (green line)

The volumetric air flow rate also changes along the cycle, from 250 m^3/h to 190 m^3/h in the last part. For the experimental tests, the inlet air parameters are represented according to the dry-bulb temperature and the absolute humidity in a t-x graph, shown in Fig. 7.3.

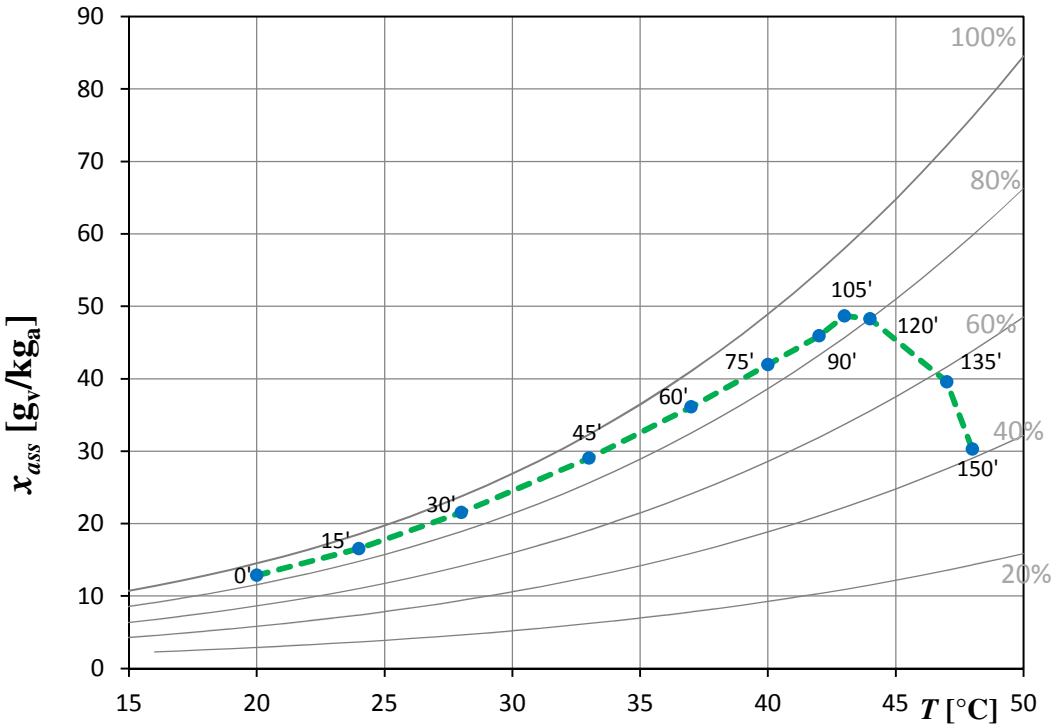

Fig. 7.3 Air conditions at evaporator inlet

As can be seen by Fig. 7.3, the inlet air temperature always increases along the cycle, but the inlet absolute humidity reaches a maximum value after about two hours. In the first hour of the cycle, the relative humidity reaches values of 90% or more due to a high evaporation rate in the drum. Then, the relative humidity slightly decreases up to 80% in the next hour.; at the same time, the inlet absolute humidity presents values over 40 g_v/kg_a and reaches a maximum close to 50 g_v/kg_a. These values are abnormally higher than the ones reach in air conditioning and their impact on the heat exchanger performance has been described in Section 6. In the last part of the cycle, the relative humidity falls up to 40% due to the low evaporation rate in the drum. In order to reproduce the working cycle conditions, ten representative points were considered, equally spaced in time, as shown in Fig. 7.3. Each point is uniquely characterized by single inlet values of temperature and absolute humidity. For each point, the water inlet temperature was fixed at the same value of the refrigerant one in the tumble dryer, while the water volumetric flow rate was also kept constant to 180 l/h for all the tests. The water mass flow was divided into two circuits to minimize the temperature difference between inlet and outlet, thus trying to be as closer as possible to isothermal conditions, which occur as far as the refrigerant is evaporating in commercial HPTD. This arrangement allowed to have a Reynolds Number of 4000 in each circuit. The procedure of a single test follows the same steps described in Section 6.2.3. For each point, the air and water inlet conditions were reproduced at the inlet of the test section in the apparatus. After the recording of 30 minutes, an evaluation of the retained water on the test sample was performed. The power of the electrical heaters, the steam generators, the chiller pump and the centrifugal fan was cut off. Then, the test section was opened from the top cover and a compressed air gun was used for obtaining a complete cleaning of the heat exchanger surface. The retained water felt down into the receiver located on the balance. The weight difference measured with the balance between the start and the end of the complete cleaning operation led to an evaluation of the retained water for each sample at a specific investigated point. Each test was performed twice in order to reduce the uncertainty in the measure value.

7.2 Data reduction

The thermal balance at the test section, shown in Eq. 6.7, was considered for the analysis of the experimental data. The air heat transfer rate was calculated as expressed by Eq. 6.6. In this study, the water flow was arranged in two parallel circuits. At each inlet and outlet, a thermocouple was inserted for measuring the coolant temperature. The water mass flow rate was equally divided between the circuits. So, the water heat transfer rate was calculated as explained in Eq. 7.1:

$$Q_w = \frac{\dot{m}_w}{2} \cdot c_{p,w} \cdot (t_{w,out,1} + t_{w,out,2} - t_{w,in,1} - t_{w,in,2}) \quad (7.1)$$

The thermal dispersion losses to the surroundings and the heat transfer rate related to the water condensate were calculated as expressed by Eq. 6.8 and Eq. 6.9.

7.3 Experimental results at a fixed air volumetric flow rate

An overview of the experimental tests carried out for each sample is shown in Table 7.2.

Table 7.2

Air and water test conditions

Dryer cycle [min]	$Q_{v,a}$ [m^3/h]	$T_{a,in}$ [°C]	$x_{ass,in}$ [g$_v$/kg$_a$]	$Q_{v,w}$ [l/h]	$T_{w,in}$ [°C]
15	250	24	17	180	12
30	250	28	21	180	16
45	250	33	30	180	18
60	250	37	36	180	21
75	200	40	42	180	23
75	250	40	42	180	23
75	300	40	42	180	23
90	200	42	46	180	24
90	250	42	46	180	24
90	300	42	46	180	24
105	200	43	49	180	25
105	250	43	49	180	25
105	300	43	49	180	25
120	200	44	48	180	25
120	250	44	48	180	25
120	300	44	48	180	25
135	250	47	40	180	25
150	250	48	30	180	24

A first experimental investigation was performed in steady state conditions at a fixed air volumetric flow rate equal to 250 m^3/h. A comparison according to the total heat transfer rate, the drain rate and the retained water weight was carried out between the three test samples. In Fig. 7.4, the heat transfer rate of the coolant side of the three samples is represented for all the investigated points of the dryer cycle.

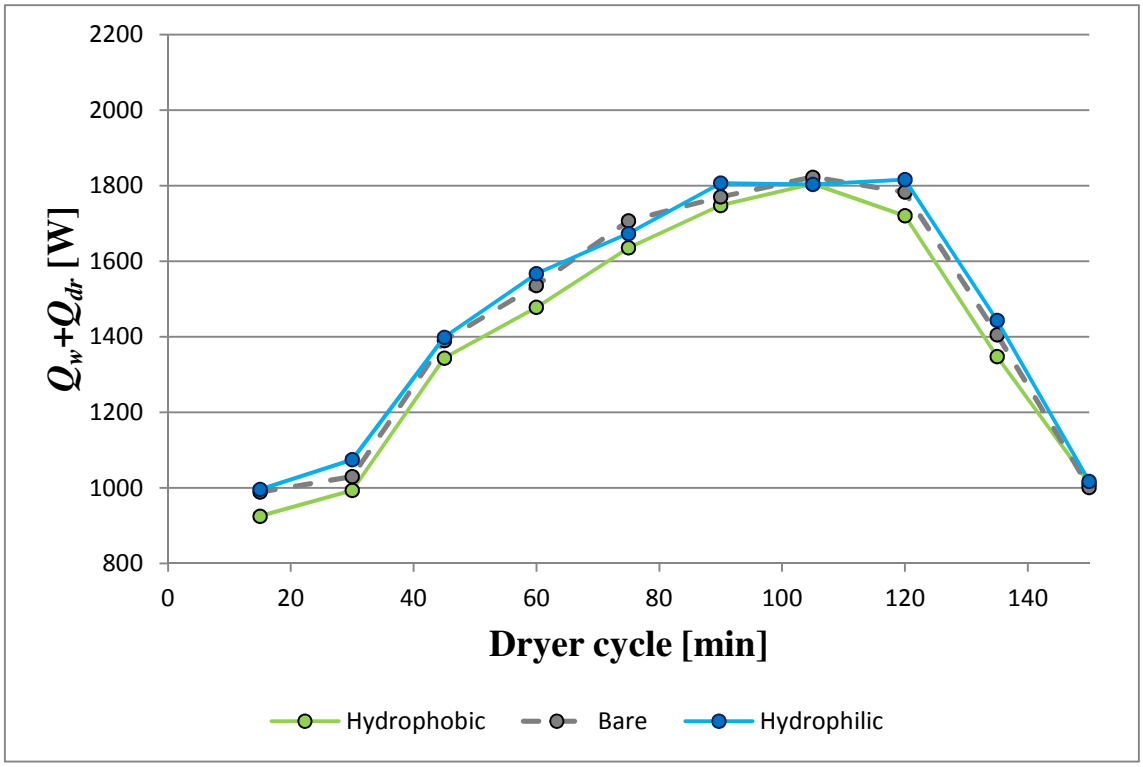

Fig. 7.4 Water side heat transfer rate at 250 m^3/h

As can be seen from Fig. 7.4, for all the samples, the heat transfer rates increases in the first six representative points and reaches a maximum at point 105'. Then, the sum decreases for the last three points. The heat transfer rates of the untreated and the hydrophilic samples show similar values for the entire cycle. Otherwise, the heat transfer rate of the hydrophobic samples presents the lowest values for all the points. This behaviour is also highlighted in Fig. 7.5, where the air side heat transfer rates of the test samples for all the investigated points are shown. In Fig. 7.5, the air side heat transfer rates of the three samples reflect the trend of Fig. 7.4, even though in a more irregular way. As in Fig. 7.4, the heat transfer rates of the hydrophobic sample present lower values than the ones of the other two samples for the entire cycle.

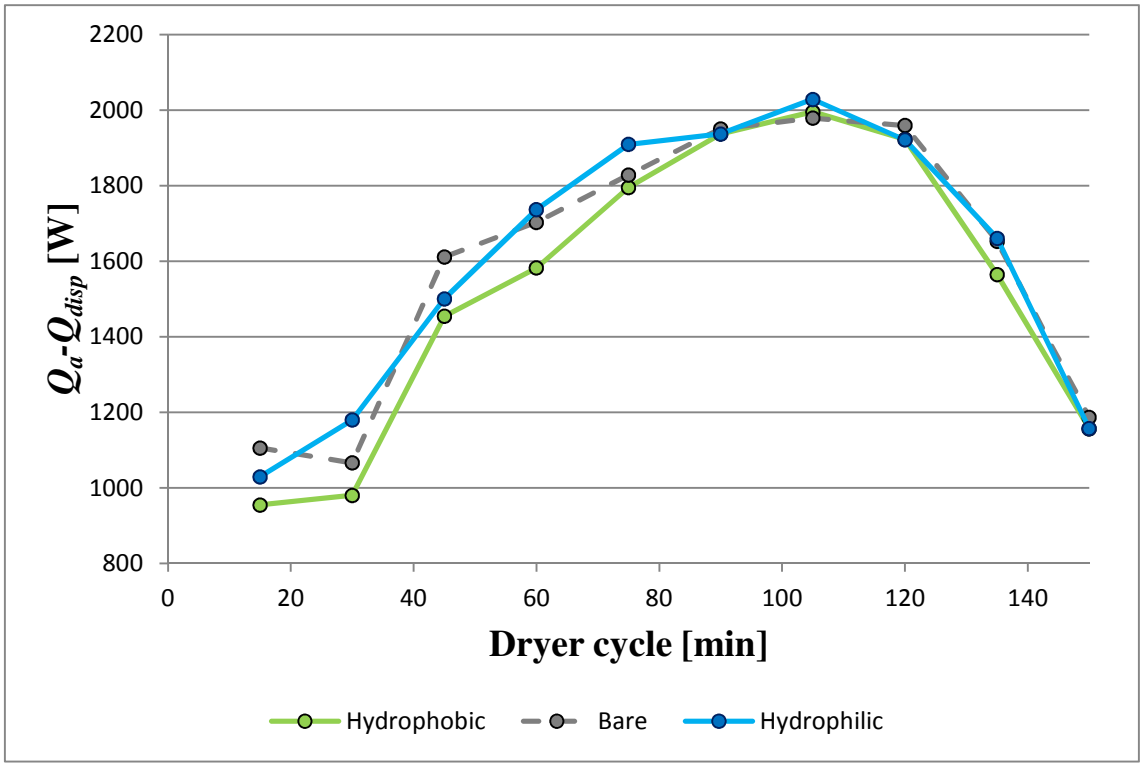

Fig. 7.5 Air side heat transfer rate at 250 m^3/h

A comparison according to the steady state drain rate of the condensate water as a function of the dryer cycle point is represented in Fig. 7.6.

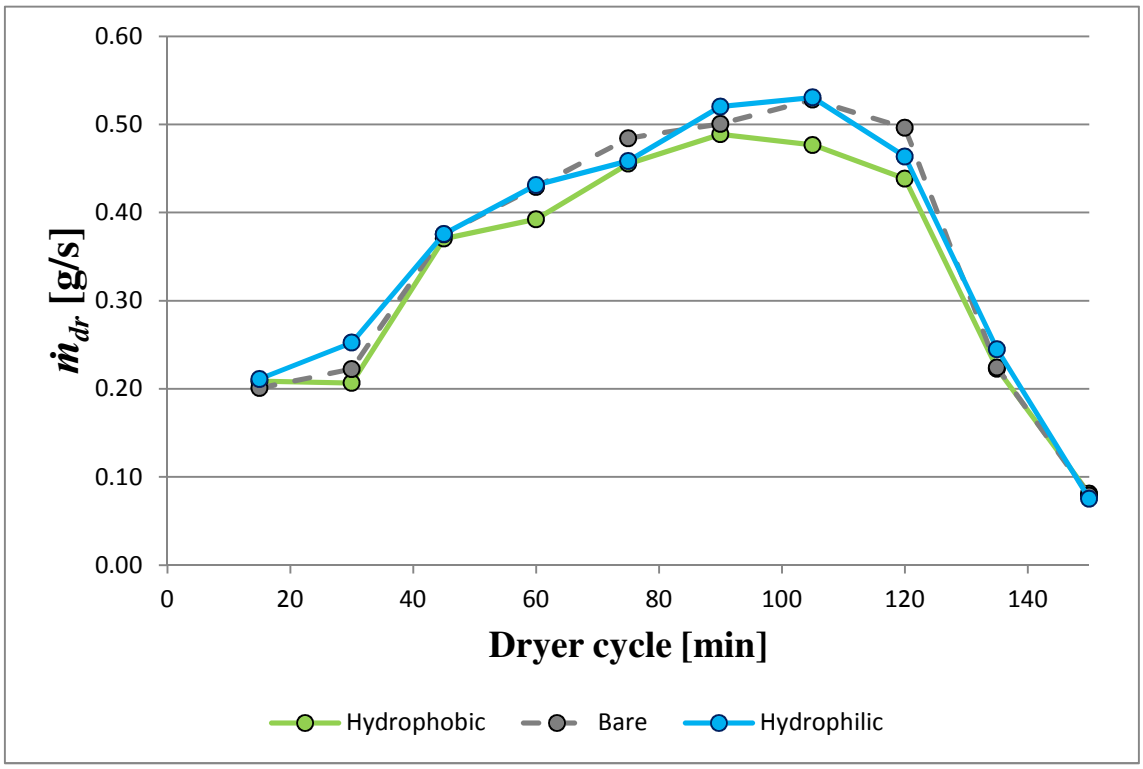

Fig. 7.6 Drain rate of the condensate water at 250 m^3/h

As can be seen from Fig. 7.6, for all the samples, the drain rate increases up to point 105' and reaches a maximum; then, in the last points, the drain rate monotonously decreases. The drain rate values of the hydrophobic sample are the lowest for all the points. On the other hand. the hydrophilic and the untreated samples present similar values of drain rate for all the points. This behaviour according to the drain rate between the three samples reflects the previous differences found in the heat transfer rate comparison. At last, the retained water weight on each test sample is shown in Fig. 7.7.

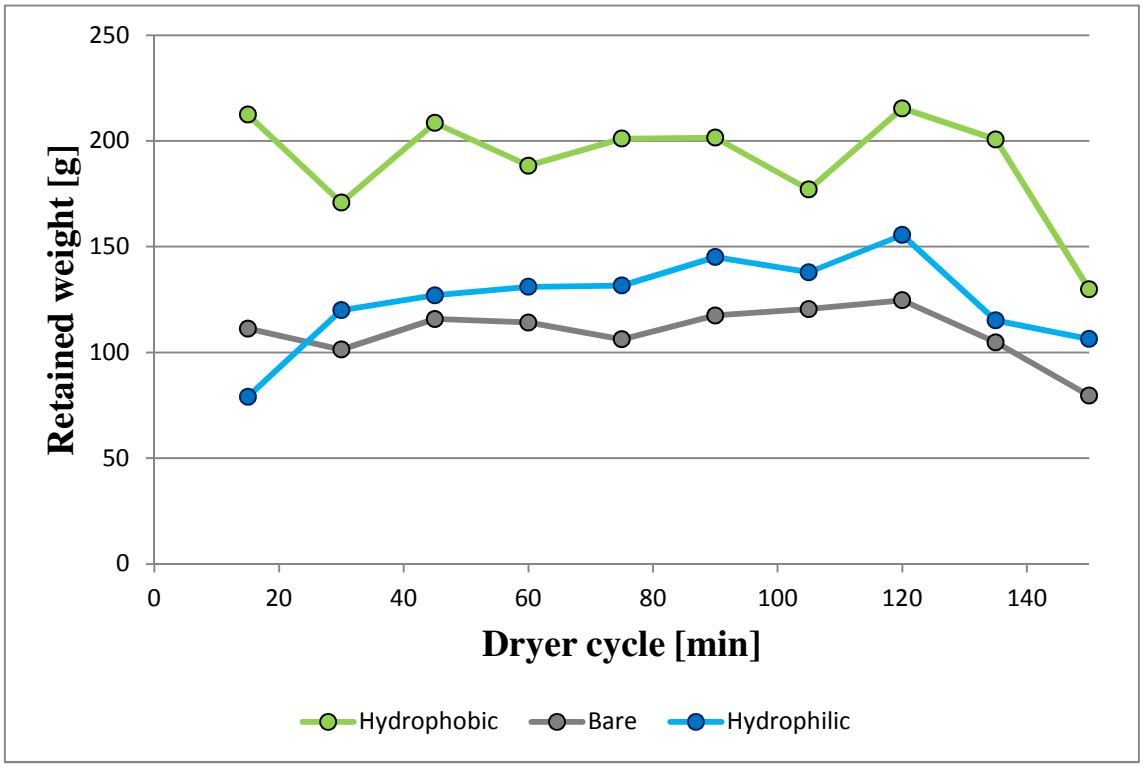

Fig. 7.7 Water retained weight at 250 m^3/h

The hydrophobic sample presents the higher retained water weight for all the investigated points, reaching values of about 200 g. The hydrophilic and the untreated retained water weights show similar values in the range of 100 and 150 g. The hydrophilic sample presents slightly higher value than the untreated one due to its higher wettability that tends to improve the filmwise condensation. On the other side, the high values of the retained water weight on the hydrophobic sample explain the lower ones in terms of heat transfer rate. The low wettability of the hydrophobic surface promotes dropwise condensation. Droplets grow up until the gravity force overcomes the retention force due to the surface tension and causes the droplet fall. On the same fin surface side, the droplet fall can be promotes by the coalescence between two droplets. However, the coalescence process can occur between two droplet of two adjacent fins if the fin pitch is small enough. The two droplets do not fully merge in an unique one, but they remain partially jointed, forming a sort of

bridge. This phenomenon leads to a decrease of the air flow cross area and of the heat transfer surface. A reduction of the air flow cross area leads to an increase of the pressure drops though the heat exchanger, while a reduction of the heat transfer area leads to a decrease of the heat transfer rate. This effect was also highlighted by Liu [1].

7.4 Experimental results at different air volumetric flow rates

After tests at a fixed air volumetric flow rate, further experimental investigations were carried out at different volumetric flow rates in steady state conditions. The air flow was adjusted by acting on the fan potentiometer. Two air volumetric flow rates were considered in this analysis: 200 m^3/h and 300 m^3/h. Besides, four representative points of the dryer working cycle of Fig. 7.3 were investigated. Points at 75', 90', 105', 120' were considered due to their high values of temperature (more than 40 °C) and absolute humidity (more than 40 g_v/kg_a). A comparison according to the total heat transfer rate, the drain rate and the retained water weight was carried out between the three test samples. In Fig. 7.8 and Fig. 7.9, the sum of the heat transfer rates of the coolant side and the water condensate of the three samples at 200 m^3/h and 300 m^3/h are represented.

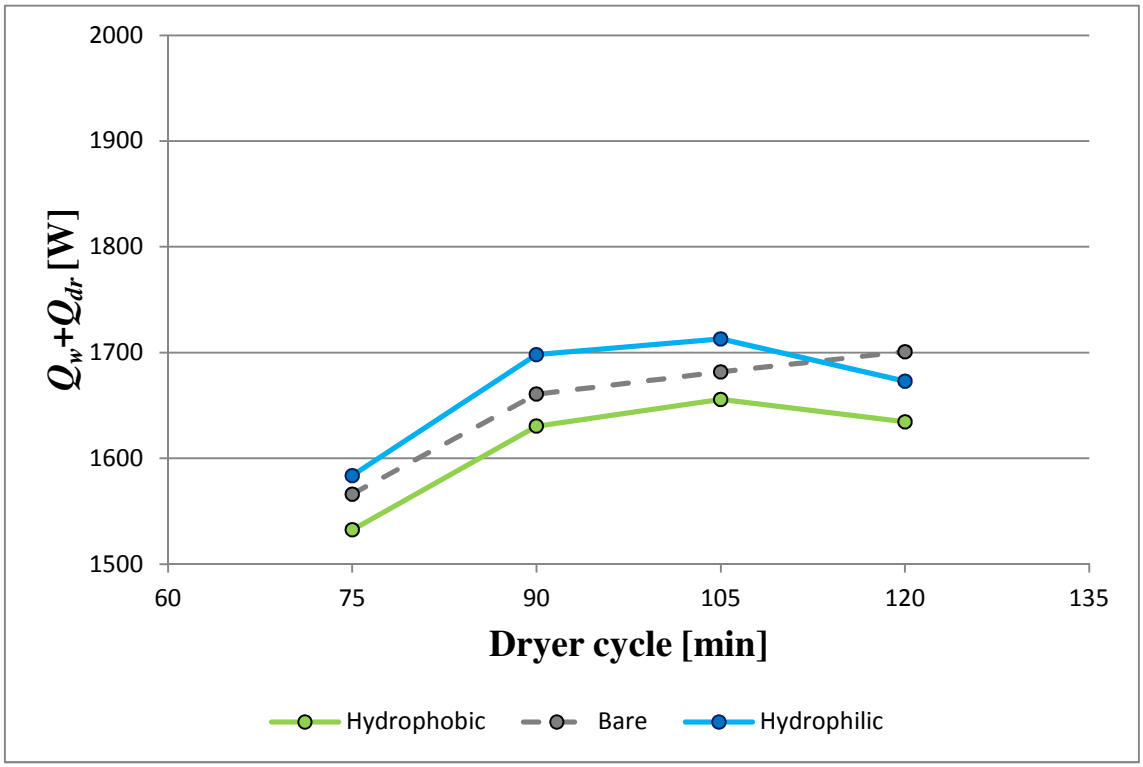

Fig. 7.8 Water side heat transfer rate at 200 m^3/h

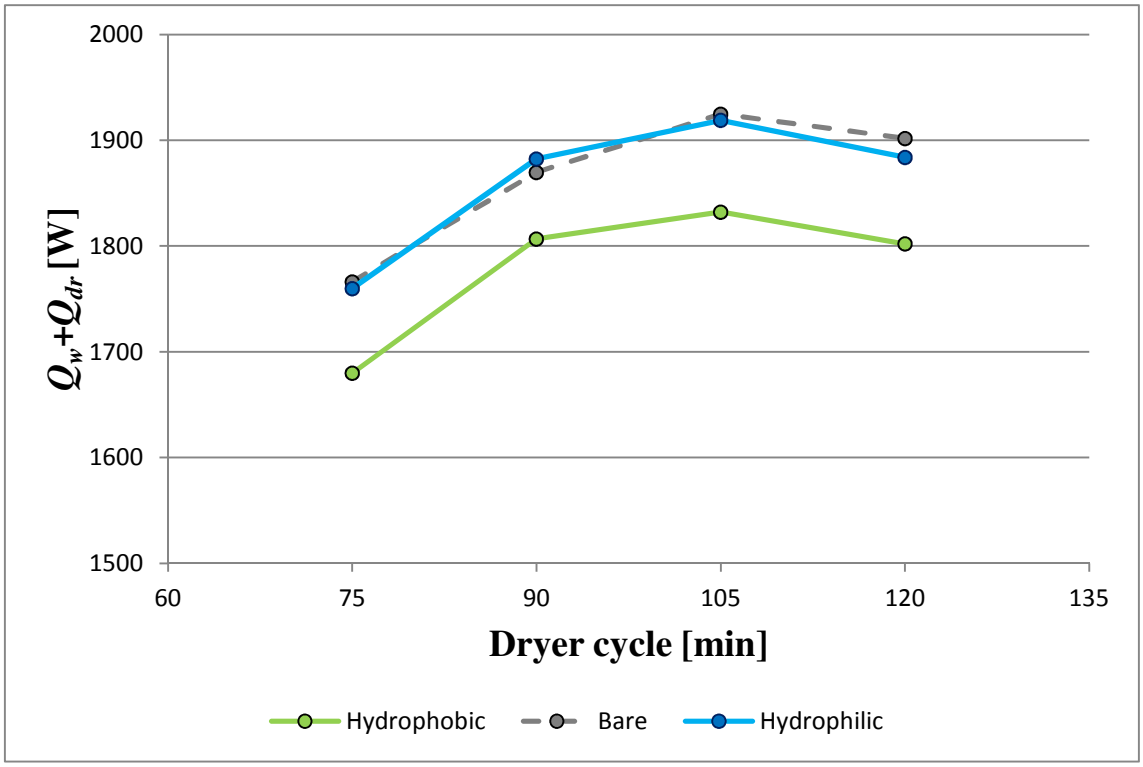

Fig. 7.9 Water side heat transfer rate at 300 m^3/h

As can be seen from Fig. 7.8 and Fig. 7.9, the heat transfer rates of the three samples increases up to point 105' where it reaches a maximum, except for the untreated sample at 200 m^3/h. The hydrophobic sample presents the lowest values of heat transfer rates at both air volumetric flow rates. The hydrophilic and the untreated samples shows similar values of heat transfer rates at both air volumetric flow rates. This behaviour is equal to the one found at 250 m^3/h; the changing of the air volumetric flow rate does not produce an effect in the heat transfer rate comparison results. In Fig. 7.10 and in Fig. 7.11, experimental results related to the drain rate of the condensate water are shown at the two different air volumetric flow rates.

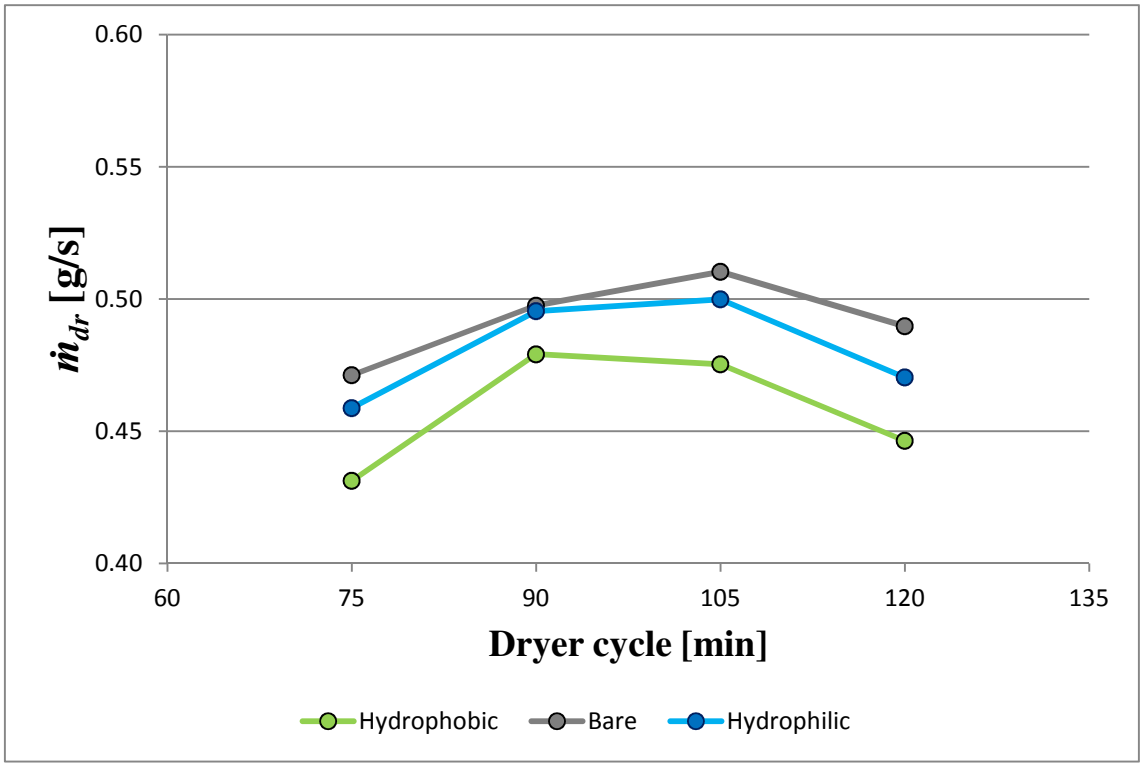

Fig. 7.10 Drain rate of the condensate water at 200 m^3/h

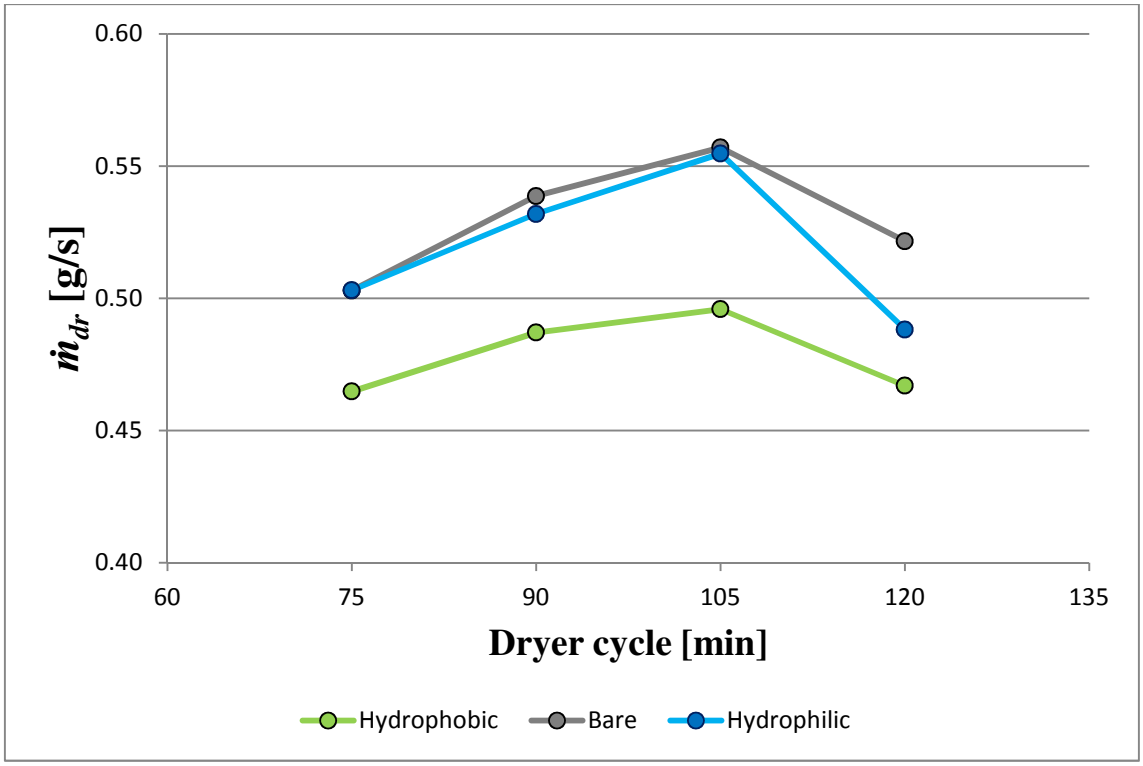

Fig. 7.11 Drain rate of the condensate water at 300 m^3/h

As can be seen from Fig. 7.10 and Fig. 7.11, the drain rate of the three samples increases up to point 105' where it reaches a maximum, except for the hydrophobic sample at 200 m^3/h; however, the variation between the drain rate at 90' and 105' is very limited. The hydrophilic and the untreated samples present similar values of drain rate for all the investigated points. On the other hand, the

hydrophobic heat exchanger shows the lowest values of drain rate at both air volumetric flow rates. This trends are similar to the one found in tests at 250 m^3/h, showing no relevant differences in the behaviour of the three test samples. At last, the retained water weight at 200 m^3/h and at 300 m^3/h is represented in Fig. 7.12 and Fig. 7.13.

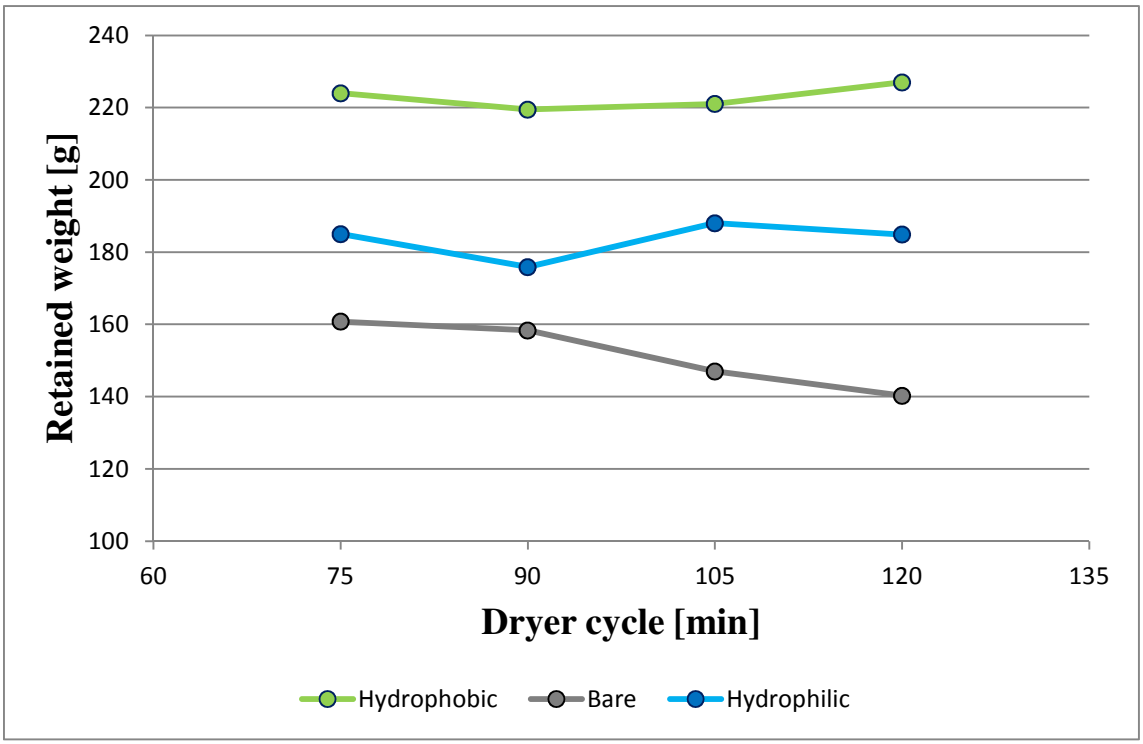

Fig. 7.12 Retained water weight at 200 m^3/h

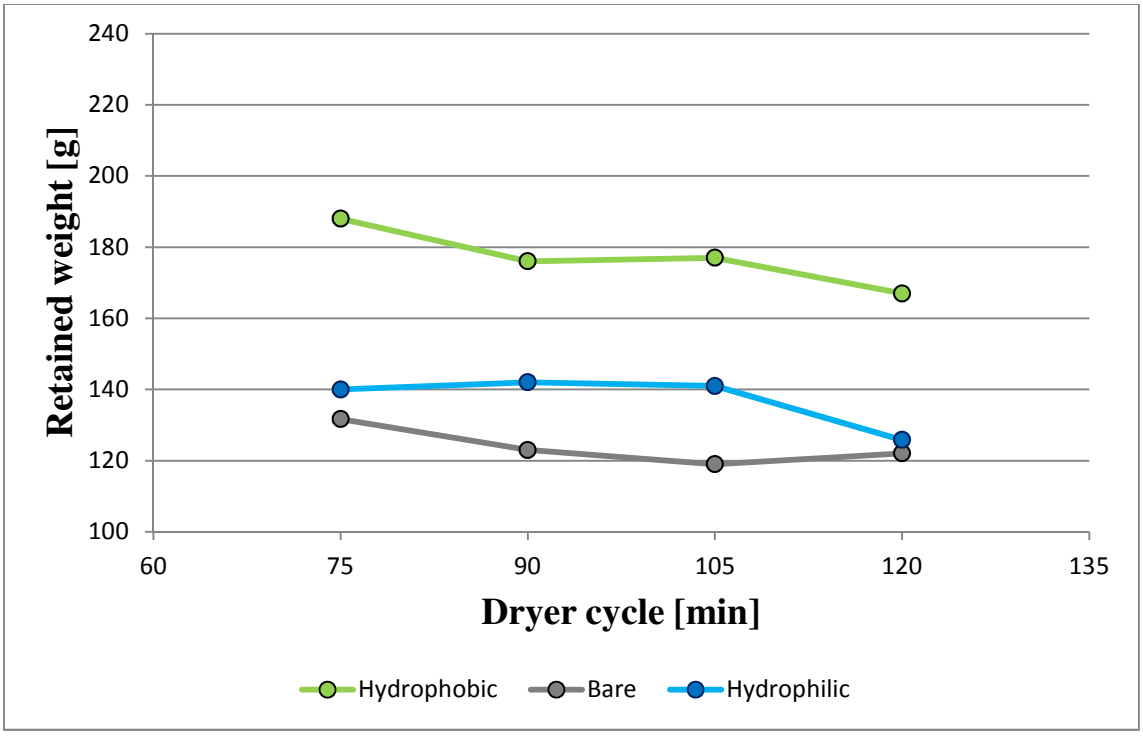

Fig. 7.13 Retained water weight at 300 m^3/h

As can be seen from Fig. 7.12 and Fig. 7.13, the hydrophobic sample presents the highest values of retained eater weight for all the points. At 200 m^3/h, the weight reaches values of about 220 g. The hydrophilic and the untreated samples shows similar values for all the points, always lower than the ones of the hydrophobic sample. This behaviour was previously shown for tests at 250 m^3/h; also in this comparison no relevant changing was noticed.

7.5 Conclusions

An experimental investigation on the impact of fin commercial coatings into heat exchanger behaviour under dehumidification conditions was carried out. The air conditions at the evaporator inlet of the tumble dryer were reproduced in the tests. These conditions are characterized by high values of temperature and absolute humidity (higher than 40 g_v/kg_a). Three test samples of the same supplier were considered in this study. One sample presented fins of untreated aluminium, while the other two were respectively treated with a hydrophilic and a hydrophobic coating. Comparisons were carried out according to the total heat transfer rate, the drain rate and the retained water weight. Dehumidification tests were performed in steady state conditions at different air volumetric flow rates. The hydrophobic sample presented the lowest values of heat transfer rate and drain rate for all the investigated flow rates, but it showed the highest values of retained weight. On the other hand, the hydrophilic and the untreated samples showed similar values of heat transfer rate, drain rate and retained weight, highlighting no relevant difference between their behaviour in dehumidification conditions.

7.6 References

[1] Liping Liu, Effects of air-side surface wettability on the performance of dehumidifying heat exchangers, Ph.D. Thesis, University of Illinois, 2011.

8 Conclusions

The reduction of energy consumption of household appliances is one of the main goals of the Ecodesign Regulation, introduced in 2009. One of the main appliances that has an high impact into the domestic overall energy consumption is the tumble dryer. The main technology currently used in this appliance is the heat pump element that provides, at the same time, to the heating and to the dehumidification of the process air. Considering the air dehumidification process in the heat pump evaporator, the research activity focused on the experimental evaluation of finned coil evaporator performance under extreme conditions, like those occurring in this appliance and the impact of commercial fin coatings. Three test samples of the same commercial tumble dryer heat pump evaporator were considered for the study, provided by the same supplier. One sample presented fins of untreated aluminium and it was considered the baseline for the study. The other two samples were respectively treated with a hydrophilic and a hydrophobic coating. At first, a SEM analysis was carried out on a sample of each surface type. No information were obtained from each sample according to its chemical composition. Fin surface characterization was then carried out in an experimental apparatus for the measurement of the static and advancing contact angles, investigating into the wettability of each coating. Advancing contact angles of 76°, 97° and 7° were found respectively for the untreated, the hydrophobic and the hydrophilic sample. A wind tunnel was designed and built at the ITC-CNR of Padova for experimental investigations. The overall size of the experimental apparatus is about 6 m in length, 1.2 in width and 1.7 in height. The wind tunnel was equipped with the measurement instrumentation and other auxiliary elements for control purposes. First experimental tests were carried out for characterizing the heat exchanger behaviour in dry conditions. A relation between the air side heat transfer coefficient, the overall surface efficiency and the air frontal velocity was found for an untreated plain fins sample. Then, tests in dehumidification conditions were performed on the previous sample to compare experimental results to a dehumidification model. At first, a log-mean enthalpy difference (LMED) method, implemented in a commercial software, was considered for comparing the results. Good model predictions were found for tests with air inlet absolute humidity up to 30 g_v/kg_a; for higher values of this parameter, the relative difference between experimental and model results increased. The model assumption of a unit value of the Lewis Factor was not verified for tests with air inlet absolute humidity higher than 30 g_v/kg_a; a Lewis Factor equal to 0.5 was calculated. An alternative model was then considered, based on a modification of the previous log-mean enthalpy difference method (m-LMED). This model included the Lewis Factor value in the calculation of the overall heat transfer coefficient. For tests with air inlet absolute humidity higher than 30 g_v/kg_a, relative

differences below 10% was found between experimental results and m-LMED predictions. The core of the experimental activity investigated into the impact of fin coatings on heat exchanger performance in dehumidification conditions. At first, tests were performed in order to characterized their behaviour in dry conditions. A relation between the air side heat transfer coefficient, the overall surface efficiency and the frontal air velocity was found for each sample. After, tests in dehumidification conditions were carried out, characterized by values of air inlet absolute humidity higher than 40 g_v/kg_a. Studies concerning these high values of absolute humidity are not available in the open literature. Comparisons were carried out according to the total heat transfer rate, the drain rate and the retained weight. Dehumidification tests were performed in steady state conditions at different air volumetric flow rates in the range between 200 m^3/h and 300 m^3/h. The hydrophobic sample presented the lowest values of heat transfer rate and drain rate for all the investigated flow rates, but it showed the highest values of retained weight. On the other hand, the hydrophilic and the untreated samples showed similar values of heat transfer rate, drain rate and retained weight, highlighting no relevant difference between their behaviour in dehumidification conditions. The present results lay the foundations for future studies for the development of advanced simulation tools for the design of dehumidification heat exchangers for several domestic and industrial applications of drying systems.

Acknowledgments

First of all, I'm really grateful to my research team at the ITC-CNR of Padova: my co-supervisor Ing. Silvia Minetto, Ing. Antonio Rossetti and Ing. Sergio Marinetti. They helped and encouraged me many times during my Ph.D. and I gained a lot of knowledge from their valuable teachings.

I'm also thankful to my supervisor Prof. Claudio Zilio for guiding me with his advices and his support during my Ph.D..

I would like to thank Electrolux s.p.a. for the opportunity to carry out my research activity during the years; a particular thanks is addressed to Ing. Andrea Vanin for his dedication in following the project.

A special appreciation goes to Enrico Miorin and Silvia Deambrosis of ICMATE-CNR for helping me in one of the fundamental step of my research project. I'm also thankful to the ITC-CNR specialists Gabriele Minotto and Mauro Scattolini for their essential assistance during my experimental activity.

I'm really grateful to my parents, my sister and my fiancée Fabiana for their support throughout the years and their presence in hard times.

Appendix A - Experimental test description

As described in Section 6.2.3 and in Section 7.1.2, the procedure for tests in dehumidification conditions follows several steps. An overview of the development of a typical test is represented in Fig. A.1. The test was performed on the untreated heat exchanger and its evolution is highlighted in Fig. A.1 by the air mean temperature at the first grid, the absolute humidity at the test section inlet and the air mean temperature at the second grid. In Table A.1, the test conditions of the considered test are shown.

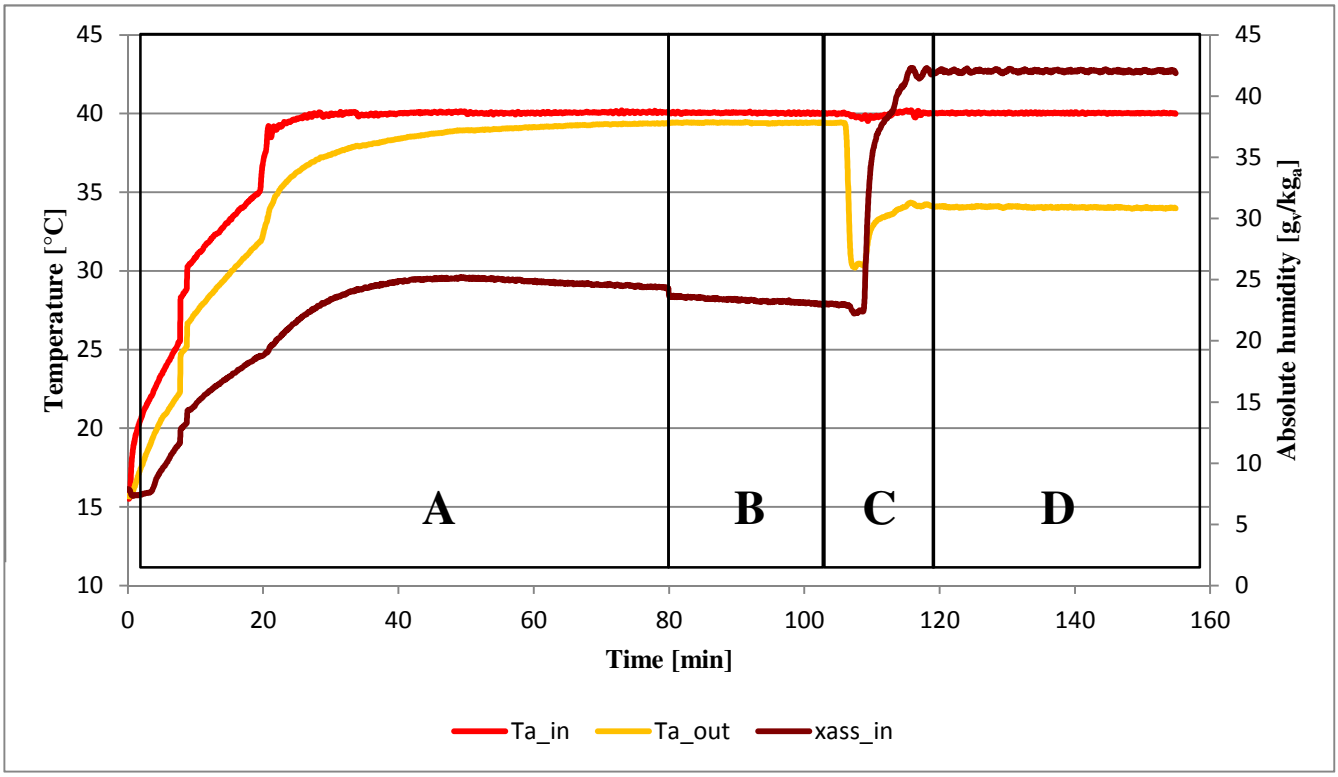

Fig. A.1 Experimental test overview

Table A.1

Test conditions of Fig. A.1

$T_{a,in}$ [°C]	$Q_{v,a}$ [m³/h]	$RH_{a,in}$ [%]	$x_{ass,in}$ [g_v/kg_a]	$T_{w,in}$ [°C]	$\dot{m}_w$ [g/s]	Re_w
40	250	87	42	23	50	7800

As can be seen from Fig. A.1, at the beginning of the test the temperature and humidity values in the wind tunnel are equal to the ambient ones. These low values (about 15°C and 7 g_v/kg_a) are typically present during the winter period. During the test first part (zone A), the main goal is to heat up the entire apparatus. The electrical heaters power is set close to the maximum for speeding

up the internal temperature increase. In this phase, the residual moisture of the previous test is vaporized into the air flow, reaching an equilibrium value (about 25 g_v/kg_a in Fig. A.1). After about 20 minutes, the controller of the electrical heaters is enabled and the output power is modulated in order to reach and keep the temperature set point value at the test section inlet. The wind tunnel reaches steady state conditions and the thermal losses to the ambient across the test section can be evaluated (zone B). Being the distance between the two grids equal to about 1 m, the difference of the two mean temperatures are in the range of 1-1.5 °C. As pointed out in Section 6.2.3, this acquisition lasts for about 15 minutes. After this step, the steam generators are turned on and the vapour flow is injected into the mixing chamber to increase the air absolute humidity (zone C). The steam flow contributes also to raise up the air temperature; so, the electrical heaters power is consequentially modulated by the controller. The steam generators controller is then activated, keeping the air absolute humidity at the inlet of the test section equal to the set point value. At the same time, the water flow begins to circulate into the heat exchanger, decreasing the external surface temperature below the air dew point and leading to condensation. The condensate water begins to fall into the bowl, where the electronic balance acquires its weight, as shown in Fig. A.2. When the temperature and humidity values remain constant to the set ones and the variation in time of the bowl weight follows a linear trend, the wind tunnel reaches steady state dehumidification conditions (zone D). In this final step, the acquisition lasts for about 30 minutes.

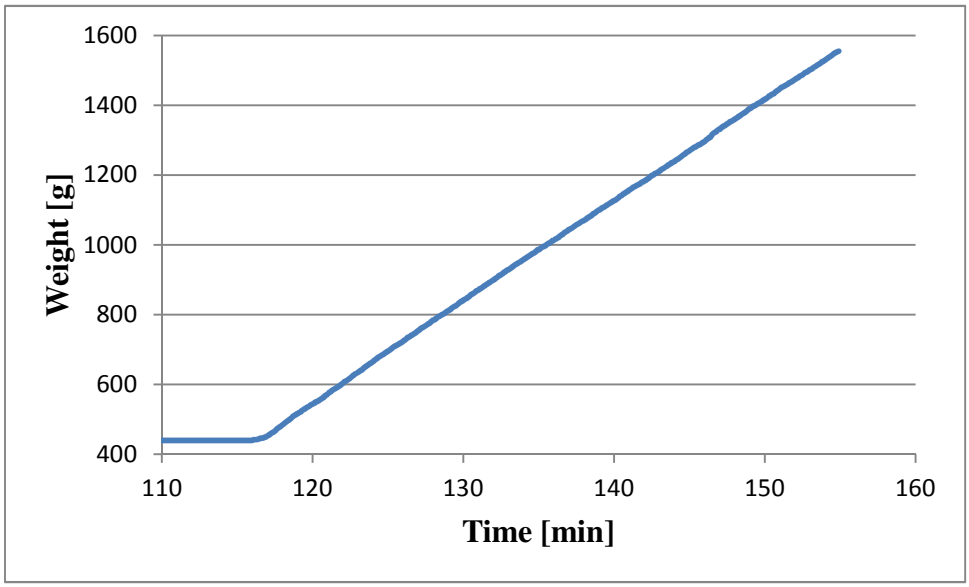

Fig. A.2 Bowl weight acquisition

Appendix B - Air side heat transfer coefficient evaluation for wavy fins heat exchanger

The air side heat transfer coefficient in dry conditions was evaluated for the three test samples analyzed in Section 7. This activity was undertaken in order to understand the impact of the fin coating in the sensible heat transfer process for the three heat exchangers. The same experimental procedure described in Section 6.2.2 for the bare plain fins heat exchanger was followed in this investigation. The tests working conditions of the air and water sides are reported in Table B.1.

Table B.1

Dry tests conditions

$T_{a,in}$ [°C]	$RH_{a,in}$ [%]	$w_{a,fr}$ [m/s]	$T_{w,in}$ [°C]	$\dot{m}_w$ [g/s]	Re_w
26	50	0.8-2.8	55	68	10600-10700

Tests were carried out at different air volumetric flow rates and with a constant coolant flow rate in turbulent conditions (Re_w > 10000). As pointed out in Section 6.4, a maximum relative discrepancy between air and water heat transfer rates ($|Q_a-Q_w|/Q_{m,dry}$) was also found for this tests equal to ±2%. A correlation between the air side heat transfer coefficient, the fin surface efficiency and the air frontal velocity was obtained for each sample. In Fig. B.1, the experimental results for each heat exchangers are shown.

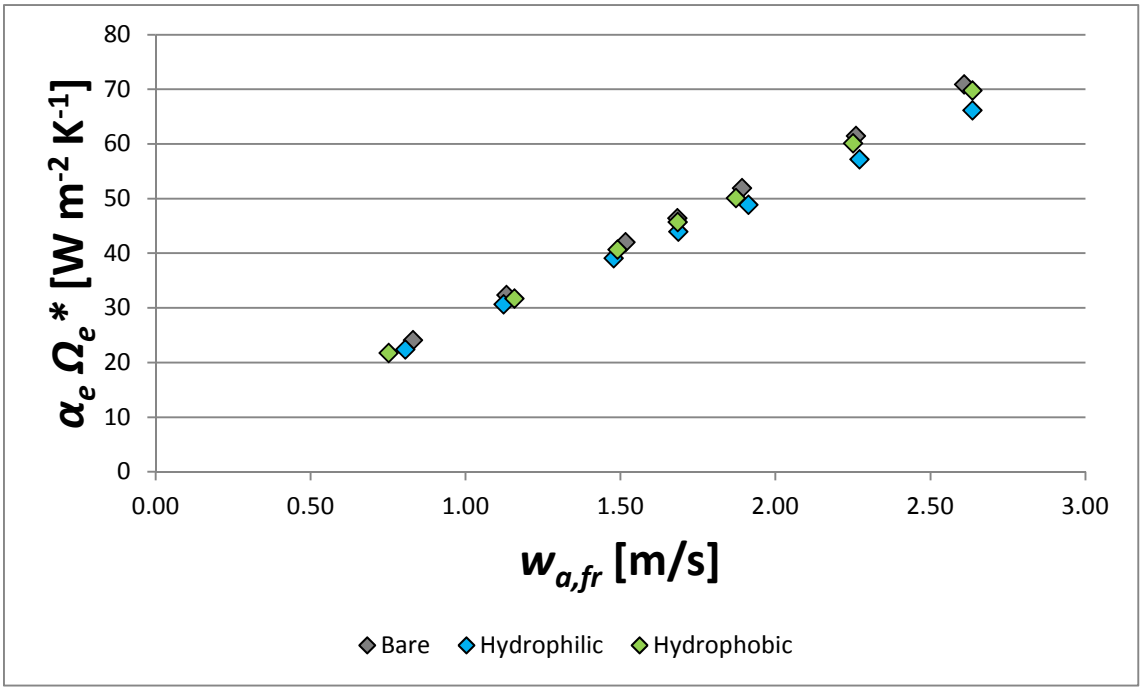

Fig. B.1 Air side heat transfer coefficient for wavy fin samples

As can be seen from Fig. B.1, the air side heat transfer coefficients of the hydrophobic and the untreated samples present similar values. This behaviour underlines that the hydrophobic treatment does not influence the sensible heat transfer process. On the other hand, the hydrophilic sample shows lower values of the air side heat transfer coefficient for the same air frontal velocities. This difference can be ascribed to the presence of an additional contact resistance to the heat transfer in the hydrophilic sample. This additional resistance may arise during the coupling phase between the untreated tube and the hydrophilic fins. In Eq. B.1, Eq. B 2 and Eq. B.3, the resultant correlations, respectively of the untreated, hydrophobic and hydrophilic samples, are shown.

$$\alpha_e \cdot \Omega_e^* = 28.60 \cdot w_{a,fr}^{0.937} \tag{B.1}$$

$$\alpha_e \cdot \Omega_e^* = 28.01 \cdot w_{a,fr}^{0.935} \tag{B.2}$$

$$\alpha_e \cdot \Omega_e^* = 27.31 \cdot w_{a,fr}^{0.906} \tag{B.3}$$

As can be seen from Eq. B.1, Eq. B.2, the coefficients *a* and *b* of the two equations are respectively quite closer between each other, confirming the similar behaviour between the untreated and the hydrophobic samples in the sensible heat transfer process. On the other side, the coefficient *a* and *b* in Eq. B.3 are have values much more different than the previous two samples. The corrugation angle of the three test samples was not available from the supplier. Due to this lack, a comparison between experimental results and heat transfer models in the open literature was not possible.